Democratic and Popular Republic of Algeria
Ministry of Higher Education and Scientific Research
Djillali Liabes University, Sidi-Bel-Abbes.
Faculty of Exact Sciences.
Department of Materials and Sustainable Development.

Ab-initio Study of the Physical Properties of Heusler Alloys

Thesis Submitted in Partial Fulfillment of the Requirements for the Degree of Doctorate in Theoretical Concepts and Modeling Techniques in Materials Sciences

Prepared by:
Miss. Amina MAÂFA

Supervisor:
Pr. Habib ROZALE

Board of Examiners:

Mme F. BOUKABRINE	**MC(A) (UDL SBA)**	**President**
Mr H. ROZALE	**Pr (UDL SBA)**	**Supervisor**
Mr. A. CHAHED	**Pr (UDL SBA)**	**Examiner**
Mme H. RIANE	**MC(A) (Univ. Mascara)**	**Examiner**

Academic Year 2020 - 2021

Acknowledgments

Alhamdulillah, thank you Allah for all the blessing You had given me. The ability, courage, endurance and patience You put inside me strengthening me in completing this study and research.

First and foremost, I would sincerely thank my supervisor Pr. Rozale Habib for his wisdom guidance, his patience, and mostly for being very understanding during the last couple years. His motivation and enthusiasm encouraged me to work harder and increase my research knowledge in order to complete this thesis.

Likewise, I would like to thank Pr. Chahed Abbes for his time, valuable feedback in the laboratory and his positive attitude. His guidance helped me in all the time of research and writing of this thesis.

My deep and respectful gratitude goes to Dr Boukabrine Fouziya and Pr Riane Houriya to have agreed to judge this work and to be reviewers.
I would like to thank Pr. Benhelal Omar and Dr. Bouabdallah Badera for being part of my Master's thesis.

Also I want to sincerely thank Pr. Foudil Khelil from university "Mustapha Stambuli" of Mascara, for his kindness, his support and for being a source of inspiration.

During this work, I have collaborated with many colleagues whom I have great regard and I wish to extend my warmest thanks to all the members of condensed matter and sustainable development laboratory, University of Djilali Liabes.

I owe my loving thanks to my supportive, encouraging and patient father and mother. My gratitude goes to my beloved grandmothers for being supportive and understanding during the whole course of my study. Special thanks to my sisters, my aunts, my friends and to each and every person that has supported me in accomplishing this thesis.

This work is dedicated to the soul of my grandfathers

Guendouz Nemiche, and Maafa Miloud

ملخص

منذ اكتشافها، أصبحت سبائك المغناطيس الحديدية النصف معدنية موضوعا للعديد من البحوث النظرية والتطبيقية. لقد جذبت مركبات هسلر المعروفة معظم الاهتمام حيث أن العديد منها يتميز بالخصائص النصف معدنية.

تضم عائلة هسلر الآلاف من المركبات التي تمتاز بخصائص مغناطيسية متنوعة مما يجعلها ذات أهمية كبيرة في مختلف الميادين المعاصرة مثل السبينترونيكس. لهذا السبب، كان جل اهتمامنا يتمحور حول مركبات هسلر الثلاثية الأكثر استكشافا بالإضافة الى مشتقاتها الرباعية.

قمنا في هذا العمل بدراسة الخصائص البنيوية، الالكترونية، المغناطيسية وخصائص المرونة، بالإضافة الى الخصائص الكهرو حرارية لسبائك هسلر الثلاثية والرباعية القائمة على معادن الحديد الكوبالت. الحسابات أجريت بالاعتماد على طريقة الموجة المستوية خطيا المدمجة في برنامج wien2k في إطار نظرية تابع الكثافة الدالية DFT وذلك باستخدام التقريب GGA.

بالنسبة لمركبات هسلر الثلاثية X_2MoGe (X = Co, Fe) و Co_2MoSb، فهي تمتاز ببنية مكعبة متما سكة و مستقرة، و هي البنية العكسية XA. أما بالنسبة لباقي المركبات، فهي تمتاز بالبنية المكعبة L_{21}. عند دراسة الخصائص الالكترونية، وجدنا أن المركبان Fe_2ZrSb و Co_2ZrGe هما من فئة النواقل النصف معدنية حيث قيم العزم المغناطيسي الكلي تساوي μ_B 0.99 و μ_B 1.96، بالتتابع. بالنسبة لمركب Fe_2ZrGe، فهو يمتاز بكونه شبه ناقل مع قيمة العزم المغناطيسي الكلي μ_B 0. أما باقي المركبات فهي من فئة النواقل في حالتي السبين الأعلى و السبين الأسفل.

قمنا كذلك بحساب معاملات المرونة الخاصة بالبنية المكعبة، فوجدنا أن ثوابت المرونة C_{11}، C_{12} و C_{44} الخاصة بالمركبات Fe_2ZrSb، Co_2ZrGe وFe_2MoZ (Z = Ge, Sb) تخضع لشروط الاستقرار. أما بالنسبة للمعاملات الخاصة بالمركبات Fe_2ZrGe، Co_2ZrSb و Co_2MoZ، فنلاحظ أن C_{11} أصغر من C_{12}، مما يرجح عدم استقرارها.

عند دراسة مركبات هسلر الرباعية، وجدنا أن المركبان CoFeZrGe و CoFeZrSb يتميزان بخصائصهما النصف معدنية مع قيم العزم المغناطيسي الكلي μ_B 1.05 و μ_B 1.99، بالتتابع. أما عن باقي المركبات، فهي من فئة النواقل في حالتي السبين الأعلى والأسفل.

أظهرت نتائج حساب معاملات المرونة أن كل المركبات الرباعية تخضع لشروط الاستقرار.

وأخيرا قمنا بدراسة الخصائص الكهرو حرارية، حيث أظهرت الحسابات مدى فاعلية هذه المركبات في مجال الاستخدام الكهرو حراري، مما يشجع على المزيد من الدراسات الفرضية والتطبيقية لهذه المركبات الحديثة.

الكلمات المفتاحية: سبائك هسلر، النواقل النصف معدنية، معاملات المرونة، الخصائص الكهرو حرارية، نظرية تابع الكثافة الدالية.

Abstract

Since their discovery, half-metallic ferromagnets have been the topic of many theoretical and experimental researches due to their potential applications. The well-known Heusler compounds have attracted most attention as several among them were predicted to be half-metals. The family of Heuslers incorporates thousands of members exhibiting diverse magnetic phenomena, which makes them very useful in various contemporary fields such as spintronics. For this reason, we have been interested in the ternary most explored group of Heusler alloys as well as their quaternary daughter systems.

At first, we have investigated a set of Co- and Fe-based ternary systems (X = Fe, Co; Y = Zr, Mo and Z = Ge, Sb) using ab-initio calculations. We found that Cu_2MnAl type structure is more favorable for all compounds, except X_2MoGe (X = Co, Fe) and Co_2MoSb where the inverse structure was energetically more stable. After studying the electronic properties, we have identified two half-metals (Co_2ZrGe and Fe_2ZrSb) that could be potential for spintronics applications. Unlike Fe_2ZrSb, the half-metallicity in Co_2ZrGe alloy has already been predicted in few theoretical studies where the structural and electronic properties agree well to our results.

We have also checked the mechanical properties of the ternary alloys. The elastic parameters indicated the mechanical stability of the four Fe_2ZrSb, Co_2ZrGe and Fe_2MoZ (Z = Ge, Sb) materials, where the half-metallic Fe2ZrSb compound is the only one characterized by an enhanced ductility.

Afterwards, we completed the previous study by forming eight quaternary structures using the same previous magnetic components. We have studied the physical properties of the quaternary XX'YZ alloys (X = Co, Fe; X' = Mo, Fe; Y = Zr, Fe; Z = Sb, Ge) and explained their relation with the former ternary Heuslers. The DFT method was once again applied to investigate the magnetic nature of these alloys and we found two other half-metals (CoFeZrGe and CoFeZrSb). Actually, both materials have already been investigated and the resulting lattice constants and gaps were close in values to our theoretical calculations.

Additionally, we have computed the elastic parameters, electronic properties as well as the thermoelectric efficiency of the quaternary XX'YZ alloys. They were found to be mechanically stable and have shown different degrees of ductility and stiffness. Besides, they could be very

efficient for the thermoelectric field applications, which paves the way for further theoretical and experimental investigations concerning these new Heuslers.

Keywords: Heusler alloys, half-metals, elastic constants, thermoelectric properties, density functional theory.

Résumé

Dès leur découverte, les matériaux semi-métalliques sont devenus très attractifs et ils présentent un sujet de base dans des milliers de recherches théoriques et expérimentales. Une raison particulière est leur usage dans divers domaines modernes notamment, ceux concernant le domaine du spintronique. Pour cette raison, nous étions intéressés à l'étude des alliages ternaires ainsi que leurs filles quaternaires.

En premier lieu, on a investiguer le groupe Co_2- et Fe_2YZ d'alliages ternaires (X = Fe, Co; Y = Zr, Mo and Z = Ge, Sb) en utilisant la méthode ab-initio. La structure Cu_2MnAl a été adoptée par tous les alliages sauf X_2MoGe et Co_2MoSb, où la structure Hg_2CuTi été plus stable énergétiquement. Après étudier les propriétés électroniques, on a trouvé deux composés semi-métalliques (Co_2ZrGe et Fe_2ZrSb) qui pourraient être utiles dans le domaine du spintronique. Les résultats du matériau Co_2ZrGe ont été déjà prédits dans quelques études théoriques, et le type de structure et la valeur du gap sont en bon accord avec nos résultats.

Ainsi, on a calculé les propriétés élastiques de ces composés ternaires. On a trouvé que les matériaux Fe_2ZrSb, Co_2ZrGe et Fe_2MoZ (Z = Ge, Sb) satisfont les conditions de stabilité, où le semi-métallique Fe_2ZrSb est le seul matériau caractérisé par une ductilité accrue.

Ensuite, on a étudié une deuxième famille de Heusler appelée les alliages quaternaires XX'YZ (X = Co, Fe; X' = Mo, Fe; Y = Zr, Fe; Z = Sb, Ge) et on a essayé de trouver la relation entre leurs propriétés physiques et celles de leurs parents ternaires. La méthode DFT a été de nouveau appliquée afin de savoir la nature magnétique de ces composés et on a trouvé deux autres semi-métaux (CoFeZrGe et CoFeZrSb). Ces derniers ont été déjà investiguer et leurs paramètres de mailles et gaps sont très proche de ceux estimés dans notre travail.

En outre, nous avons calculé les paramètres élastiques, propriétés électroniques et efficacité thermoélectrique des alliages quaternaires. Ils se sont révélés mécaniquement stables et ils présentent différents degrés de ductilité. Ainsi, ils pourraient être très efficaces pour les applications de champ thermoélectrique, ce qui ouvre la voie à d'autres recherches théoriques et expérimentales concernant ces nouveaux matériaux Heusler.

Les mots clés: alliages Heusler, les matériaux semi-métalliques, les constantes élastiques, les propriétés thermoélectriques, la théorie de la fonctionnelle de la densité.

Table of Contents

Chapter III. Methodology

Chapter IV. Results and Discussion

List of Figures

List of Tables

List of Publications

Large portions of Chapters IV have appeared in its entirety as:

1. "Theoretical study of the electronic properties of X_2YZ (X = Fe, Co; Y = Zr, Mo; Z = Ge, Sb) ternary Heusler: ab-initio study"
   A Maafa, H Rozale, A Oughilas, A Boubaça, A Amar, D Lucache
   Annals of the West University of Timisoara. Physics Series 62, 1-14

2. "Electronic properties, stability and thermoelectric response of CoFeZrZ (Z= Ge, Sb) quaternary Heuslers"
   A Maafa, LF Blaha, H Rozale, A Ougilas, MAH Boukli, A Sayade
   Materials Chemistry and Physics 263, 124405

The following papers are not related to this thesis in any manner:

1. "Probing the structural, elastic, electronic and thermoelectric properties of C15-type Laves phase LaCo2: a DFT based ab-initio investigation"
   S Ziri, L Blaha, F Boukabrine, A Maafa, A Oughilas, A Bouabca, H Rozale
   Revista Mexicana de Física 67 (4)

2. "The first principle calculations of structural, magneto-electronic, elastic, mechanical, and thermoelectric properties of half-metallic double perovskite oxide Sr2TiCoO6"
   LF Blaha, A Maafa, A Chahed, MAH Boukli, A Sayade
   Revista Mexicana de Física 67 (1 Jan-Feb), 114-122

3. "Electronic and Thermoelectric Properties of Li-Based Half-Heusler Alloys: A DFT Study"
   F Issaad, A Maafa, H Rozale, MAB Hacene, A Bouabça
   Annals of the West University of Timisoara. Physics Series 62, 95-107

Introduction

Since their invention, integrated circuits (IC) [1] have become the heart and brain of most circuits and they exist almost in every circuit board. The number of electronic components that can be placed on an IC is characterized by Moore's law [2], which describes a long-term trend in the history of computing hardware.

In the last decades, advances in magnetic hard drive technology have increased the capacity of typical hard drives. However, there is a limit to such packing due to the finite interatomic distance of a few Angstroms in typical materials. Another important issue is the volatility of the information stored. Intense research efforts were dedicated to the area of magnetic data storage to produce smaller and faster devices.

In 1988 [3,4], Fert and Grünberg [5] discovered a totally new physical effect called the giant Magneto-resistance (GMR). GMR was the perfect tool for reading data from hard disks when information registered magnetically has to be converted to electric current.

Innovative technologies have been developed since the discovery of GMR to utilize the electron spin degree of freedom for information manipulation, storage, and transmission. Metal-based devices in the form of hetero-structures have already found applications in ultra-high density magnetic recording [6], as GMR sensors [7], in prototype magnetic random access memory (MRAM) [8] and in spin-current switches [9]. These devices utilize ordinary ferromagnetic (FM) materials that have a finite electronic spin polarization at Fermi energy. Information can be encoded into the finite resistance change resulting from spin-dependent electric transport through these magnetic hetero-structures. Unlike the conventional nonmagnetic devices, these devices exploit the spin degree of freedom. They have the advantages of increasing integration densities, non-volatility, accelerating speed in data processing and lowering the power consumption.

Further development of these new technologies is by combining semiconductors and magnetism (utilize both electron's charge and spin degree of freedom), in other words, employing spintronics [10].

Spintronics is characterized by the transport of spin or charge and spin in semiconductor-based materials. These materials can be composed of FM metals, magnetic semiconductors with or without doping, and/or the so-called “half-metals” (HMs) [11,12].

Half-metals are a special kind of materials having novel spin properties due to their unique electronic structures. Many compounds were predicted to be half-metals [13-17] and Heusler alloys [18] received the most experimental and theoretical interest.

The main goal of this work is to study Heusler compounds with the objective of developing new potential half-metallic materials. First principles calculations based on the density functional theory [19] have helped us significantly in understanding the electronic and magnetic behavior of these compounds.

Bibliography

1. Kilby, Jack S. ”Miniaturized Electronic Circuits”, U.S. patent 3,138,743, filed 6 February 1959, issued 23 June 1964.
2. Tuomi, I. (2002). “The Lives and Death of Moore’s Law”. First Monday. 7 (11).
3. M. N. Baibich, J. M. Broto, A. Fert, F. N. Van Dau, F. Petro, P. Etienne, G. Creuzet, A. Friederich and J. Chazelas, Phys. Rev. Lett. 61, 2472 (1988).
4. G. Binasch, P. Grünberg, F. Saurenbach and W. Zinn, Phys. Rev. B 39, 4828 (1989).
5. "The Nobel Prize in Physics 2007". Nobel Foundation. Archived from the original on 5 August 2011. Retrieved 27 February 2011.
6. Ross C A 2001 Magnetic behavior of lithographically patterned particle arrays, Presented at 46th MMM (Seattle, WA) Paper AC-06.
7. M. N. Baibich, J. M. Broto, A. Fert, F. Nguyen Van Dau, f. Petroff, P. Etienne, G. Creuzet, A. Friederich, and J. Chazelas Phys. Rev. Lett. 61, 2472 (1988).
8. Inomata, K., Ikeda, N., Tezuka, N., Goto, R., Sugimoto, S., Wojcik, M., Jedryka, E.: Highly spin-polarized materials and devices for spintronics. Sci. Technol. Adv. Mat. 9(1), 014101 (2008).
9. F. J. Albert, J. A. Katine, and R. A. Buhrman. Appl. Phys. Lett. 77, 3809 (2000).
10. C. Felser, G.H. Fecher and B. Balke, Angew. Chem. Int. Ed. 46 (2007) p.668.
11. R.A. de Groot, F.M. Mueller, P.G. van Engen and K.H.J. Buschow, Phys. Rev. Lett. 50 (1983) p.2024.
12. J. Kübler, A.R. William and C.B. Sommers, Phys. Rev. B 28 (1983) p.1745.
13. Solovyev, I.V.; Kashin, I.V.; Mazurenko, V.V. Mechanisms and origins of half-metallic ferromagnetism in CrO2. Phys. Rev. 2015, 92, 144407.
14. Bhat, S.G.; Anil Kumar, P.S. Demonstration of efficient spin injection and detection in various systems using Fe3O4 based spin injectors. AIP Adv. 2016, 6, 056308.
15. Park, J.H.; Vescovo, E.; Kim, H.J.; Kwon, C.; Ramesh, R.; Venkatesan, T. Direct evidence for a half-metallic ferromagnet. Nature 1998, 392, 794–796.
16. Velasco, P.; Alonso, J.A.; Casais, M.T.; Martínez-Lope, M.J.; Martínez, J.L. Analysis of magnetotransport data of Tl2Mn2O7 pyrochlore: evidence for half-metallicity. J. Phys. Condens. Matter 2004, 16, 8725.
17. Sarma, D.D.; Mahadevan, P.; Saha-Dasgupta, T.; Ray, S.; Kumar, A. Electronic Structure of Sr2FeMoO6. Phys. Rev. Lett. 2000, 85, 2549–2552.

18. Heusler, F. Über magnetische manganlegierungen. Verh. Dtsch. Phys. Ges. 1903, 5, 219.
19. W. Koch, M. C. Holthausen, *A Chemist's Guide to Density Functional Theory*, Wiley-VCH, Weinheim, Germany, (2000).

Chapter I

Theoretical Background

Ferromagnetic materials with unsaturated d shells (iron Fe, cobalt Co, and nickel Ni, …) have always been of great interest in several innovative advanced technologies. Heusler compounds are a class of ferromagnetic materials that have made a significant topic of research. Due to their unique electronic structure, Heuler alloys exhibit a wide variety of properties such as spintronics [1], thermoelectrics [2,3] and magnetic shape memory effects [4,5].

In 1988, the Frenchman **Albert Fert** and the German **Peter Grünberg** [6] each independently discovered the antiferromagnetic coupling effect in Fe/Cr/Fe multilayered system [7]. Fert and Grünberg were later rewarded the Nobel Prize in 2007 for this experimental discovery in physics [8].

The giant magneto-resistance (GMR) is a quantum mechanical effect observed in multilayers composed of alternating ferromagnetic and non-magnetic conductive layers (see figure (I.1)) [9,10].

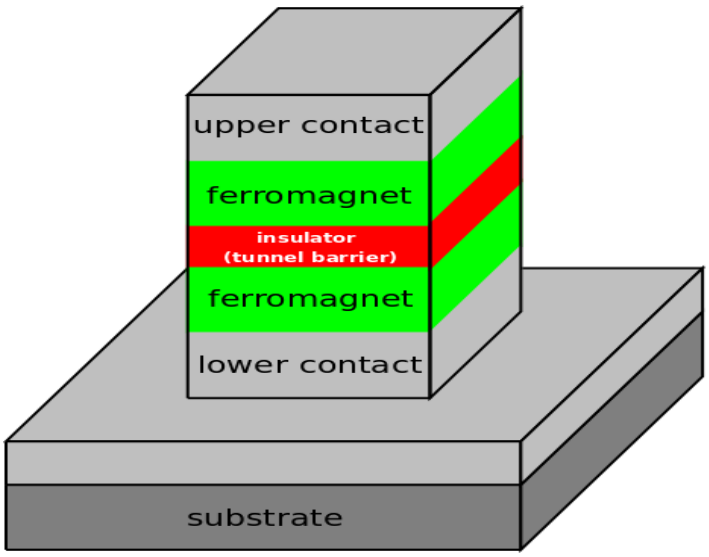

Figure I.1 Magnetic tunnel junction.

It manifests in a significant change in the electrical resistance depending on whether the magnetization of adjacent ferromagnetic layers are in a parallel or an antiparallel alignment, where under the influence of an external magnetic field, the overall resistance is relatively low for parallel alignment and relatively high for antiparallel alignment (see figure (I.2)).

Very weak magnetic changes give rise to major differences in electrical resistance in a GMR system. A system of this kind is the perfect tool for reading data from hard disks when information registered magnetically has to be converted to electric current. Soon researchers and engineers began work to enable use of the effect in read-out heads. In 1997, the first commercial read heads based on GMR were designed and launched by IBM (International Business Machines) and this soon became the standard technology. Even the most recent read-out techniques of today are further developments of GMR.

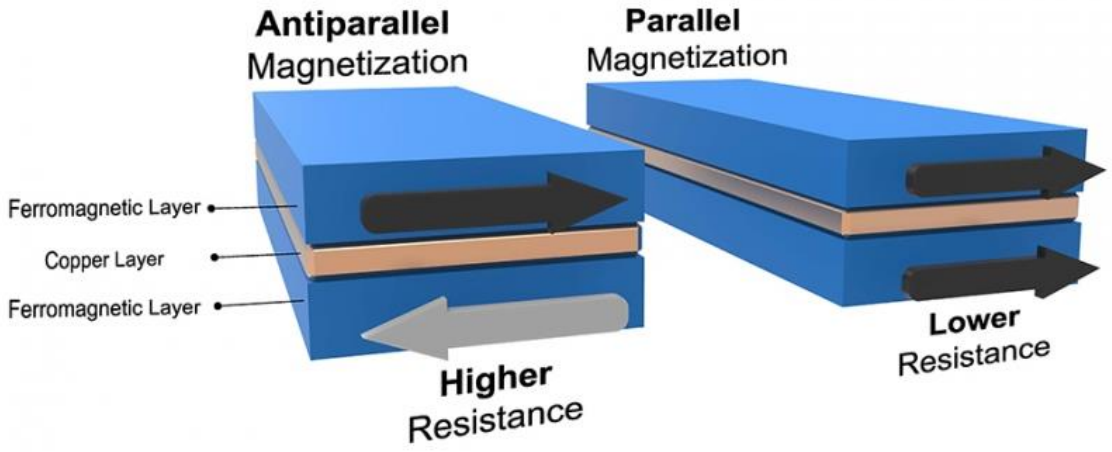

Figure I.2 Dependence of the electrical resistance on the relative magnetic alignment of the ferromagnetic layers.

The main applications of GMR are magnetic field sensors (which are used to read data in hard disk drives HDD) [11], biosensors [12], micro-electromechanical systems (MEMS) and other devices [13]. GMR multilayer structures are also used in magneto-resistive random-access memory (MRAM) [14] as cells that store one bit of information. Besides, GMR is found in nearly all computers, and it was used in some digital cameras and MP3 players.

Actually, it was the discovery of GMR that paved the way for new physics, such as TMR (tunneling magneto-resistance) [15]. TMR technology is the natural evolution of older

technologies like GMR and AMR (anisotropic magneto-resistance) [16] (see figure (I.3)). It is a magneto-resistive effect that occurs in a magnetic tunnel junction (MTJ), which is a component consisting of two ferromagnets separated by a thin insulator. If the insulating layer is thin enough (typically a few nanometers), electrons can tunnel from one ferromagnet into the other. Since this process is forbidden in classical physics, the tunnel magneto-resistance is a strictly quantum mechanical phenomenon.

The highest tunnel magneto-resistance ratio record were obtained when the Co_2MnSi Heusler compound was used in tunnel-junction devices [17]. GMR and TMR devices have then a basic common structure, namely two ferromagnetic metal films separated by a nonmagnetic film. The difference between the structures of these devices is in the nonmagnetic spacer film, which consists of a metal film (GMR) or an insulator film (TMR) (see figure (I.3)). The discovery of giant magneto-resistance has opened the eyes on using the electron spin degree of freedom to develop innovative technologies, where traditionally, the electronic devices used to rely only on charge degree of freedom. Nowadays, advanced devices exploit electron spin properties in addition to their charge, thus defining the term spintronics [18].

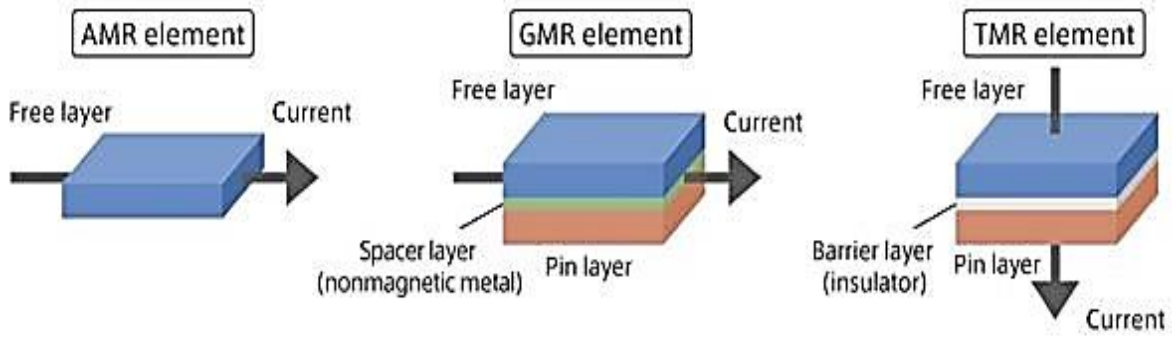

Figure I.3 Evolution of anisotropic magneto-resistance.

As mentioned above, studies of spintronics started in 1988 after the discovery of GMR, which was implemented in hard disk drives (HDD). Because today's information technology needs larger capacity data storage and faster data processing, spintronics, based on spin polarized electron transport, satisfy the above requirements. Actually, Heusler alloys offer fascinating functionalities in this particular domain. The main feature that makes these materials efficient for spintronics applications is their ideal 100% spin polarization.

I.1 Spin polarization

In a nonmagnetic material, the occupation of spin up and spin down states is equal, resulting in a zero net spin polarization. However, in a ferromagnetic metal, states of one spin channel are more occupied than the other, which leads to nonzero net spin polarization and ferromagnetic properties. Spin polarization is then quantified by the difference between the numbers of spin up and spin down electrons at Fermi level, as follows:

$$P = \frac{N_{\uparrow}(E_f) - N_{\downarrow}(E_f)}{N_{\uparrow}(E_f) + N_{\downarrow}(E_f)} \times 100\% \quad \text{(I-1)}$$

where $N_{\uparrow}$ and $N_{\downarrow}$ represent the density of state of spin up and spin down near the Fermi level (E_f), respectively.

The formula that relates the spin polarization (P) and the magneto-resistance for TMR devices was expressed in terms of spin polarization of two ferromagnetic electrodes (P_1, P_2) [19], as follows

$$TMR = \frac{2P_1P_2}{1 - P_1P_2} \quad \text{(I-2)}$$

As P approaches 1, TMR values approach infinity, which implies that a perfect switch can be made with a 100% spin-polarized material.

Highly spin-polarized ferromagnetic materials are strongly desired for spintronics devices such as magnetic tunnel junctions (MTJs), spin injectors to semiconductors and spin-torque oscillators [20-22]. Unfortunately, the spin polarization of common ferromagnets such as Fe and Co is only about 35-40% [23]. Hence, conventional ferromagnets cannot inject electrons with a large degree of spin polarization into the non-magnetic material [24]. The injected spin polarization could be increased by employing a half-metallic ferromagnet (HMF) [25] or a dilute magnetic semiconductor (DMS) [26], both of which might have 100% spin polarization in theory.

However, in a DMS, Curie temperatures (the temperature above which certain materials lose their permanent magnetic properties) are typically below 80 K. For this reason, HMFs present a convenient solution for exploiting 100% spin polarization induced by spontaneous magnetization [27]. Among the many theoretically proposed HMFs, Heusler compounds hold the greatest potential to realize half-metallicity at room temperature due to their high Curie temperatures [28], lattice constant matching with major substrates (such as III–V semiconductors and MgO), and generally large gap at Fermi level (E_F) [29]. A minority of

Heusler compounds were calculated to be half-metals and particularly promising as ferromagnetic electrodes of magneto-resistive devices since they have high Curie temperatures and high spin polarization. Finding such highly spin-polarized materials (half-metals) presents a main challenge for many theoreticians and experimentalists. So what are half-metals?

I.2 Heusler compounds as Half-metallic Ferromagnets

The concept of half-metallic ferromagnetism has attracted great interest since its introduction in the early 1980s. Half-metals (HMs) are materials that, unlike ordinary metals (Fe) combining both spin types at Fermi level, have only spin up electrons at E_f ($N_\downarrow(E_f) = 0$), leading to 100% spin polarization. HMs have then the peculiarity of being magnetic and semiconducting at the same time. This concept was initially predicted by de Groot and collaborators using first-principles electronic calculations. They observed unusual electronic properties of the half-Heusler NiMnSb [30] and showed that this compound is in reality half-metallic, i.e. the minority band is semiconducting with a gap at the Fermi level.

NiMnSb has attracted considerable attention among theoreticians and several first-principles calculations have confirmed its half-metallic character [31-36]. This half-metallic compound has also attracted a lot of experimental interest [37-39]. It belongs to the family of Heuslers [40] consisting of full Heuslers and Half-Heusler compounds.

The first family of Heusler alloys is of the form X_2YZ, crystallizing in the L21 structure, which consists of four fcc sublattices. Such Heusler compounds have attracted a lot of interest due to the possibility to study in the same family of alloys a series of interesting diverse magnetic phenomena. In fact, full Heusler alloys were the first to be synthetized [41].
The Japanese research groups were the first to predict the existence of half-metallicity in the case of full Heusler compounds. Using *ab-initio* electronic structure calculations, Ishida and collaborators studied the Co2MnZ alloys, where Z stands for Si and Ge [42-44], and Fujii and collaborators studied the Fe2MnZ alloys [45].

Full-Heusler compounds became very popular for potential applications and several groups managed to grow Co2MnGe and Co2MnSi thin films [46-53]. Experimentally, many full Heusler alloys have been confirmed to be half-metallic [54,55].

Heusler alloys of the second class are of the form XYZ, crystallizing in the C1b structure, and consisting of three fcc sublattices; they are often called half- or semi-Heusler alloys in literature.

As half-metallic ferromagnets have a great potential in the emerging field of spintronic applications [56,57], magneto-optical effects [58] and GMR applications [59], Heusler alloys have been rigorously investigated and many of them were predicted to be new HMFs [60-67].

I.3 Classes of Half-metals

Up to now, three main classes of ferromagnetic half-metals have been found by theory and/or experiment with distinct crystal structures. The first class of ferromagnetic half-metals are Heusler alloys [68], such as Co_2CrAl. The second one are the oxides, such as CrO_2 [69], and the third one are those having the zinc blende (ZB) structure (e.g., CrAs) [70,71].

A common feature of all these HMs is that they contain at least one transition-metal (TM) atom, such as Co, Mn, or Fe in the unit cell, where their d-states play a key role in the half-metallicity.

The interaction of the d-states with the states of other atoms (the d-states of other TM atoms, the p-states of oxygen atoms, pnictides, or Group IV elements) give rise to a number of distinguishing properties.

I.4 Half-metallic ferrimagnets

Half-metallic ferrimagnetic materials are desirable candidates for the applications in magneto-electronic devices. The advantage of a ferrimagnetic interaction is the resulting reduction of the magnetic moment due to the compensation of the moments carried by the different sublattices. These materials offer distinct advantages over their ferromagnetic counterparts, which are mostly due to their small magnetic moment. The ideal compensated ferrimagnet would exhibit a total magnetic moment of zero. In fact, half-metallic fully-compensated ferrimagnets (HM-FCF) [72] were initially named half-metallic antiferromagnets (HMAs).

In 1995, van Leuken and de Groot proposed a new class of materials called half-metallic antiferromagnets [73]. In conventional antiferromagnets, the symmetry of sites with opposite spin results in no spin polarization. However, in the case of crystallographically inequivalent magnetic sublattices with antiparallel alignment of their spins, half-metallicity combined with a zero net magnetic moment can be achieved, giving rise to half-metallic compensated ferrimagnets (see figure (I.4)). In this respect, Heusler compounds are an interesting class of materials. One of their major advantages is the high tunability of their magnetic structure because of the existence of one or more magnetic sublattices. The HMA character has been

reported the first time when studying the semi-Heusler compound CrMnSb, and it has been confirmed by calculations made by Shaughnessy and collaborators [74].

Except the semi-Heusler CrMnSb, full Heusler alloys with 24 valence electrons have also been predicted to be HMAs including the Mn3Ga [75,76], Cr2MnZ (Z = P, As, Sb, Bi) alloys [77,79], the Co-doped Mn2VZ (Z = Al, Si) half-metallic ferrimagnetic alloys and the Cr-doped Co2CrAl [80].

Heusler compounds are not the only family where the half-metallic anitferromagnetism has been predicted. Potential HMA candidates include also the double-perovskites [81-85], superlattice structures [86,87], diluted magnetic semiconductors [88,89] and even Fe-based superconductors [90].

Finally, it is possible to grow a HMA by combing alternate layers of half-metallic ferromagnetic and ferrimagnetic Heusler compounds as suggested in [91].

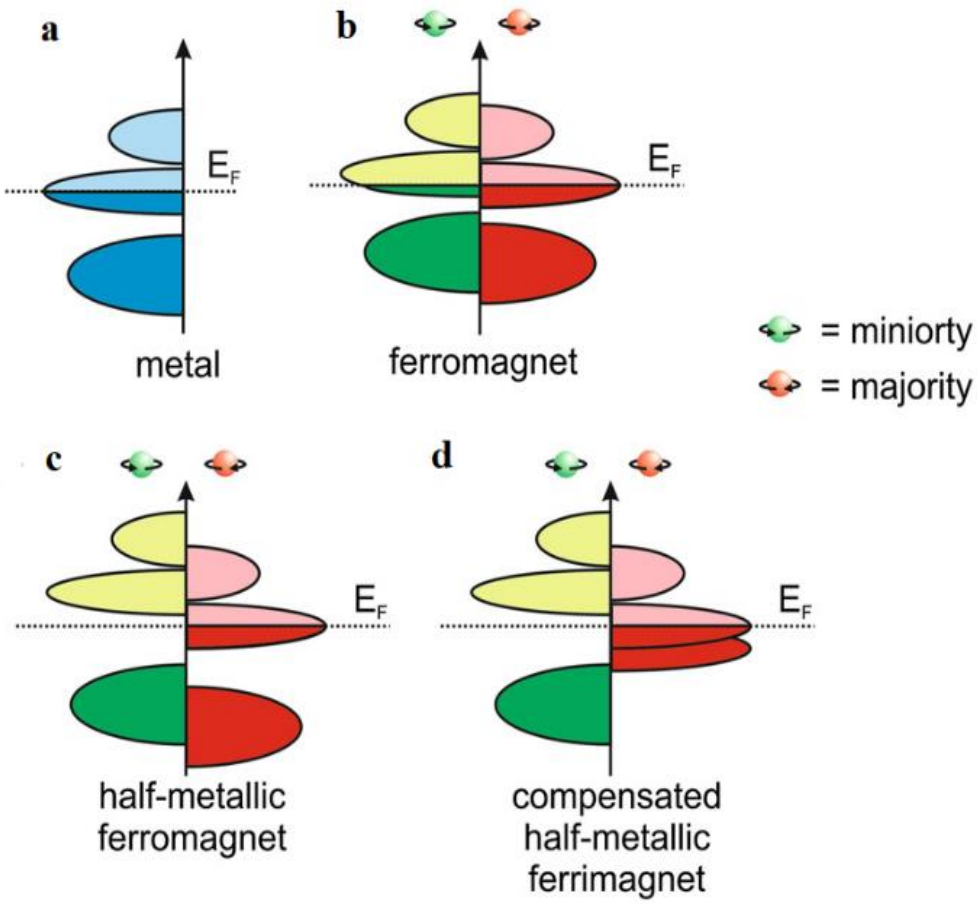

Figure I.4 Density of states of (a) a metal, (b) a ferromagnet, (c) a half-metallic ferromagnet, and (d) a completely compensated half-metallic ferrimagnet [92].

I.5 Magnetic semiconductors

Another type of materials are the ones combining both the semiconducting behavior with the magnetic properties. Such compounds can offer novel functionalities to spintronic and magneto-electronic devices, e.g. they can act as spin-filter materials. These materials can find application in magnetic tunnel junctions (MTJ). In usual MTJs, the magnetic electrodes are separated by an insulating barrier and ballistic transport is achieved through the tunneling of the electrons via the barrier. The alternative is to use a spin-filter material as the barrier and have metallic electrodes. Then the probability for electrons tunneling through the spin-filter barrier is different for the two spin-directions and the flow of a spin-polarized current can be achieved [93,94]. Among Heusler compounds, there are two families of compounds studied recently that are magnetic semiconductors and can be used as spin-filter materials:

(i) (CoV)XAl with X being Ti, Zr or Hf, which are ferromagnetic semiconductors [95], and (ii) (CrV)XAl with X being Ti, Zr or Hf, which are fully-compensated ferrimagnetic semiconductors [96]. The latter also combines magnetic semiconducting behavior with zero magnetization leading to minimum energy losses in devices.

A special class are the so-called spin-gapless semiconductors [97]. These materials combine the properties of half-metals and magnetic semiconductors, and they are actually magnetic semiconductors, where there is an almost vanishing zero-width energy gap at Fermi level in the majority spin direction and a usual energy gap in the other spin-direction. Spin-gapless semiconductors offer also novel functionalists due to their unique properties: (i) the mobility of carriers is considerably larger than in usual semiconductors, (ii) excited carriers include both electrons and holes, which can be 100% spin-polarized simultaneously, and (iii) a vanishing amount of energy is enough to excite majority spin electrons from the valence to the conduction band.

Although gapless-semiconductors are well known in literature, it was not until 2008 that Wang proposed that the doping of $PbPdO_2$, a gapless semiconductor with transition metal atoms, would lead to a spin-gapless semiconductor [98,99]. Experimental confirmation was offered in 2014 by Kim and collaborators who studied polycrystalline films of Mn and Co doped $PbPdO_2$ [100]. Among Heusler compounds, several have been identified to be spin-gapless semiconductors [101-103]. The main attention was given to Mn_2CoAl, an inverse full Heusler compound, due to its successful growth in the form of films [104]. Galanakis and collaborators

have shown that defects keep the half-metallic character of Mn2CoAl but destroy the spin-gapless semiconducting character [105].

Apart from the half-metallic character, Heusler alloys possess interesting diverse properties such as high magnetic Curie temperature [106], magneto-optical effects and spin filters [107], which explains the reason why these materials are extensively researched, studied and fabricated. However, there are certain factors that might affect the half-metallic character such as atomic disorder, defects and even vacancies [108,109]. More details about these phenomena are described in the next chapter.

I.6 Motivation for the study of Co- and Fe-based type of Heuslers

We found great passion in studying, particularly, Fe and Co-based Heusler families, and here are the reasons that motivated us:

Heusler alloys containing Co atoms have attracted much attention as they are strongly ferromagnetic and most of the predicted half-metals belong to Co_2YZ family [110-118].

Co-based compounds were synthesized and investigated in the 1970s. They show high spin polarization in tunnel junction devices and spin-resolved photoemission. Moreover, high tunnel magneto-resistance (TMR) has been observed in some magnetic tunnel junctions (MTJs) based on Co_2FeSi [119] and $Co_2Cr_{0.6}Fe_{0.4}Al$ [120] films.

Generally, many Co-based Heuslers have been predicted to be fully spin-polarized, making them suitable in spintronic domain. They have also drawn commendable interest for applications in the areas of spintronics and other magnetism related applications due to their high Curie temperatures [121,122]. For instance, Wurmehl et al. have reported an exceptionally high magnetic moment of 6 μB and a Curie temperature T_C of 1100K for the half-metallic Co_2FeSi [123]. Other remarkable properties would be visualized in their structural similarity to industrial binary semiconductors [125,125] as well as the variable localized Co magnetic moments [126]. Furthermore, the simple fabrication method of Co_2YZ materials makes them very attractive from the perspective of industrial applications. Yet there are relatively fewer investigations until now concerning Co-based systems with 4d transition metal elements. Several classes of Co-based compounds show a consistent trend with Slater-Pauling behavior. In contrast to experiments, calculations give a non-integer value of the magnetic moment in certain Co-based Heusler compounds.

Fe-based Heusler compounds, on the other hand, have also received as much interest as Co based ones. They are promising candidates for thermoelectric power generation. The theoretical investigation was demonstrated in Fe-based Heusler compounds using the first-principle calculations yielding the power factors, which are 4 to 5 times larger than that in the classical thermoelectric materials at room temperature [127]. Fe-based Heusler compounds are known to be soft ferromagnets with Curie temperature as high as 900 K, making them suitable for potential magnetic applications [128]. They have also been investigated experimentally and theoretically [129]. Unlike Co-based compounds, many Fe-based Heuslers often exhibit a deviation from the Slater Pauling rule due to disorder or less localized states at Fermi energy.

It has been found that Co and Fe atoms possess high spin magnetic moments in the periodic table. For this reason, the magnetization values of the ferromagnetic Co- and Fe-based Heusler compounds are high.

I.7 Thesis statement

This work offers a set of several novel ferromagnets, semiconductors and new distinctive half-metals with 3d and 4d transition elements, which can be exploited in various future electronic applications. These materials represent our primal motivator in making this thesis. Most of our work focuses on theoretical predictions of half-metallicity in ternary and quaternary iron (Fe) and cobalt (Co) based systems, as well as the effect of substituting Fe by Co atoms on the properties of the studied systems. Moreover, we have investigated different properties of these Heusler compounds in order to identify their capabilities and functionalities in different physical fields. We hope by the end of this experience to be able to clarify the impact of atomic arrangements on the electronic properties. Besides, we would like to find out how the conversion of a ternary Heusler structure to a quaternary one might influence the half-metallic character and the physical properties of these systems. Another interesting point in this thesis concerns the effect of the presence of both 3d and 4d magnetic constituents on the electronic and magnetic properties, as well as the half-metallic character.

I.8 thesis Outline

Chapter I describes the story behind the discovery of half-metallic ferromagnets and their fascinating properties and applications. We also discuss the types of materials predicted to be half-metals in addition to Heusler compounds. Moreover, we discuss the appearance of new

half-metallic alloys with magnetic properties, such as half-metallic ferrimagnets, magnetic semiconductors and spin-gapless semiconductors. Lastly, we mention the reasons that motivated us to study Co- and Fe-based type of Heuslers.

In chapter II, we remind of the nascence of the first Heusler alloy. Then, we introduce basic concepts relevant to Heusler compounds such as crystal structure, half-metallicity (HM) and other different magnetic phenomena. Next, we discuss special topics such as chemical disorder, defects and vacancies. In the last part of this chapter, details about the mechanical stability of cubic structures and the thermoelectric parameters are analyzed. We also present the main fields of applications of Heusler materials.

The essential of the density functional theory based on the works of Hohenberg, Kohn and Sham in addition to the exchange-correlation effect are discussed in chapter III. We also review the main classes of usual approximations for the exchange-correlation energy.
In chapter IV, we present the theoretical results concerning the ternary Co- and Fe-based series in addition to their quaternary derived compounds. For each system, we identify the crystal structure, electronic properties and magnetic behavior as well as the mechanical stability. The thermoelectric features are discussed for the quaternary systems only as most of the ternary alloys show no mechanical stability.

Lastly, we present the summary of all previous chapters and our futuristic vision.

I.9 Bibliography

1. S. A. Wolf, D. D. Awschalom, R. A. Buhrman, J. M. Daughton, S. von Molnár, M. L. Roukes, A. Y. Chtchelkanova and D. M. Treger, "Spintronics: A spin-based electronics vision for the future", Science 294, 1488-1495 (2001).
2. S. Populoh, M.H. Aguirre, O.C. Brunko, K. Galazka, Y. Lu, A. Weidenkaff, High figure of merit in (Ti, Zr, Hf) NiSn half-Heusler alloys, Scr. Mater. 66 (2012) 1073–1076.
3. C. Yu, T.-J. Zhu, R.-Z. Shi, Y. Zhang, X.-B. Zhao, J. He, High-performance half-Heusler thermoelectric materials Hf 1- x ZrxNiSn 1- ySby prepared by levitation melting and spark plasma sintering, Acta Mater. 57 (2009) 2757–2764.
4. R. C. O'Handley, S. J. Murray, M. Marioni, H. Nembach, S. M. Allen, Phenomenology of giant magnetic-field-induced strain in ferromagnetic shape-memory materials. J. Appl. Phys. 87, 4712–4717 (2000).
5. R. Kainuma et al., Magnetic-field-induced shape recovery by reverse phase transformation. Nature 439, 957–960 (2006).
6. Binasch, G.; Grünberg; Saurenbach; Zinn (1989). "Enhanced magnetoresistance in layered magnetic structures with antiferromagnetic interlayer exchange". Physical Review B. 39 (7): 4828–4830.
7. M. N. Baibich, J. M. Broto, A. Fert, F. N. Van Dau, F. Petroff, P. Etienne, G. Creuzet, A. Friederich and J. Chazelas, "Giant magnetoresistance of (001)Fe/(001)Cr magnetic superlattices", Physical Review Letters 61, 2472-2475 (1988).
8. "The Nobel Prize in Physics 2007". Nobel Foundation. Archived from the original on 5 August 2011. Retrieved 27 February 2011.
9. M. T. Sarah, "The discovery, development and future of GMR: The Nobel Prize 2007", Journal of Physics D: Applied Physics 41, 093001 (2008).
10. C. Hordequin, J.P. Nozières, J. Pierre, J. Magn. Magn. Mater. 183, 225 (1998).
11. *Khvalkovskii, A. V. "Гигантское магнитосопротивление: от открытия до Нобелевской премии". AMT&C. Archived from the original on 8 January 2015*. Retrieved 27 February 2011.
12. *Coehoorn, R. (2003). "Novel Magnetoelectronic Materials and Devices" (PDF). Giant magnetoresistance and magnetic interactions in exchange-biased spin-valves. Lecture Notes. Technische Universiteit Eindhoven. Archived from the original (PDF) on 24 July 2011*. Retrieved 25 April 2011.
13. Reig, Cardoso & Mukhopadhyay 2013.

14. Inomata, K., Ikeda, N., Tezuka, N., Goto, R., Sugimoto, S., Wojcik, M., Jedryka, E.: Highly spin-polarized materials and devices for spintronics. Sci. Technol. Adv. Mat. 9(1), 014101 (2008).
15. T. Miyazaki and N. Tezuka, Journal of Magnetism and Magnetic Materials 139, L231 (1995).
16. F. J. Yang et al. Applied Physics Letters 102, 172403 (2013).
17. H. Liu, Y. Honda, T. Taira, K. Matsuda, M. Arita, T. Uemura and M. Yamamoto, "Giant tunneling magneto-resistance in epitaxial Co2MnSi/MgO/Co2MnSi magnetic tunnel junctions by half-metallicity of Co2MnSi and coherent tunneling", Applied Physics Letters 101, 132418 (2012).
18. A. Hirohata, J. Sagar, L. R. Fleet and S. S. P. Parkin, in Heusler Compounds: Properties, Growth, Applications, edited by C. Felser and A. Hirohata (Springer International Publishing, Cham, 2016), pp. 219-248.
19. M. Julliere, Physics letters A 54, 225 (1975).
20. Y. Sakuraba, M. Hattori, M. Oogane, Y. Ando, H. Kato, A. Sakuma, T. Miyazaki and H. Kubota, "Giant tunneling magnetoresistance in Co2MnSi/Al–O/Co2MnSi magnetic tunnel junctions", Applied Physics Letters 88, 192508 (2006).
21. Y. K. Takahashi and K. Hono, in Heusler Compounds: Properties, Growth, Applications, edited by C. Felser and A. Hirohata (Springer International Publishing, Cham, 2016), pp. 295-318.
22. K. Kenji, F. Yuichi, Y. Shinya, S. Kentarou, M. Masanobu and H. Kohei, "Greatly enhanced generation efficiency of pure spin currents in Ge using Heusler compound Co2FeSi electrodes", Applied Physics Express 7, 033002 (2014).
23. E. Y. Tsymbal, O. N. Mryasov, and P. R. LeClair, Journal of Physics: Condensed Matter 15, R109 (2003).
24. G. Schmidt, D. Ferrand, L. W. Molenkamp, A. T. Filip and B. J. van Wees, "Fundamental obstacle for electrical spin injection from a ferromagnetic metal into a diffusive semiconductor", Physical Review B 62, R4790-R4793 (2000).
25. R. A. de Groot, F. M. Mueller, P. G. v. Engen and K. H. J. Buschow, "New class of materials: Half-metallic ferromagnets", Physical Review Letters 50, 2024-2027 (1983).
26. R. Fiederling, M. Keim, G. Reuscher, W. Ossau, G. Schmidt, A. Waag and L. W. Molenkamp, "Injection and detection of a spin-polarized current in a light-emitting diode", Nature 402, 787-790 (1999).
27. P. H. D. I. Galanakis, "Half-Metallic Compounds". (Springer, Berlin, 2005).

28. Buschow, K. H. J. (2001). Encyclopedia of materials: science and technology. Elsevier. ISBN 0-08-043152-6.
29. M. K. A. Hirohata, N. Tezuka, K. Inomata, J.S. Claydon, Y.B. Xu, G. van der Laan, Curr. and Opin., "", Solid State Material Society 10, 93–107 (2006).
30. K. Watanabe, Trans. Jpn. Inst. Met. 17, 220 (1976).
31. I. Galanakis, S. Ostanin, M. Alouani, H. Dreyssé, J.M. Wills, Phys. Rev. B 61, 4093 (2000).
32. E. Kulatov, I.I. Mazin, J. Phys. Condens. Matter 2, 343 (1990).
33. S.V. Halilov, E.T. Kulatov, J. Phys. Condens. Matter 3, 6363 (1991).
34. X. Wang, V.P. Antropov, B.N. Harmon, IEEE Trans. Magn. 30, 4458 (1994).
35. S.J. Youn, B.I. Min, Phys. Rev. B 51, 10436 (1995).
36. V.N. Antonov, P.M. Oppeneer, A.N. Yaresko, A. Ya, Perlov, T. Kraft, Phys. Rev. B 56, 13012 (1997).
37. M.M. Kirillova, A.A. Makhnev, E.I. Shreder, V.P. Dyakina, N.B. Gorina, Phys. Stat. Sol. (b) 187, 231 (1995).
38. K.E.H.M. Hanssen, P.E. Mijnarends, Phys. Rev. B 34, 5009 (1986).
39. K.E.H.M. Hanssen, P.E. Mijnarends, L.P.L.M. Rabou, K.H.J. Buschow, Phys. Rev. B 42, 1533 (1990).
40. F. Heusler, Verh. Dtsch. Phys. Ges. 12, 219 (1903).
41. P.J. Webster, J. Phys. Chem. Solids 32, 1221 (1971).
42. S. Ishida, S. Akazawa, Y. Kubo, J. Ishida, J. Phys. F Met. Phys. 12, 1111 (1982).
43. S. Ishida, S. Fujii, S. Kashiwagi, S. Asano, J. Phys. Soc. Jpn. 64, 2152 (1995).
44. S. Fujii, S. Sugimura, S. Ishida, S. Asano, J. Phys. Condens. Matter 2, 8583 (1990).
45. F.Y. Yang, C.H. Shang, C.L. Chien, T. Ambrose, J.J. Krebs, G.A. Prinz, V.I. Nikitenko, V.S. Gornakov, A.J. Shapiro, R.D. Shull, Phys. Rev. B 65, 174410 (2002).
46. T. Ambrose, J.J. Krebs, G.A. Prinz, Appl. Phys. Lett. 76, 3280 (2000).
47. T. Ambrose, J.J. Krebs, G.A. Prinz, J. Appl. Phys. 87, 5463 (2000).
48. T. Ambrose, J.J. Krebs, G.A. Prinz, J. Appl. Phys. 89, 7522 (2001).
49. M.P. Raphael, B. Ravel, M.A.Willard, S.F. Cheng, B.N. Das, R.M. Stroud, K.M. Bussmann, J.H. Claassen, V.G. Harris, Appl. Phys. Lett. 70, 4396 (2001).
50. M.P. Raphael, B. Ravel, Q. Huang, M.A. Willard, S.F. Cheng, B.N. Das, R.M. Stroud, K.M. Bussmann, J.H. Claassen, V.G. Harris, Phys. Rev. B 66, 104429 (2002).
51. B. Ravel, M.P. Raphael, V.G. Harris, Q. Huang, Phys. Rev. B 65, 184431 (2002).

52. L. Ritchie, G. Xiao, Y. Ji, T.Y. Chen, C.L. Chien, M. Chang, C. Chen, Z. Liu, G. Wu, X.X. Zhang, Phys. Rev. B 68, 104430 (2003).
53. Y.J. Chen, D. Basiaga, J.R. O'Brien, D. Heiman, Appl. Phys. Lett. 84, 4301 (2004).
54. P.J. Brown, K.U. Neumann, P. J .Webster, K. R. A. Ziebeck, J. Phys. Condens. Matter 12, 1827 (2000).
55. N.I. Kourov, V.V. Marchenkov, K.A. Belozerova, H.W. Weber, 2015, published in Zhurnal Eksperimental'noi i Teoreticheskoi Fiziki, 2015, Vol. 148, No. 5, pp. 966–975.
56. J. Winterlik, G. H. Fecher, B. Balke, T. Graf, V. Alijani, V. Ksenofontov, C. A. Jenkins, O. Meshcheriakova, C. Felser, G. Liu, S. Ueda, K. Kobayashi, T. Nakamura, and M. Wojcik, Phys. Rev. B. 83, 174448 (2011).
57. M. Meinert, J. M. Schmalhorst, G. Reiss, and E. Arenholz, J. Phys. D: Appl. Phys. 44, 215003 (2011).
58. H J Elmers, G H Fecher, D Valdaitsev, S A Nepijko, A Gloskovskii G Jakob, G Schönhense, S Wurmehl adn T Block, and C Felser. *Phys. Rev. B*, 67:104412, 2003.
59. B Balke, G H Fecher, H C Kandpal, C Felser, K Kobayashi, E Ikenaga, J J Kim, and S Ueda. *Phys. Rev. B*, 74:104405, 2006.
60. H. Kato, T. Okuda, Y. Okimoto, Y. Tomioka, K. Oikawa, T. Kamiyama, Y. Tokura, Phys. Rev. B 69, 184412 (2004).
61. T. Shishidou, A.J. Freeman, R. Asahi, Phys. Rev. B 64, 180401 (2001).
62. I. Galanakis, Ph Mavropoulos, Phys. Rev. B 67, 104417 (2003).
63. Ph. Mavropoulos, I. Galanakis, J. Phys. Condens. Matter 16, 4261 (2004).
64. J.H. Zhao, F.Matsukura, K. Takamura, E. Abe, D. Chiba, Y. Ohno, K. Ohtani, H. Ohno, Mat. Sci. Semicond. Process. 6, 507 (2003).
65. T. Graf, S. Parkin, and C. Felser, Prog. Solid State Chem. 39, 1 (2011).
66. S. Trudel, O. Gaier, J. Hamrle, and B. Hillebrands, J. Phys. D: Appl. Phys. 43, 193001 (2010).
67. E. Liu, W. Wang, L. Feng, W. Zhu, G. Li, J. Chen, H. Zhang, G. Wu, C. Jiang, H. Xu, and F. Boer, Nat. Commun 635, 976 (2012).
68. Galanakis, I., Dederichs, P. & Papanikolaou, N. (2002*b*). *Phys. Rev. B*, 66, 174429.
69. K Schwarz 1986 *J. Phys. F: Met. Phys.* 16 L211.
70. Hiro Akinaga *et al* 2000 *Jpn. J. Appl. Phys.* 39 L1118.
71. J. E. Pask, L. H. Yang, C. Y. Fong, W. E. Pickett, and S. Dag. Phys. Rev. B 67, 224420 (2003).

72. S.Wurmehl, H.C. Kandpal, G.H. Fecher, C. Felser, J. Phys. Condens. Matter 18, 6171 (2006).
73. H. van Leuken and R. A. de Groot, Phys. Rev. Lett. 74(7) (1995).
74. M. Shaughnessy, C.Y. Fong, L.H. Yang, C. Felser, Preprint arXiv:1108.3651 (2011).
75. B. Balke, G.H. Fecher, J. Winterlik, C. Felser, Appl. Phys. Lett. 90, 152504 (2007).
76. J. Winterlik, B. Balke, G.H. Fecher, C. Felser, M.C.M. Alves, F. Bernardi, J. Morais, Phys. Rev. B 77, 054406 (2008).
77. K. Özdoğan, I. Galanakis, J. Magn. Magn. Mater. 321, L34 (2009).
78. I. Galanakis, K. Özdoğan, E. ¸Şaşıoğlu, B. Akta¸s, Phys. Status Sol. (a) 205, 1036 (2008).
79. I. Galanakis, K. Özdoğan, E. ¸Şaşıoğlu, B. Akta¸s, Phys. Rev. B 75, 92407 (2007).
80. H. Luo, L. Ma, Z. Zhu, G. Wu, H. Liu, J. Qu, Y. Li, Physica B 403, 1797 (2008).
81. W.E. Pickett, Phys. Rev. B 57, 10613 (1998).
82. J.H. Park, S.K. Kwon, B.I. Min, Phys. Rev. B 65, 174401 (2002).
83. M. Uehara, M. Yamada, Y. Kimishima, Solid. State Commun. 129, 385 (2004).
84. Y.K. Wang, G.Y. Guo, Phys. Rev. B 73, 064424 (2006).
85. V. Pardo, W.E. Pickett, Phys. Rev. B 80, 054415 (2009).
86. M. Nakao, Phys. Rev. B 74, 172404 (2006).
87. M. Nakao, Phys. Rev. B 77, 134414 (2008).
88. H. Akai, M. Ogura, Phys. Rev. Lett. 97, 026401 (2006).
89. N.H. Long, M. Ogura, H. Akai, J. Phys. Condens. Matter 21, 064241 (2009).
90. M. Nakao, Phys. Rev. B 83, 214404 (2011).
91. S. Tirpanci, E. Şaşıoğlu, I. Galanakis, J. Appl. Phys. 113, 043912 (2013).
92. T. Graf, C. Felser, and S. S. P. Parkin, Prog. Solid State Chem. 39, 1 (2011).
93. J.S. Moodera, G.-X. Miao, T.S. Santos, Phys. Today 63, 46 (2010).
94. G.-X. Miao, M. Münzenberg, J.S. Moodera, Rep. Prog. Phys. 74, 036501 (2011).
95. I. Galanakis, K. Özdoğan, E. ¸ Şaşıoğlu, Appl. Phys. Lett. 103, 142404 (2013).
96. I. Galanakis, K. Özdoğan, E. ¸ Şaşıoğlu, J. Phys. Condens. Matter 26, 086003 (2014).
97. I.M. Tsidilkovski, *Electron Spectrum of Gapless Semiconductors*. Springer Series in Solid-State Sciences, vol. 116, ed. by von K. Klitzing (Springer, New York, 1996)
98. X.L. Wang, Phys. Rev. Lett. 100, 156404 (2008).
99. X. Wang, G. Peleckis, C. Zhang, H. Kimura, S. Dou, Adv. Mater. 21, 2196 (2009).
100. D.H. Kim, J. Hwang, E. Lee, K.J. Lee, S.M. Choo, M.H. Jung, J. Baik, H.J. Shin, B. Kim, K. Kim, B.I. Min, J.-S. Kang, Appl. Phys. Lett. 104, 022411 (2014).

101. G.Z. Xu, E.K. Liu, Y. Du, G.J. Li, G.D. Liu, W.H. Wang, G.H. Wu, Europhys. Lett. 102, 17007 (2013).

102. S. Skaftouros, K. Özdoğan, E. Şaşıoğlu, I. Galanakis, Appl. Phys. Lett. 102, 022402 (2013).

103. G.Y. Gao, K.-L. Yao, Appl. Phys. Lett. 103, 232409 (2013).

104. S. Ouardi, G.H. Fecher, C. Felser, J. Kübler, Phys. Rev. Lett. 110, 100401 (2013).

105. I. Galanakis, K. Özdoğan, E. ¸ Şaşıoğlu, S. Blügel, J. Appl. Phys. 115, 093908 (2014)

106. S. Wurmehl, G.H. Fecher, H. C. Kandpal, V. Ksenofontov, C. Felser, H- J. Lin, and J. Morais, Phys. Rev. B 72 (2005) 184434.

107. K.A. Killan, R.H. Victora, J. Appl. Phys. 87 (2000) 7064.

108. K. Özdoğan, E. Şaşıoğlu, I. Galanakis, Phys. St. Sol. (RRL) 1, 184 (2007).

109. I. Galanakis, E. Şaşıoğlu, K. Özdoğan, S. Blügel, Phys. Rev. B 90, 064408 (2014).

110. Ishida S, Masaki T, Fujii S and Asano S 1998 Physica B 245 1.

111. Picozzi S, Continenza A and Freeman A J 2002 Phys. Rev. B 66 094421.

112. Kellow A, Fenineche N E, Grosdidier T, Aourag H and Coddet C 2003 J. Appl. Phys. 94 3292.

113. Ishida S, Kawakami S and Asano S 2004 Mater. Trans. JIM 45 1065.

114. Miura Y, Nagano K and Shirai M 2004 Phys. Rev. 69 144413.

115. Ishida S, Sugimura S, Fujii S and Asano S 1991 J. Phys.: Condens. Matter 3 5793.

116. Umetsu R Y, Kobayashi K, Kainuma R, Fujita A, Fukamichi K, Ishida K and Sakuma A 2004 Appl. Phys. Lett. 85 2011.

117. H. C. Kandpal, G. H. Fecher and C. Felser, Phys. Rev. B 73, 094422 (2006).

118. H. M. Huang, S. J. Luo and K. L. Yao, J. Phys. B 406, 1368 (2011).

119. Gercsi Z, Rajanikanth A, Takahashi Y K, Honob K, Kikuchi M, Tezuka N and Inomata K 2006 Appl. Phys. Lett. 89 082512.

120. Marukame T, Ishikawa T, Matsuda K I, Uemura T and Yamamoto M 2006 Appl. Phys. Lett. 88 262503.

121. S. Wurmehl, G. H. Fecher, H. C. Kandpal, V. Ksenofontov, C. Felser, and H.-J. Lin, Applied physics letters 88, 032503 (2006).

122. E. Şaşıoğlu, L. Sandratskii, and P. Bruno, Journal of Physics: Condensed Matter 17, 995 (2005).

123. B. K. Hazra, M. M. Raja, and S. Srinath, "Correlation between structural, magnetic and transport properties of Co2FeSi thin films," J. Phys. Appl. Phys. 49(6), 65007 (2016).

124. L. Feng, E. K. Liu,W. X. Zhang,W. H.Wang, and G. H.Wu, "First-principles investigation of half-metallic ferromagnetism of half-Heusler compounds XYZ," J. Magn. Magn. Mater. 351, 92–97 (2014).

125. R. Umamaheswari, M. Yogeswari, and G. Kalpana, "Ab-initio investigation of half-metallic ferromagnetism in half-Heusler compounds XYZ (X=Li, Na, K and Rb; Y=Mg, Ca, Sr and Ba; Z=B, Al and Ga)," J. Magn. Magn. Mater. 350, 167–173 (2014).

126. A. W. Carbonari, R. N. Saxena, W. Pendl, Jr., J. Mestnik Filho, R. N. Attili, M. Olzon-Dionysio, and S. D. de Souza, "Magnetic hyperfine field in the Heusler alloys Co_2YZ (Y = V, Nb, Ta, Cr; Z = Al, Ga)," J. Magn. Magn. Mater. 163(3), 313–321 (1996).

127. D. I. Bilc, H. Geoffroy, W. David, G. M. Rignanese, P. Ghosez, Low-Dimensional Transport and Large Thermoelectric Power Factors in Bulk Semiconductors by Band Engineering of Highly Directional Electronic States, Phys. Rev. Lett. 114(2015) 136601.

128. T. Gasi et al., Physical Review B 87, 064411 (2013).

129. L. Hongzhi, Z. Zhiyong, M. Li, X. Shifeng, L. Heyan, Q. Jingping, L. Yangxian, W. Guangheng, J. Phys. D: Appl. Phys. 40, 7121 (2007).

Chapter II

Basics of Heusler Compounds

II.1 Heusler compounds

The birth of Heusler alloys recurs to the early nineties when Friedrich Heusler [1] discovered the ferromagnetic Cu_2MnAl alloy [2]. This remarkable compound crystallizing in L_{21} structure was only the beginning of the rise of thousands of compounds namely Heusler alloys. It is the atomic combination of diamagnetic and paramagnetic elements that defines and differentiates the properties of each compound from the other, leading to amazing magnetic phenomena like metallicity, half-metallicity [3], semiconducting, superconductivity and topological insulators [4].

Except the usual full Heusler compounds, there exists the so-called inverse full Heusler structure. These compounds have also the chemical formula X_2YZ, but in their case, the valence of X transition metal atom is smaller than the valence of Y atom. Several inverse Heuslers have been studied using first-principles electronic structure calculations [5-8], also by experiment [9,10], and many of them have been identified to be half-metallic ferromagnets [11].

Quaternary Heusler alloys are a special case of full Heuslers, where one site is occupied randomly by two chemical elements. Almost a decade ago, first-principles calculations have been employed to study the electronic and magnetic properties of 60 LiMgPdSn-type multifunctional quaternary Heuslers [12]. It was shown that most of these compounds were half-metals obeying the same Slater-Pauling rule for full Heuslers ($M_t = Z_t - 24$), with few exceptions.

Other from the full Heuslers mentioned above, there exists another type of ternary Heuler compounds called the half-Heuslers with the composition XYZ. The most well-known half-Heusler compound is NiMnSb [13]. It has attracted a lot of experimental interest since, in 1983, de Groot and his collaborators [14] showed, using first-principles calculations that this compound is in reality half-metallic.

II.2 Crystal structure of Heusler compounds

Usually, Heusler compounds can be categorized into two main groups; one with the composition 1:1:1 (half-Heuslers) and the other with stoichiometry 2:1:1 (full Heuslers). Mostly, X and Y elements represent different transition metals, while Z atom is either a nonmagnetic metal or a semiconductor [15]. The compounds of the first family are ternary materials with the general formula XYZ, and they are called Half-Heuslers (HH). HH compounds crystallize in a non-centrosymmetric cubic structure with space group F43m (216). In fact, the crystal structure is a sum of the zinc blende (covalent) and the sodium chloride (ionic) lattice. The corresponding occupied Wyckoff positions are (0, 0, 0), (1/2, 1/2, 1/2) and (1/4, 1/4, 1/4), where the most electropositive atom and the main group element occupy the octahedral sites, while tetrahedral sites are occupied by the other transition metal element. Whereas X_2YZ Heusler compounds follow the L_{21} structure with the atomic positions (0, 0, 0), (1/2, 1/2, 1/2), (1/4, 1/4, 1/4) and (3/4, 3/4, 3/4). The unit cell consists of four face centered cubic sublattices and belongs to the space group Fm3m (225). A rock salt-type lattice is formed by the least and the most electropositive elements (Y and Z). Due to the ionic character of their interaction, these elements are coordinated octahedrally. On the other hand, all tetrahedral holes are filled by X atoms.

When the atomic number of Y element is greater than that of X [16], an inverse Heusler structure is obtained. Inverse Heuslers have also the chemical formula X_2YZ and the structure is still described by four interpenetrating face-centered-cubic (fcc) sublattices, but in this case, X and Z atoms form a rock salt lattice to achieve an octahedral coordination for X. The remaining X and Y atoms fill the tetrahedral holes with fourfold symmetry. As a consequence, the inverse Heusler compounds crystallize in the so-called XA or Xα structure, where the sequence of the atoms is X-Y-X-Z and the prototype is Hg_2TiCu [17].

Except the usual and inverse full Heusler compounds, another full Heusler family is the quaternary one, also known as LiMgPdSn-type of Heuslers [18], with the chemical formula XX'YZ where X, X' and Y are transition metal atoms, and Z is a main group element. The valence of X' is lower than the valence of X atoms, and the valence of Y element is lower than the valence of both X and X'. The sequence of the atoms along the fcc cube's diagonal is X-Y-X'-Z, which is energetically the most stable [19] (see table II.1).

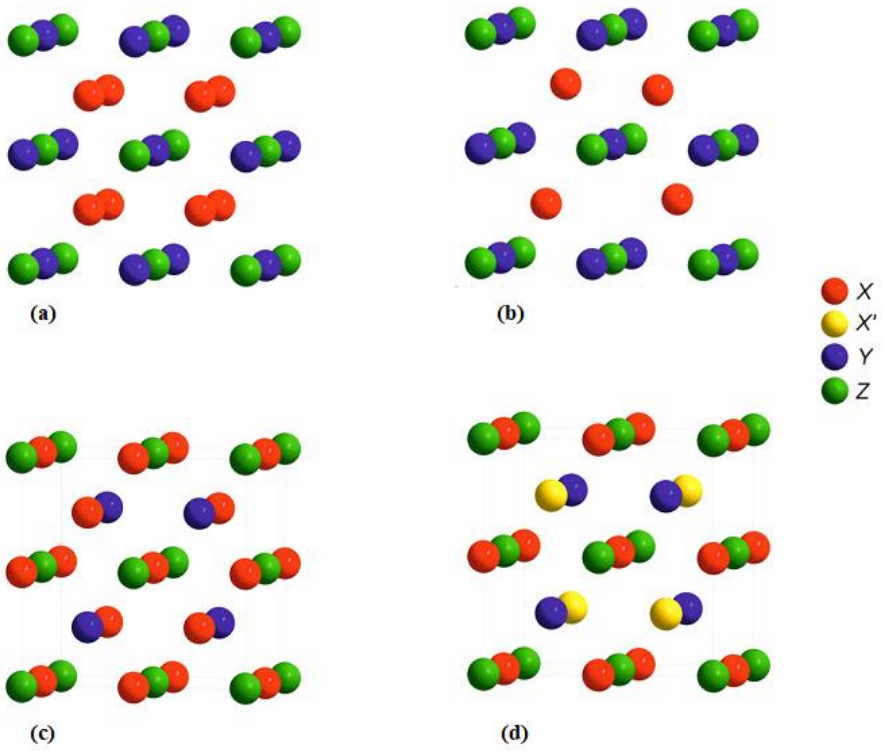

Figure II.1 Heusler structures (a) The full Heusler structure, (b) the half-Heusler structure, (c) the inverse Heusler structure and (d) the quaternary Heusler structure [62].

Table II.1 Atomic positions of the half-, full-, inverse and quaternary Heusler structures.

	(1/4, 1/4, 1/4)	***(3/4, 3/4, 3/4)***	***(1/2, 1/2, 1/2)***	***(0, 0, 0)***
Half Heusler XYZ	*X*		*Y*	*Z*
Full Heusler X_2YZ	*X*	*X*	*Y*	*Z*
Inverse Heusler XYXZ	*X*	*Y*	*X*	*Z*
Quaternary Heusler XX'YZ	*X*	*X'*	*Y*	*Z*

II.3 Disorder and defects

As mentioned in the previous chapter, the properties of Heusler compounds strongly depend on the atomic order. Larson et al [20] have shown that the ordered structure of Heusler alloys is the one with the minimum energy and thus the most stable. There are several derivatives of the initial ideal Heusler structures (figure (II.1)), due either to atomic swaps or to disorder [21]. Vacancies are also a very common defect occurring during the growth of samples of Heusler compounds. Usually, moderate degrees of disorder and doping do not alter half-metallicity. Also defects with low formation energies, which are the most likely to occur; keep the half-metallic character of the compounds. Yet, in [22], it was shown for several families of Heuslers that the occurrence of vacancies at the sites occupied by the higher valence transition metal atoms alters the local environment of the atoms, destroying the half-metallic character of the compounds under study.

Half-Heusler compounds are tetrahedrally filled structures that are closely related to binary semiconductors. Covalent bonding interaction plays a significant role and their crystalline order is retained up to the composition temperature [23]. Thus, structural disorder, that leads to occupation of the vacant lattice site, occurs only rarely in Half-Heusler compounds, whereas X_2YZ phases often display considerable amounts of atomic disorder.

Within the Half-Heusler structure, different types of atomic disorder are possible. An overview of potential types of disorder is displayed in figure (II.2) and a detailed description of all possible atomic arrangements with the Heusler structure can be found in [24]. A mixture of the atoms on Wyckoff positions 4a and 4b leads to a CaF_2-type structure (C1, space group Fm3m, no 225). In contrast to this, the vacant sites can partially become occupied, while at the same time, vacancies are introduced in the other sublattices. Hence, a partial occupancy of the 4d sites accompanied by voids on the 4c sites yields a Cu_2MnAl-type structure (L_{21}, space group Fm3m, no 225) and an additional mixing of the atoms on positions 4a and 4b leads to a CsCl type of disorder (B2, Pm3m, no. 221). On the other hand, if the vacant lattice site is partially occupied by atoms from 4b site accompanied by an intermixing of 4a and 4c positions, a NaTl-type structure is obtained (B32a, Fd3m, no. 227). Finally, a completely random distribution of all three atoms on the four possible positions gives rise to a tungsten-type disorder (W, Im3m, no. 229).

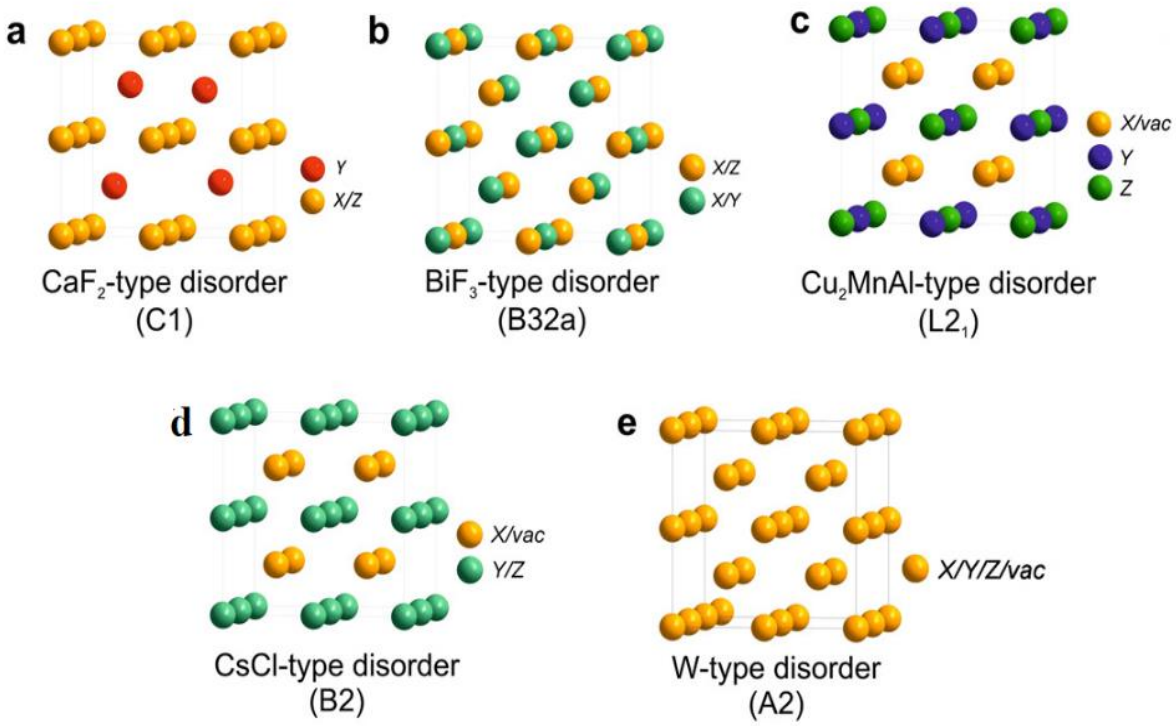

Figure II.2 Types of disorder in the Half-Heusler structure: (a) CaF2-type disorder, (b) NaTl-type disorder, (c) Cu_2MnAl-type disorder, (d) CsCl-type disorder, and (e) tungsten-type disorder [62].

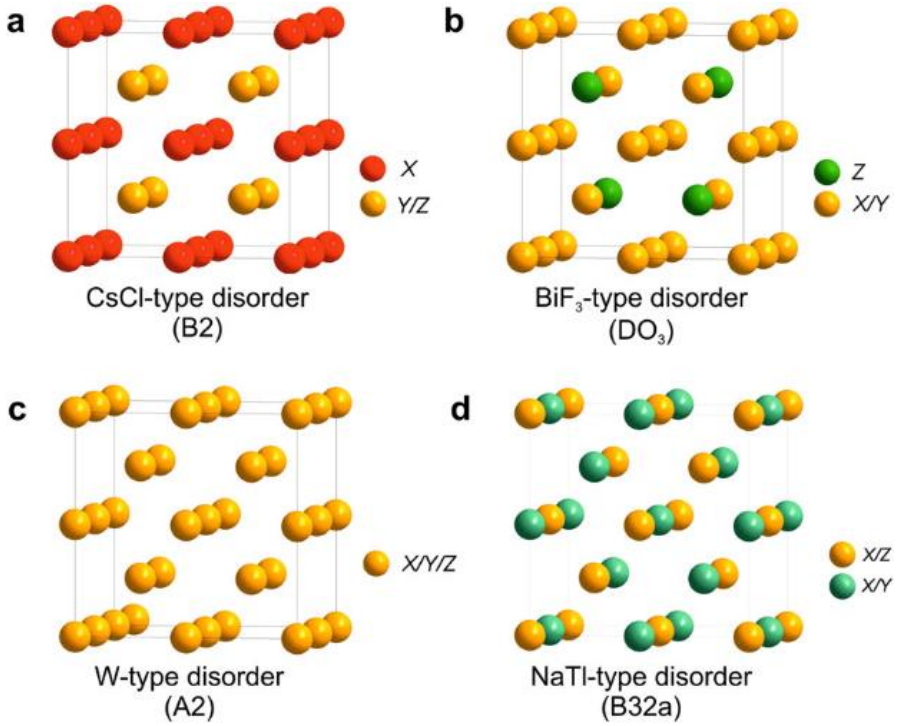

Figure II.3 Different types of disorder in the Heusler structure: (a) CsCl-type disorder, (b) BiF3-type disorder, (c) NaTl-type disorder, and (d) tungsten-type disorder [62].

In the case of full Heusler compounds, band structure calculations show that already small amounts of disorder within the distribution of the atoms on the lattice sites cause distinct changes in their electronic structure and also in their magnetic and transport properties [25,26]. Therefore, a careful analysis of their crystal structure is essential to understand the structure-to-property relation of Heusler compounds.

Figure (II.3) shows the transition from the ordered to the most prominent disordered Heusler structures, which will be explained in the following [27-29]: If Y and Z atoms are evenly distributed, 4a and 4b positions become equivalent. This leads to a CsCl-like structure, also known as B2-type disorder. Consequently, the symmetry is reduced and the resulting space group is Pm3m.

On the other hand, the random distribution of X and Y or X and Z leads to a BiF3-type disorder (Space group no. 216: Fm3m, DO_3). Different from these types of disorder, the NaTl-type structure is observed very rarely. In this structure type, X atoms, which occupy one of the fcc sublattices, are mixed with Y atoms, whereas X atoms on the second sublattice are mixed with Z atoms. This kind of disorder is also known as B32a disorder (Space group no. 227, Fd3m). Here, X atoms are placed at the Wyckoff position 8a (0, 0, 0), while Y and Z are randomly distributed at position 8b (1/2, 1/2, 1/2).

In contrast to these partial disorder phenomena, all positions become equivalent in the tungsten-type structure with a base-centered-cubic (bcc) lattice and reduced symmetry (Im3m (A2)).

All disorder types, which can be found in the Heusler structure, may also occur in Half-Heusler compounds, where the vacancy is statistically distributed on all positions. Only in the CaF2-type disorder, the vacant site is preserved.

We point out that the chemical disorder occurring in the Heusler structure is the reason why experimental results differ from theoretical predictions of first-principle calculations, since these last ones are based on a perfect crystal.

II.4 Magnetic properties of Heusler compounds

The XYZ materials exhibit one magnetic sublattice, since only the atoms on the octahedral sites can carry a magnetic moment. However, X_2YZ compounds have two magnetic sublattices that can couple ferromagnetically or antiferromagnetically (figure (II.4)). Thus, full Heuslers can show all kinds of magnetic phenomena, such as ferromagnetism, antiferromagnetism, ferrimagnetism, helimagnetism, Pauli paramagnetism and heavy fermion behavior [30-33]. The crystal structure, composition and heat treatment were found to be important parameters for determining the magnetic properties of Heuslers. In fact, it has been shown that the s-p electron concentration plays an important role in establishing the magnetic properties, including the total magnetic moment, the structural stability, and the type of magnetic order. In addition, the properties of Heusler compounds strongly depend on the atomic order, especially the X atom site.

The majority of Heusler compounds order ferromagnetically and saturate in weak applied magnetic fields. Nevertheless, there exists some Heuslers that order antiferromagnetically, and many studies reported the antiferromagnetic behavior in several B2-type disordered X_2MnZ (X=Ni, Pd; Z=Al, In) Heusler alloys [34]. Although antiferromagnetism is more favorable in full Heusler alloys with B2-type structure, experimentally, antiferromagnetic order has been measured both in half-Heusler ($C1_b$ structure) and in full Heusler alloys (L_{21} and B2 structure). In comparison to ferromagnetic or antiferromagnetic behavior, ferrimagnetic ordering is very rare in Heusler alloys. Actually only CoMnSb, Mn_2VAl and Mn_2VGa compounds have been detected to be ferrimagnetic alloys, and Mn_2VAl [35] received the most experimental attention. The properties of Heusler alloys can easily be predicted by simply counting the number of valence electrons [36], which leads us to an important criteria used as an indicator of the half-metallic character in Heusler compounds.

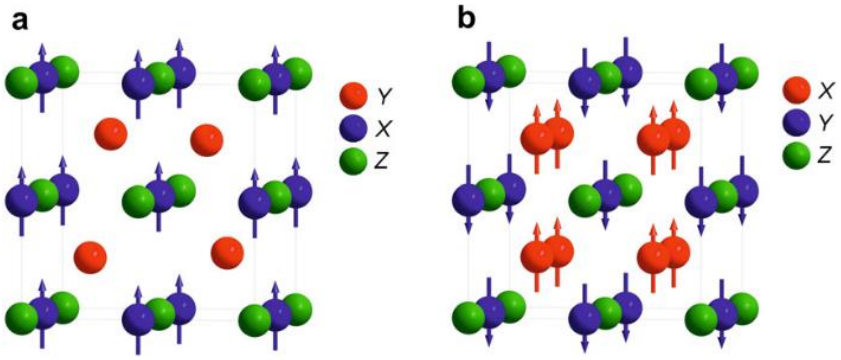

Figure II.4 Types of interactions in (a) XYZ Half Heusler compounds exhibiting only one magnetic sublattice, (b) X_2YZ Heusler compounds having two magnetic sublattices [62].

- The Slater Pauling rule

Based on the Slater Pauling behavior [37,38], the total magnetic moment M_t can be estimated by following a simple electron counting rule. For half- and full Heuslers, the total magnetic moment is given by $\mathbf{M_t = Z_t - 18}$, and $\mathbf{M_t = Z_t - 24}$, respectively, where Z_t is the total number of valence electrons.

The Slater-Pauling rule is also valid for quaternary Heusler compounds [39]. In figure (II.5), we present the Slater Pauling curve for the ternary and quaternary Heusler materials studied in this thesis.

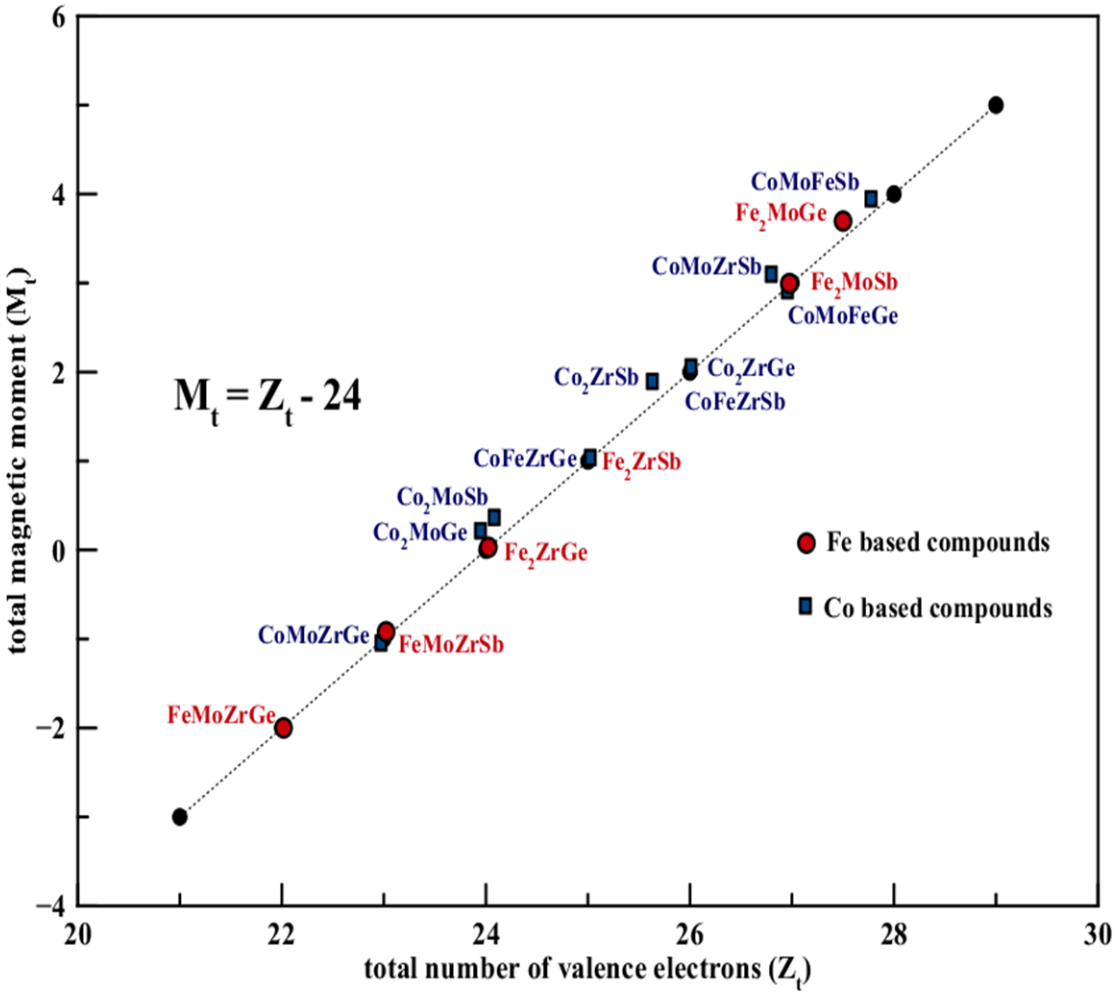

Figure II.5 Slater Pauling curve for the ternary X2YZ (X = Fe, Co; Y = Zr, Mo; Z = Ge, Sb) and quaternary XX'YZ (X = Co, Fe; X' = Mo, Fe; Y = Zr, Fe; Z = Sb, Ge) Heusler alloys.

II.5 Elastic properties

The elastic properties reflect the response of a particular material to elastic or non-elastic deformation when a stress load is applied. Investigating the mechanical properties is crucial to provide information about the stiffness and stability of a material, hence estimating its different practical usages.

Cubic crystals have only three independent elastic constants, namely, C_{11}, C_{12}, and C_{44}. The two cubic elastic constants C_{11} and C_{12} are derived from the bulk modulus B, as:

$$\mathbf{B} = \frac{(\mathbf{C_{11}+2C_{12}})}{\mathbf{3}}, \quad \text{(II-1)}$$

Moreover, the bulk modulus can be extracted from the equation of state described by a Morse function [40] fitted to the total energy, by:

$$\mathbf{B} = \mathbf{V}\frac{\partial^2 \mathbf{E}}{\partial \mathbf{V}^2} \quad \text{(II-2)}$$

The necessary and sufficient mechanical stability conditions of the elastic constants for a cubic crystal are the so called Born-Huang criteria [41], defined as:

$$\mathbf{C_{44}} > \mathbf{0} \quad \text{(II-3)}$$

$$\mathbf{B} > \mathbf{0} \quad \text{(II-4)}$$

$$\frac{(\mathbf{C_{11}-C_{12}})}{\mathbf{2}} > \mathbf{0} \quad \text{(II-5)}$$

$$\mathbf{C_{12}} < \mathbf{B} < \mathbf{C_{11}} \quad \text{(II-6)}$$

After determining the elastic constants, one can calculate other important elastic moduli, such as the shear modulus, anisotropy and Young's modulus through the following equations:

$$\mathbf{A} = \frac{\mathbf{2C_{44}}}{\mathbf{C_{11}-C_{12}}}, \quad \text{(II-7)}$$

$$\mathbf{E} = \frac{\mathbf{9BG}}{\mathbf{3B+G}}, \quad \text{(II-8)}$$

$$\mathbf{G} = \frac{(\mathbf{G_R+G_V})}{\mathbf{2}}, \quad \text{(II-9)}$$

Where G_R and G_V are Reuss's [42] and Voigt's [43] shear moduli of a cubic crystal, respectively, given by:

$$\mathbf{G_R} = \frac{\mathbf{5C_{44}(C_{11}-C_{12})}}{\mathbf{4C_{44}+3(C_{11}-C_{12})}}, \quad \text{(II-10)}$$

and:

$$\mathbf{G_V} = \frac{\mathbf{C_{11}-C_{12}+3C_{44}}}{\mathbf{5}}, \quad \text{(II-11)}$$

The value of Young's modulus generally shows how materials respond along the edges when strain is applied, and describes their stiffness. In fact, the higher the value of E, the higher will be the stiffness.

The Cauchy pressure is used as an indicator of the brittle-ductile behavior, it is expressed as:

$$\mathbf{C_p = C_{12} - C_{44}} \quad \text{(II-12)}$$

Negative $\mathbf{C_p}$ has been associated with covalent nature of the metallic bond and is characteristic to brittle alloys, whereas positive $\mathbf{C_p}$ indicates metallic character and enhanced ductility [44]. A second indicator of the brittle-ductile behavior is Pugh's ratio [45], given by:

$$\mathbf{k = B/G} \quad \text{(II-13)}$$

and Poisson's ratio υ,

$$\boldsymbol{\upsilon} = \frac{\mathbf{1}}{\mathbf{2}}\frac{\mathbf{(3B-2G)}}{\mathbf{(3B+G)}} = \frac{\mathbf{3B-E}}{\mathbf{6B}} \quad \text{(II-14)}$$

Pugh's and Poisson's ratio give valuable expectations of the malleability in materials. The ratio of bulk and shear modulus [46] can also be used to examine the brittle and ductile behavior [47] for covalent and ionic materials. Small values of Pugh's ratio indicate low malleability of crystals. High values of $\mathbf{B/G}$ (above 1.75) indicate the material is ductile.

Ductile materials have a wide range of applications in the parts of machine undergoing rapid acceleration. Another factor that gives information about the brittle/ductile nature of a given material is Poisson's ratio. It usually ranges between 0.25 and 0.35 for solids such as metals, polymers and ceramics [48]. According to the Frantsevich rule [49], Poisson's ratio is less than 0.26 for brittle alloys, while materials having a value above 0.26 are observed to be ductile.

Anisotropy factor [50] is considered as the signifier of instability of cubic structures. The large anisotropy of crystals correlates to the possibility of micro-cracks in materials, since it shows the tendency of a system toward phase transitions.

It is also important to mention that the value of elastic anisotropy must be unity for an isotropic crystal, while any value less or greater than 1 indicates the system is anisotropic [51].

- Prediction of the melting temperature

The melting point of a substance is the temperature at which it changes state from solid to liquid. At this point, the solid and liquid phases exist in equilibrium. For cubic crystals, Fine et al. [52] showed that there is a rough correlation between the average elastic constant and the melting temperature as follows:

$$\boldsymbol{T_{melt} = [553K + \left(\frac{5.91K}{GPa}\right) C_{11}] \pm 300K} \quad \text{(II-15)}$$

II.6 Thermoelectric properties

Thermoelectric (TE) effects have been well known since the discoveries of Thomas Seebeck in the early 19th century [53]. When a material is subject to a temperature gradient, high-energy carriers residing in hot regions tend to diffuse to the cold ones, producing a charge build-up and an electrostatic potential difference. In open-circuit conditions, such a process continues until drift and diffusion currents balance and a Seebeck voltage is established.

The term "thermoelectric effect" encompasses three separately identified effects: the Seebeck effect (creating a voltage from temperature difference), Peltier effect (driving heat flow with an electric current) and Thomson effect (reversible heating or cooling within a conductor when there is both an electric current and a temperature gradient).

TE effects provide a very interesting way to convert waste heat into useful energy (see figure (II.6)) using a solid-state converter: this possibility has been widely explored since the 1950s, but in practice, TE devices have been relegated so far to a small group of niche scientific, medical, or military applications. The key reason for such a limited diffusion of this technology fundamentally lies in the relatively low thermodynamic efficiency of existing TE devices.

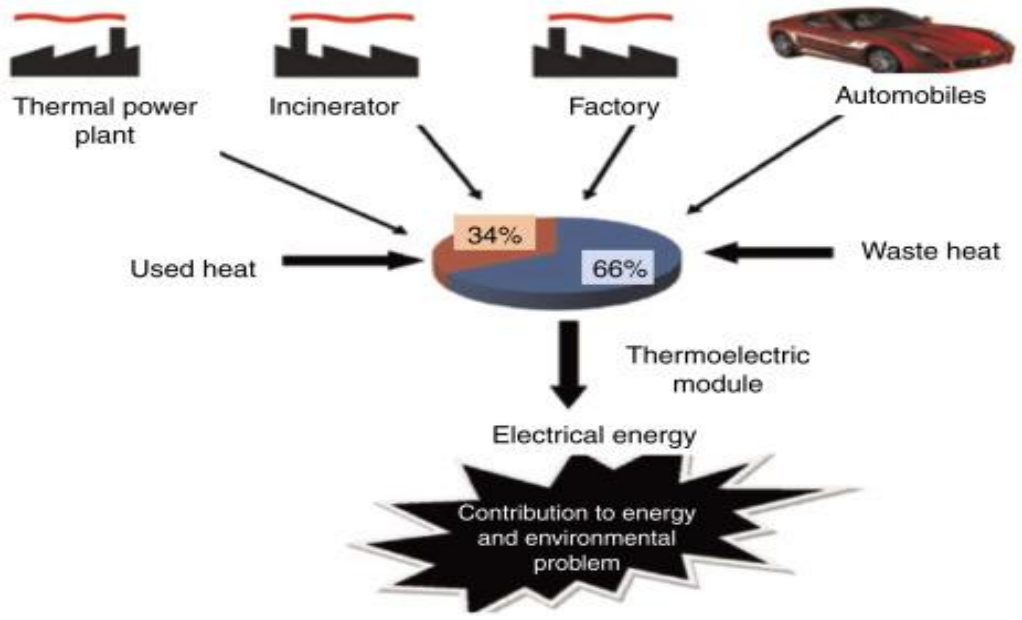

Figure II.6 Overview of energy conversion from various sources using TE device.

While all materials have a nonzero thermoelectric effect, in most materials it is too small to be useful. However, low-cost materials that have a sufficiently strong thermoelectric effect (and other required properties) are also considered for applications including power generation and refrigeration.

The performance of thermoelectric materials can be determined by the parameter thermoelectric figure-of-merit (ZT) and fabricating those better materials with higher ZT value (c. ZT > 1) is the challenging one for the proper usage of thermal energy against refrigeration and electrical power generation.

The performance of thermoelectric materials is often defined by the following dimensionless figure of merit [54]:

$$\mathbf{ZT} = \frac{\mathbf{TS^2\sigma}}{\mathbf{k}}, \qquad \text{(II-16)}$$

Here: $\boldsymbol{S}$ is the Seebeck coefficient, $\boldsymbol{\sigma}$ is the electrical conductivity, **T** the absolute temperature and **k** the thermal conductivity: $\mathbf{k} = \mathbf{k_{electronic}} + \mathbf{k_{lattice}}$. Since the thermoelectric figure of merit is directly related to the efficiency of a thermoelectric generator, it makes it very convenient parameter to compare the potential effectiveness of converters, which uses different materials. Values of about ZT = 1 at room temperature are now considered as good values and allow to achieve efficiency of the order of 8 %. Increasing the figure of merit up to 2-3 would increase the efficiency of thermoelectric converters to about 20 % and expand their applications. While ZT values of about 3-4 seem to be sufficient so that the thermoelectric device can compete in efficiency with electric generators and cooling units of conventional design. Equation (II-16) shows that the Seebeck coefficient and the electrical conductivity are directly proportional to ZT.

Efficient thermoelectric materials are characterized by a large Seebeck coefficient, high conductivity, and low thermal conductivity at the same time.

The Seebeck coefficient and electrical conductivity are determined mainly by the electronic properties of the material. By combining these two physical quantities, we get a single value called the power factor, which is defined by the relation:

$$\boldsymbol{PF = S^2\sigma/\tau}, \qquad \text{(II-17)}$$

From this relation, one can see that the power factor increases with increasing conductivity and Seebeck coefficient. The spin dependent Seebeck coefficient (S) is used to designate the material characteristics from the application perspectives.

The total thermopower generated from materials can be estimated by taking into consideration the conductivities [55,56] and Seebeck coefficients of both spin channels, as:

$$\mathbf{S} = \frac{\mathbf{S_{\uparrow}\sigma_{\uparrow} + S_{\downarrow}\sigma_{\downarrow}}}{\boldsymbol{\sigma_{\uparrow} + \sigma_{\downarrow}}} \quad \text{(II-18)}$$

Here $\sigma_{\uparrow}$, $\sigma_{\downarrow}$ are the electrical conductivities, and $S_{\uparrow}$, $S_{\downarrow}$ are the Seebeck coefficients of spin up and spin down channels, respectively.

While the overall temperature dependent behavior of the electrical conductivity [57] is calculated by combining the contributions from both spin channels as follows:

$$\boldsymbol{\sigma = \sigma_{\uparrow} + \sigma_{\downarrow}} \quad \text{(II-19)}$$

The effective thermal conductivity has a contribution from two parameters namely electronic thermal conductivity (k_e) and lattice thermal conductivity (k_l), where: $k_{tot} = k_e + k_l$.

The lattice thermal conductivity k_l can be estimated using the Slack equation [58]:

$$\boldsymbol{k_l = \frac{A\theta_D V^{1/3} m}{\gamma^2 n^{2/3} T}}, \quad \text{(II-20)}$$

Where: A is a physical constant (A ~ 3.1 *10^{-6}), γ is the Grüneisen parameter, θ_D the Debye temperature, V is the volume per atom, n is the number of atoms in the primitive unit cell, and m is the average mass of the atoms in the crystal.

Thermoelectric materials are believed to overcome the energy crisis as this method is not only environment friendly, but it is also capable of generating electric energy from waste heat. A schematic figure of a TE device is shown in figure (II.7). It consists of n- and p-type TE materials connected in series electrically with metal electrodes and arranged thermally in parallel.

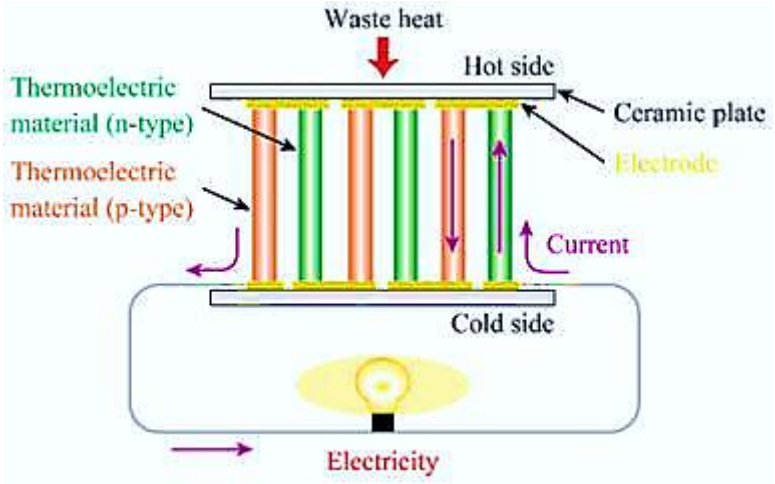

Figure II.7 Schematic figure of a thermoelectric (TE) power generation device.

Since the fundamental physical limits of thermoelectric conversion efficiency are unknown, a lot of attention is now being paid to the search for new thermoelectric materials with improved parameters. In order to achieve good thermoelectric performance, we need to minimize the thermal conductivity of materials, while enhancing their electrical conductivity. Finding an efficient and high temperature thermoelectric material with such requirements is difficult to be satisfied, because the three parameters are functions of carrier concentration, which cannot be tuned independently.

The Seebeck coefficient S decreases with carrier concentration n, whereas the conductivity σ increases. As a result, conventional metals have a very small Seebeck coefficient and a relatively high thermal conductivity, while insulators show a very high electrical resistivity. For this reason, the most favorable materials for thermoelectric applications are usually semiconductors having a Fermi level near the band gap.

A variety of TE materials have been explored, such as chalcogenides, skutterudites, clathrates, silicides, Zintl compounds, half-Heusler compounds and oxides [59-61]. Most of these materials are semiconductors because in general they have high Seebeck coefficients than metals. However, recent theoretical and experimental studies have revealed that metals, in particular, half-metallic full-Heusler compounds have relatively high Seebeck coefficients as well as high electrical conductivities. In addition, their junction with a metal electrode is robust compared to that of semiconductors, which is also an advantage.

II.7 Applications of Heusler alloys

The robustness of Heusler compounds lies at the fact that their structural and physical properties can be tuned in an exotic way. Hence, they are used in different fields of applications including spintronics [62-64], ferromagnetic shape memory alloys [65,66], thermoelectrics [67,68] and topological insulators [69,70].

II.7.1 Heusler alloys in the field of data storage

In chapter I, we have already mentioned that the discovery of the GMR effect [71,72] gave birth to a new research field, namely "spintronics." The advantages of spintronic devices include non-volatility, increased data processing speed, large storage density, and low energy consumption. To enhance their competition versus semiconducting devices, half-metallic ferromagnets (HMF) with high spin polarization are essential. This half-metallic property found in many Heusler compounds enables them to be promising materials for spintronic devices such as magnetic hard disks, magnetic random access memories, and magnetic sensors.

The discovery of the half-Heusler compound NiMnSb [73] suggested the possibility of dramatic magneto-resistance (MR) enhancement of the GMR/TMR devices by using Heusler compounds as electrodes. However, the first MTJ with NiMnSb epitaxial electrode yielded MR ratios as low as 9% at room temperature and 18% at low temperature [74], respectively. This low MR ratio was attributed to the atomic-disorder, which leads to the diminishing of the half-metallic gap around Fermi level (Ef) [75]. Similar low MR effect was reported for devices employing other half-Heusler compounds, for example, PtMnSb in GMR spin-valves [76-79].

Later on, research interest was shifted to Co-based full Heusler compounds due to their expected larger MR effect, because they were shown to possess more stable half-metallicity in both theory and experiment [80-84]. The early successful demonstration of large MR values in the quaternary $Co_2Cr_{0.6}Fe_{0.4}Si$-based MTJs triggered enormous efforts focusing on the incorporation of the Co-based full Heusler compounds into both GMR and TMR devices [85], leading to a tremendous increase in the MR ratio during the recent decade [86,87]. In addition to the high spin polarization and high Curie temperature (Tc), Co-based Heusler compounds such as Co2FeAl and $Co_2Fe_xMn_{1-x}Si$, have a much lower saturation magnetization and damping constant compared with those of the conventional ferromagnetic materials [88,89]. This is of crucial importance to the reduction of the switching current and power consumption of the current spin-transfer torque (STT) devices. Remarkably, perpendicular magnetic anisotropy

(PMA) has recently been reported in the CoFeAl-based epitaxial stacking structures [90-93], suggesting the feasibility of the application of CoFeAl in the perpendicular ferromagnetic electrodes of MTJs with high thermal stability at reduced dimension.

Other than the well-known cubic full Heusler compounds, a family of tetragonally distorted Heusler compounds Mn2YZ have recently emerged as another category of suitable materials due to their almost excellent fulfillment of the requirements for the electrodes of STT devices [94-99].

II.7.2 Heusler alloys in the field of thermoelectrics

The most commonly used thermoelectric materials are based on Bi_2Te_3 and Bi_2Se_3, which are considered as good thermoelectric materials at room temperature with a temperature independent figure of merit between 0.8 and 1.0 [100], and therefore they are suitable for refrigerating applications around 300K. Nevertheless, the use of telluride compounds is limited by the toxicity and rarity of Tellurium [101]. Motivated by the discovery of Bi_2Te_3 in mid-1950s, many thermoelectric materials were synthesized, but *ZT* did not exceed unity for 30 years or more.

The efficient thermoelectric performance of Heusler alloys have revolutionized the fields of waste heat recovery systems and power generators [102]. Half-Heusler (HH) alloys have a great potential for high-temperature power generation applications and are also environmentally friendly [103]. Examples of these alloys include NbFeSb, NbCoSn and VFeSb. They have a cubic MgAgAs-type structure formed by three interpenetrating fcc lattices. The ability to substitute any of these three sublattices opens the door for wide variety of compounds to be synthesized. Various atomic substitutions are employed to reduce the thermal conductivity and enhance the electrical conductivity. Previously, ZT could not peak more than 0.5 for p-type (0.8 for n-type) HH compounds. However, in the past few years, researchers were able to achieve $ZT \approx 1$ for both n- and p-type HH alloys [104].

II.8 Bibliography

1. F. Heusler, "Über magnetische Manganlegierungen", Verhandlungen der Deutschen Physikalischen Gesellschaft. 12, 219 (1903).
2. M. Bouchard, "Electron metallography and magnetic properties Cu-Mn-Al heusler compounds", Imperial College London, (1970).
3. M. Meinert, J M Schmalhorst, and G Reiss. Appl. Phys. Lett., 97:12501, 2010.
4. S. Chadov, X. Qi, J. Kübler, G. H. Fecher, C. Felser, and S. C. Zhang, Nature materials 9, 541 (2010).
5. J. Li, H. Chen, Y. Li, Y. Xiao, Z. Li, J. Appl. Phys. 105, 083717 (2009).
6. E. Bayar, N. Kervan, S. Kervan, J. Magn. Magn. Mater. 323, 2945 (2011).
7. B. Xu, M. Zhang, H. Yan, Phys. St. Sol. (b) 248, 2870 (2011).
8. M. Pugaczowa-Michalska, Intermetallics 24, 128 (2012).
9. M. Meinert, J.-M. Schmalhorst, C. Klewe, G. Reiss, E. Arenholz, Phys. Rev. B 84, 132405 (2011).
10. P. Klaer, C.A. Jenkins, V. Alijani, J. Winterlik, B. Balke, C. Felser, H.J. Elmers, Appl. Phys. Lett. 98, 212510 (2011).
11. S. Skaftouros, K. Özdoğan, E. Şaşıoğlu, I. Galanakis, Phys. Rev. B 87, 024420 (2013).
12. K. Özdoğan, E. Şaşıoğlu, I. Galanakis, J. Appl. Phys. 113, 193903 (2013).
13. K. Watanabe, Trans. Jpn. Inst. Met. 17, 220 (1976).
14. R.A. de Groot, F.M. Mueller, P.G. van Engen, K.H.J. Buschow. Phys. Rev. Lett. 50, 2024 (1983).
15. Webster PJ, Ziebeck KRA. Landolt-Börnstein - group III condensed matter, vol. 19C. Berlin: Springer; 1988. 75-184.
16. H. Luo, L. Yang, B. Liu, F. Meng, and E. Liu, Physica B: Condensed Matter 476, 110 (2015).
17. K. Özdoğan, I. Galanakis, J. Magn. Magn. Mater. 321, L34 (2009).
18. D. Xu, G. Liu, G.H. Fecher, C. Felser, Y. Li, H. Liu, J. Appl. Phys. 105, 07E901 (2009).
19. V. Alijani, J.Winterlik, G.H. Fecher, S.S. Naghavi, C. Felser, Phys. Rev. B 83, 184428 (2011).
20. Larson P, Mahanti S D, and Kanatzidis M G 2000 Phys. Rev. B 62 12754.
21. K. Özdoğan, I. Galanakis, J. Appl. Phys. 110, 076101 (2011).
22. I. Galanakis, E. ¸ E. Şaşıoğlu, K. Özdoğan, S. Blügel, Phys. Rev. B 90, 064408 (2014).

23. Skovsen I, Bjerg L, Christensen M, Nishibori E, Balke B, Felser C, et al. Dalton Trans 2010;39:10154-9.
24. Bacon GE, Plant JS. J Phys F Met Phys 1971;1:524-32.
25. Miura Y, Nagao K, Shirai M. Phys Rev B 2004;69:144413.
26. Picozzi S, Continenza A, Freeman AJ. Phys Rev B 2004;69:094423.
27. Webster PJ. Contemp Phys 1969;10:559-77.
28. Ziebeck RA, Neumann K-U. Landolt-Börnstein e group III condensed matter, vol. 32C. Berlin: Springer; 2001. pp. 64-314.
29. Graf T, Casper F, Winterlik J, Balke B, Fecher GH, Felser C. Z Anorg Allg Chem 2009;635:976.
30. J. Tobola, J. Pierre, J. Alloys Compd. 296, 243 (2000).
31. J. Tobola, S. Kaprzyk, P. Pecheur, Phys. St. Sol. (b) 236, 531 (2003).
32. M. Gillessen, R. Dronskowski, J. Comput. Chem. 30, 1290 (2009).
33. M. Gillessen, R. Dronskowski, J. Comput. Chem. 31, 612 (2010).
34. X. Li, "SPICA: stereographic projection for interactive crystallographic analysis", Journal of Applied Crystallography 49, 1818-1826 (2016).
35. Şaşıoğlu E, Sandratskii L M, and Bruno P 2005 J. Phys.: Condens. Matter 17 995; Weht R and Pickett W E 1999 Phys. Rev. B 60 13006.
36. Felser C, Fecher GH, Balke B. Angew Chem Int Ed 2007;46:668e99.
37. G H Fecher, H C Kandpal, S Wurmel, C Felser, and G Schönhense. J.Appl.Phys, 99:08J106, 2006.
38. J Kübler. Theory of Itinerant Electron Magnetism. Clarendon Press, Oxford, 2000.
39. Galanakis I, Dederichs P. Half metallic alloys (lecture notes in physics), vol. 676. Berlin: Springer Verlag; 2005.
40. V. L. Moruzzi, J. F. Janak, and K. Schwarz, Phys. Rev. B 37, 790 (1988).
41. M. Born and K. Huang, Dynamical Theory of Crystal Lattices (Oxford University Press, Oxford, Uk, 1954).
42. Reuss A. Calculation of the flow limits of mixed crystals on the basis of the plasticity of monocrystals. Z Angew Math Mech 1929;9:49–58.
43. Voigt W. Lehrbuch der kristallphysik (mit ausschluss der kristalloptik). Springer-Verlag; 2014.
44. D. Nguyen-Manh, M. Mrovec, and S. P. Fitzgerald, Mater. Trans. 49, 2497 (2008).

45. S.F. Pugh, XCII. Relations between the elastic moduli and the plastic properties of polycrystalline pure metals, London, Edinburgh, Dublin Philos. Mag. J. Sci. 45 (1954) 823–843.
46. V.V. Bannikov, I.R. Shein, A.L. Ivanovskii, Physica Status Solidi b 1 (2007) 89–91.
47. I.N. Frantsevich, F.F. Voronov, S.A. Bokuta, Elastic Constants and Elastic Moduli of Metals and Insulators Handbook, in: I.N. Frantsevich (Ed.), Naukova Dumka, Kiev, 1982, pp. 60–180.
48. Greaves, G.N., Greer, A.L., Lakes, R.S., Rouxel, T.: Poisson's ratio and modern materials. Nat. Mater. 10(11), 823–837 (2011).
49. Frantsevich, I., Voronov, F., Bokuta, S., Frantsevich, I.: Elastic Constants and Elastic Moduli of Metals and Insulators Handbook, pp. 60–180. Naukova Dumka, Kiev (1983).
50. D.H. Chung, W.R. Buessem, J. Appl. Phys. 38, 2010 (1967).
51. J. Wang, S. Yip, S.R. Phillpot, D. Wolf, Phys. Rev. Lett. 71, 4182 (1993).
52. M. E. Fine, L. D. Brown, and H. L. Marcus, Scr. Metall. 18, 951 (1984).
53. Britannica, The Editors of Encyclopaedia. "Thomas Johann Seebeck". *Encyclopedia Britannica*, 5 Apr. 2021.
54. Chasmar, R.P.; Stratton, R. The Thermoelectric figure of merit and its relation to thermoelectric generatorsy. J. Electron. Control 1959, 7, 52–72.
55. H.J. Xiang, D.J. Singh, Phys. Rev. B 76 (2007) 195111.
56. A.S. Botana, P.M. Botta, C. de la Calle, A. Piñeiro, V. Pardo, D. Baldomir, J.A. Alonso, Phys. Rev. B 83 (2011) 184420.
57. J.W.F. Dorleijn, Philips Res. Rep. 31 (1976) 287.
58. G. A. Slack, "The thermal conductivity of nonmetallic crystals," in Solid State Physics, pp. 1–71, Elsevier, 1979.
59. Rowe DM, editor. Thermoelectrics Handbook: Macro to Nano. Boca Raton, FL: CRC Press; 2005. p. 1022.
60. Uher C. Materials Aspect of Thermoelectricity. Boca Raton, FL: CRC Press; 2016. p. 610.
61. Kurosaki K, Takagiwa Y, Shi X, editors. Thermoelectric Materials: Principles and Concepts for Enhanced Properties. Berlin: De Gruyter; 2020. p. 280.
62. T. Graf, C. Felser, and S. S. P. Parkin, Prog. Solid State Chem. 39, 1 (2011).
63. F. Casper, T. Graf, S. Chadov, B. Balke, and C. Felser, Semicond. Sci. Technol. 27, 063001 (2012).

64. C. Felser and G. H. Fecher, Spintroincs: From Materials to Devices (Springer, Netherlands, 2013).
65. R. Kainuma et al., Nature 439, 957 (2006).
66. R. Kainuma, K. Oikawa, W. Ito, Y. Sutou, T. Kanomata, and K. Ishida, J. Mater. Chem. 18, 1837 (2008).
67. J. Barth, G. H. Fecher, B. Balke, T. Graf, C. Felser, A. Shkabko, and A. Weidenkaff, Phys. Rev. B 81, 064404 (2010).
68. S. Bhattacharya, A. L. Pope, R. T. Littleton IV, and T. M. Tritt, V. Ponnambalam, Y. Xia, and S. J. Poon, Appl. Phys. Lett. 77, 2476 (2000).
69. X. L. Qi, R. Li, J. Zang, and S. C. Zhang, Science 323, 1184 (2009).
70. H. Lin, L. A. Wray, Y. Q. Xia, S. Y. Xu, S. Jia, R. J. Cava, A. Bansil, and M. Z. Hasan, Nat. Mater. 9, 546 (2010).
71. M. N. Baibich, J. M. Broto, A. Fert, F. Nguyen van Dau, F. Petroff, P. Eitenne, G. Creuzet, A. Friederich, and J. Chazelas, Phys. Rev. Lett. 61, 2472 (1988).
72. G. Binasch, P. Gr€unberg, F. Saurenbach, and W. Zinn, Phys. Rev. B 39, 4828 (1989).
73. K. E. H. M. Hanssen and P. E. Mijnarends, Phys. Rev. B 34, 5009 (1986).
74. C. T. Tanaka, J. Nowak and J. S. Moodera, J. Appl. Phys. 86, 6239 (1999).
75. S. J. Jenkins, Phys. Rev. B 70, 245401 (2004).
76. M. C. Kautzky, F. B. Mancoff, J. F. Bobo, P. R. Johnson, R. L. White and B. M. Clemens, J. Appl. Phys. 81, 4026 (1997).
77. P. R. Johnson, M. C. Kautzky, F. B. Mancoff, R. Kondo, B. M. Clemens and R. L. White, IEEE Trans. Magn. 32, 4615 (1996).
78. J. Kübler, A. R. William and C. B. Sommers, Phys. Rev. B 28, 1745 (1983).
79. S. Ishida, S. Fujii, S. Kashiwagi and S. Asano, J. Phys. Soc. Jpn. 64, 2152 (1995).
80. W. E. Pickett and J. S. Moodera, Phys. Today 54, 39 (2001).
81. I. Galanakis, P. H. Dederichs and N. Papanikolaou, Phys. Rev. B 66, 174429 (2002).
82. S. Picozzi, A. Continenza and A. J. Freeman, Phys. Rev. B 66, 094421 (2002).
83. N. Auth, G. Jakob, T. Block and C. Felser, Phys. Rev. B 68, 024403 (2003).
84. C. Felser, B. Heitkamp, F. Kronast, D. Schmitz, S. Cramm, H. A. Durr, H. J. Elmers, G. H. Fecher, S. Wurmehl, T. Block, D. Valdaitsev, S. A. Nepijko, A. Gloskovskii, G. Jakob, G. Schonhense and W. Eberhardt, J. Phys.: Condens. Matter 15, 7019 (2003).
85. K. Inomata, S. Okamura, R. Goto and N. Tezuka, Jpn. J. Appl. Phys. 42, L419 (2003).
86. K. Inomata, N. Ikeda, N. Tezuka, R. Goto, S. Sugimoto, M. Wojcik and E. Jedryka, Sci. Tech. Adv. Mater. 9, 014101 (2008).

87. T. M. Nakatani, N. Hase, H. S. Goripati, Y. K. Takahashi, T. Furubayashi and K. Hono, IEEE Trans. Magn. 48, 1751 (2012).
88. S. Mizukami, D. Watanabe, M. Oogane, Y. Ando, Y. Miura, M. Shirai and T. Miyazaki, J. Appl. Phys. 105, 07D306 (2009).
89. M. Oogane, T. Kubota, Y. Kota, S. Mizukami, H. Naganuma, A. Sakuma and Y. Ando, Appl. Phys. Lett. 96, 252501 (2010).
90. X. Q. Li, X. G. Xu, D. L. Zhang, J. Miao, Q. Zhan, M. B. A. Jalil, G. H. Yu and Y. Jiang, Appl. Phys. Lett. 96, 142505 (2010).
91. W. H. Wang, H. Sukegawa and K. Inomata, Appl. Phys. Exp. 3, 093002 (2010).
92. X. Q. Li, S. Q. Yin, Y. P. Liu, D. L. Zhang, X. G. Xu, J. Miao and Y. Jiang, Appl. Phys. Exp. 4, 043006 (2011).
93. Z. C. Wen, H. Sukegawa, S. Mitani and K. Inomata, Appl. Phys. Lett. 98, 192505 (2011).
94. B. Balke, G. H. Fecher, J. Winterlik and C. Felser, Appl. Phys. Lett. 90, 152504 (2007).
95. J. Winterlik, B. Balke, G. H. Fecher, C. Felser, M. C. M. Alves, F. Bernardi and J. Morais, Phys. Rev. B 77, 054406 (2008).
96. F. Wu, S. Mizukami, D. Watanabe, H. Naganuma, M. Oogane, Y. Ando and T. Miyazaki, Appl. Phys. Lett. 94, 122503 (2009).
97. F. Wu, S. Mizukami, D. Watanabe, E. P. Sajitha, H. Naganuma, M. Oogane, Y. Ando and T. Miyazaki, IEEE Trans. Magn. 46, 1863 (2010).
98. T. Kubota, Y. Miura, D. Watanabe, S. Mizukami, F. Wu, H. Naganuma, X. M. Zhang, M. Oogane, M. Shirai, Y. Ando and T. Miyazaki, Appl. Phys. Exp. 4, 043002 (2011).
99. H. Kurt, K. Rode, M. Venkatesan, P. Stamenov and J. M. D. Coey, Phys. Rev. B 83, 020405 (2011).
100. *Duck Young Chung; Hogan, T.; Schindler, J.; Iordarridis, L.; Brazis, P.; Kannewurf, C.R.; Baoxing Chen; Uher, C.; Kanatzidis, M.G. (1997). "Complex bismuth chalcogenides as thermoelectrics". XVI ICT '97. Proceedings ICT'97. 16th International Conference on Thermoelectrics (Cat. No.97TH8291). p. 459.*
101. Cunha, Rodrigo L. O. R., Gouvea, Iuri E. and Juliano, LuizA glimpse on biological activities of tellurium compounds. Anais da Academia Brasileira de Ciências [online]. 2009, v. 81, n. 3 [Accessed 17 August 2021], pp. 393-407.
102. Singh S, Gupta DC. J Supercond Nov Magn 2018.
103. J.-W. G. Bos and R. A. Downie, Half-Heusler thermoelectrics: a complex class of materials, J. Phys.: Condens. Matter 26 (2014) 433201.

104. *Huang, Lihong; Zhang, Qinyong; Yuan, Bo; Lai, Xiang; Yan, Xiao; Ren, Zhifeng (2016). "Recent progress in half-Heusler thermoelectric materials". Materials Research Bulletin. 76: 107–112.*

Chapter III

Methodology

III.1 The many-body problem

One of the fundamental problems in condensed-matter physics and quantum chemistry is the theoretical study of electronic properties of systems ranging from atoms and molecules to complex materials. Since electrons are governed by the laws of quantum mechanics, all these systems are fully described by the Schrödinger equation. Analytic solutions of this equation are obtainable for very simple systems only. However, for systems with large number of atoms, the electrostatic repulsion between the electrons makes its numerical resolution very difficult. In that case, it is natural to consider the many-electron wave function $\varphi(\mathrm{r}_1, \mathrm{r}_2, .., \mathrm{r}_\mathrm{i}, ...)$ with appropriate approximations. The earliest and widely used approximation was that of Hartree [1], which expresses the wave function of a system as a product of one-electron wave functions, so that the problem reduces to a one-electron Schrödinger equation. Then, considerable improvement of the energy computation was made by incorporating the exchange effects with the so-called Hartree-Fock approximation [2], which replaces the product of one-electron wave functions by a linear combination of orbitals [3].

When the adiabatic approximation is made, that permits to separate the movements of ions and electrons, the electronic Schrödinger equation describing the state of the electrons interacting in the presence of ions, reads:

$$\sum_i\left(\frac{-\hbar^2}{2m}\nabla_i^2\right) + \frac{1}{2}\sum_i\sum_{j\neq i}\mathbf{U_{ee}}\left(\left|\mathbf{r_i}-\mathbf{r_j}\right|\right) + \sum_i\sum_\alpha\mathbf{U_{ei}}\left(\left|\mathbf{R_\alpha}-\mathbf{r_i}\right|\right)\boldsymbol{\varphi}_\mathbf{el} = \mathbf{E_{el}}\boldsymbol{\varphi}_\mathbf{el} \qquad \text{(III-1)}$$

Or under the compact form:

$$[\mathbf{T}+\mathbf{U_{ee}}+\mathbf{U_{ei}}]\boldsymbol{\varphi}_\mathbf{el} = \mathbf{E_{el}}\boldsymbol{\varphi}_\mathbf{el} \qquad \text{(III-2)}$$

where the first two terms in the Hamiltonian are the kinetic and electron-electron interaction operators, respectively, and the third term represents the potential energy operator of the electron i in the field of all ions. Within the Hartree approximation, the N-electron wave function φ_{el} is the product of one-electron wave functions:

$$\boldsymbol{\varphi}_\mathbf{el} = (\mathbf{r_1}, \mathbf{r_2}, .., \mathbf{r_N}) = \prod_i\boldsymbol{\varphi}_\mathbf{i}(\mathbf{r_i}) = \boldsymbol{\varphi_1}(\mathbf{r_1})\boldsymbol{\varphi_2}(\mathbf{r_2})\ldots\boldsymbol{\varphi_N}(\mathbf{r_N}) \qquad \text{(III-3)}$$

Consequently, the electronic energy E_{el}; as a sum of one-electron energies, is given by:

$$\mathbf{E_{el}} = \sum_{i} \mathbf{E_i} = \langle \boldsymbol{\varphi}_{\mathbf{el}} | \mathbf{H} | \boldsymbol{\varphi}_{\mathbf{el}} \rangle$$

$$= \int \dots \int \boldsymbol{\varphi}_{\mathbf{1}}^{*}(\mathbf{r_1}) \dots \boldsymbol{\varphi}_{N}^{*}(\mathbf{r_N})[\mathbf{T} + \mathbf{U_{ei}}]\boldsymbol{\varphi}_{\mathbf{1}}(\mathbf{r_1}) \dots \boldsymbol{\varphi}_{\mathbf{N}}(\mathbf{r_N}) d\mathbf{r_1} \dots d\mathbf{r_N}$$

$$+ \frac{\mathbf{1}}{\mathbf{2}} \sum_{i} \sum_{j \neq i} \int \dots \int \boldsymbol{\varphi}_{i}^{*}(\mathbf{r_i}) \boldsymbol{\varphi}_{j}^{*}(\mathbf{r_j}) [\frac{\mathbf{e^2}}{\mathbf{4\pi\varepsilon_0 r_{ij}}}] \boldsymbol{\varphi}_{\mathbf{i}}(\mathbf{r_i}) \boldsymbol{\varphi}_{\mathbf{j}}(\mathbf{r_j}) d\mathbf{r_i} d\mathbf{r_j} \qquad \text{(III-4)}$$

The last term in the previous equation is the so-called Coulomb energy. The simplification achieved in this term comes from the fact that certain factors are equal to unity as a consequence of normalization of the wave function. Now, the implementation of the Hartree approximation amounts to define the Hartree potential $W^{H}(r_i)$ representing the potential energy of the electron i in the field of all other electrons:

$$\mathbf{W^H(r_i)} = \sum_{\mathbf{j \neq i}} \int \frac{\mathbf{e^2}}{\mathbf{4\pi\varepsilon_0}} \frac{|\boldsymbol{\varphi}_{\mathbf{j}}(\mathbf{r_j})|^2}{\mathbf{r_{ij}}} \mathbf{dr_j}, \qquad \text{(III-5)}$$

in order to reduce the Schrödinger equation for multiple electrons (equation (III-1)) to the sum of one-electron Schrödinger equations:

$$[\frac{-\hbar^2}{2m} \boldsymbol{\nabla}_{\boldsymbol{i}}^{\mathbf{2}} + \sum_{\alpha} \mathbf{U_{ei}}(|\mathbf{R_\alpha} - \mathbf{r_i}|) + \mathbf{W^H(r_i)}] \boldsymbol{\varphi}_{\mathbf{i}} = \mathbf{E_i} \boldsymbol{\varphi}_{\mathbf{i}} \qquad \text{(III-6)}$$

Besides, a different description of many-electron systems was made by Thomas [4] and Fermi [5], who noted that the energy of electrons moving in the potential of nuclei can be directly calculated from the electron density n(r) rather than from the wave function. If N is the number of electrons in the system, the electron density is defined as:

$$\boldsymbol{n(r)} = \boldsymbol{N} \int \dots \int \boldsymbol{\varphi}_{\boldsymbol{el}}^{*}(\mathbf{r}, \mathbf{r_2}, .., \mathbf{r_N}) \, \boldsymbol{\varphi}_{\mathbf{el}}(\mathbf{r}, \mathbf{r_2}, .., \mathbf{r_N}) d\mathbf{r_2} d\mathbf{r_N}, \qquad \text{(III-7)}$$

which is normalized to the electron number, $\int n(r)dr = N$. The term $n(r)dr$ represents the elemental probability of finding any electron in the volume element dr at position r: As a result, the electronic energy E_{el} may be calculated in terms of the electron density as:

$$\mathbf{E_{el}[n]} = \langle \boldsymbol{\varphi}_{\mathbf{el}} | \mathbf{H} | \boldsymbol{\varphi}_{\mathbf{el}} \rangle = \int [\mathbf{T} + \mathbf{U_{ee}} + \mathbf{U_{ei}}] \mathbf{n(r)} \mathbf{dr} \qquad \text{(III-8)}$$

III.2 The Density Functional Theory

The density functional theory (DFT) established itself as a well-reputed way to compute the electronic structure in most branches of chemistry and materials science. The DFT is applied, with low computational cost and reasonable accuracy, to predict diverse properties as binding or atomization energies, shapes and sizes of molecules, crystal structures of solids, energy barriers to various processes, etc. In the mid-1980s, it became an attractive alternative to the well-developed wave function techniques such as Hartree-Fock, when crucial developments in exchange-correlation energy has been taken into account, since the Hartree-Fock method treats exchange exactly but neglects correlation.

The rigorous developments of the density functional theory were posed by Hohenberg, Kohn and Sham [6,7], that legitimized the model intuitively established by Thomas, Fermi and Dirac [8]. For practical reasons, they replaced the potential energy operator of the electron i in the field of all ions U_{ei} with the external potential V_{ext} to indicate that the electrons move in an arbitrary external potential including the Coulomb energy due to point nuclei, so that the Schrödinger equation for N electrons (equation (III-2)), reads:

$$[\mathbf{T} + \mathbf{U_{ee}} + \mathbf{V_{ext}}]\boldsymbol{\varphi}_{\mathbf{el}} = \mathbf{U_{el}}\boldsymbol{\varphi}_{\mathbf{el}}, \quad \text{(III-9)}$$

and the electronic energy (equation (III-8)), is a functional of the electron density profile n(r):

$$\mathbf{E_{el}}[\mathbf{n}] = \langle \boldsymbol{\varphi}_{\mathbf{el}} | \mathbf{H} | \boldsymbol{\varphi}_{\mathbf{el}} \rangle = \mathbf{F}[\mathbf{n}] + \int \mathbf{V_{ext}}(\mathbf{r})\mathbf{n}(\mathbf{r})\, \mathbf{dr}, \quad \text{(III-10)}$$

where

$$\mathbf{F}[\mathbf{n}] = \langle \boldsymbol{\varphi}_{\mathbf{el}} | \mathbf{T} | \boldsymbol{\varphi}_{\mathbf{el}} \rangle + \langle \boldsymbol{\varphi}_{\mathbf{el}} | \mathbf{U_{ee}} | \boldsymbol{\varphi}_{\mathbf{el}} \rangle = \mathbf{T}[\mathbf{n}] + \mathbf{U_{ee}}[\mathbf{n}], \quad \text{(III-11)}$$

is the so-called universal energy functional, in the sense that it does not contain the external potential $V_{ext}(r)$ and can be determined independently of $\int V_{ext}(r)n(r)\,dr$.

III.2.1 Formulation of Hohenberg and Kohn

The Hohenberg and Kohn (HK) approach might be understood by considering the ground state [9] of a system of electrons at 0K with the wave function $\varphi^{(1)}$, the Hamiltonian $H^{(1)}$ and the external potential $V_{ext}^{(1)}(r)$. The HK approach asserts that the external potential can be uniquely determined by an electron density, n(r), that minimizes the ground state energy:

$$\mathbf{E^{(1)} = \langle \varphi^{(1)} | H^{(1)} | \varphi^{(1)} \rangle = T[n] + U_{ee}[n] + \int V_{ext}^{(1)}(r) n(r)\, dr}, \quad \text{(III-12)}$$

by supposing that another Hamiltonian $H^{(2)}$, only different from $H^{(1)}$ in the external potential $V_{ext}^{(2)}(r) \neq V_{ext}^{(1)}(r)$ gives rise to the wave function $\varphi^{(1)}$ that yields the same density $n(r)$. Unless $V_{ext}^{(1)}(r) - V_{ext}^{(2)}(r) = \text{const}$, $\varphi^{(2)}$ cannot be equal to $\varphi^{(1)}$ since they satisfy different Schrödinger equations. The wave function $\varphi^{(2)}$ minimizes the ground state energy for the Hamiltonian $H^{(2)}$:

$$\mathbf{E^{(2)} = \langle \varphi^{(2)} | H^{(2)} | \varphi^{(2)} \rangle}, \quad \text{(III-13)}$$

By force of the variational principle, the expectation energy of the Hamiltonian is the lowest with its "correct" wave function, hence

$$\mathbf{E^{(1)} = \langle \varphi^{(1)} | H^{(1)} | \varphi^{(1)} \rangle < \langle \varphi^{(2)} | H^{(1)} | \varphi^{(2)} \rangle} \quad \text{(III-14)}$$

The operators T and U_{ee} being the same in the two Hamiltonians, it follows that the equation (III-14) becomes:

$$\mathbf{E^{(1)} < E^{(2)} + \int [V_{ext}^{(1)}(r) - V_{ext}^{(2)}(r)] n(r)\, dr} \quad \text{(III-15)}$$

The same reason applied to (III-13) leads to:

$$\mathbf{E^{(2)} < E^{(1)} + \int [V_{ext}^{(2)}(r) - V_{ext}^{(1)}(r)] n(r)\, dr}, \quad \text{(III-16)}$$

and the sum of the two previous relations leads to the inconsistency:

$$\mathbf{E^{(1)} + E^{(2)} < E^{(1)} + E^{(2)}}, \quad \text{(III-17)}$$

indicating that the starting hypothesis is wrong. Thus the HK approach, based upon the variational principle, implies that it is sufficient to use the electron density (and not the full wave function) as the variational property, from which, once it is found, all ground-state properties can be deduced. The considerations above are restricted to non-degenerate ground states; however, a generalization towards degenerate states has been suggested [10], within a different and more systematic scheme.

While the universal energy functional $F[n]$ (composed of kinetic and potential energies of the electron gas), remains unchanged whatever the external potential $V_{ext}(r)$ (equation (III-11)), two different external potentials cannot yield the same ground state energy. The HK approach asserts that there is a one-to-one mapping between external potential $V_{ext}(r)$, electron density $n(r)$ and wave function of the system in its ground state. It implies that, given the electron density, only a unique external potential and, consequently, its unique wave function, can be determined. Conversely, given the external potential, the corresponding electron density and wave function are uniquely defined. It should also be stressed that the term $\int V_{ext}(r) n(r)\, dr$ is relatively easy to calculate for a given external potential, whereas the expressions of the functionals $T[n]$ and $U_{ee}[n]$ are more difficult to evaluate and some approximations have to be

made. In the initial density functional theory, the main difficulty was to determine the functionals of the kinetic and potential energies for the interacting electron gas.

III.2.2 Formulation of Kohn and Sham

The Kohn and Sham (KS) approach consists in prescribing a convenient recipe to calculate the universal energy functional $\mathbf{F}[\mathbf{n}] = \mathbf{T}[\mathbf{n}] + \mathrm{U}_{\mathbf{ee}}[\mathbf{n}]$ for interacting electronic systems.

The authors assumed that it was reasonable to evaluate the kinetic energy $\mathbf{T}[\mathbf{n}]$ of any interacting electronic system by $\mathbf{T_o}[\mathbf{n}]$, which is the kinetic energy of the corresponding non homogeneous and non-interacting electron gas of the same density, plus the exchange correlation energy $\mathbf{E_{xc}}[\mathbf{n}]$, to be further specified see equation (III-19).

The potential energy $\mathbf{U_{ee}}[\mathbf{n}]$, which, within the Hartree approximation, is that of electrons in the field of all other electrons (equation (III-5)), is approximated by the electron density interacting with itself, including self-interaction:

$$\mathbf{U_{ee}}[\mathbf{n}] \sim \mathbf{W^H}[\mathbf{n}] = \frac{\mathbf{1}}{\mathbf{2}} \frac{\mathbf{e^2}}{\mathbf{4\pi\varepsilon_0}} \iint \frac{\mathbf{n(r)n(r')}}{\mathbf{|r-r'|}} \mathbf{dr\, dr'} \qquad \text{(III-18)}$$

With the KS prescription, the total energy functional (equation (III-10)) reads:

$$\mathbf{E_{el}}[\mathbf{n}] = \mathbf{T_o}[\mathbf{n}] + \mathbf{E_{xc}}[\mathbf{n}] + \mathbf{W^H}[\mathbf{n}] + \int \mathbf{V_{ext}}(\mathbf{r})\mathbf{n}(\mathbf{r})\, \mathbf{dr} \qquad \text{(III-19)}$$

In the KS approach, the kinetic energy $\mathbf{T_o}[\mathbf{n}]$ is not an explicit functional of density, but of orbitals of which this density is constructed. The exchange-correlation energy functional $\mathbf{E_{xc}}[\mathbf{n}]$ incorporates the difference between real and approximated universal energy functionals:

$$\mathbf{E_{xc}}[\mathbf{n}] = (\mathbf{T}[\mathbf{n}] + \mathbf{U_{ee}}[\mathbf{n}]) - (\mathbf{T_0}[\mathbf{n}] + \mathbf{W^H}[\mathbf{n}]) \qquad \text{(III-20)}$$

It should be noted that $\mathbf{E_{xc}}[\mathbf{n}]$ is the only unknown functional in the right-hand side of equation (III-19), since the other terms can be calculated exactly.

In practical terms, $\mathbf{E_{xc}}[\mathbf{n}]$ is a small part of the total energy because the magnitudes of $\mathbf{T}[\mathbf{n}]$ and $\mathbf{T_0}[\mathbf{n}]$ are similar, and the same is true of $\mathbf{U_{ee}}[\mathbf{n}]$ and $\mathbf{W^H}[\mathbf{n}]$. Note also that, if $\mathbf{E_{xc}}[\mathbf{n}]$ vanishes, the physical content of the KS procedure becomes identical to that of the Hartree approximation given by equation (III-4).

The simplest and reasonable approximation for $\mathbf{E_{xc}[n]}$ proposed by Kohn and Sham is the so-called local density approximation (LDA):

$$\mathbf{E_{xc}^{LDA}[n(r)] = \int e_{xc}\,[n(r)]n(r)dr} \qquad \text{(III-21)}$$

where $\int \mathbf{e_{xc}}\,[\mathbf{n(r)}]$ is the exchange-correlation energy, per electron, of the uniform electron gas of local electron density $\mathbf{n(r)}$.

A fairly good result for $\mathbf{E_{xc}^{LDA}[n(r)]}$ cannot be overstated when n(r) has a very low spatial variation. Considering the characteristics of the functionals in equation (III-19), it is not surprising that the many-electron Schrödinger equation in the KS procedure reduces to a set of one-electron equations. Indeed, the electron density would minimize the total energy, i.e. $\mathbf{\delta E_{el}[n] = 0}$, under the normalization condition $\int \mathbf{n(r)dr = 0}$.

Therefore, the method of Lagrange with the multiplier μ may be used to obtain the equation requiring that the variation of the functional $\{\mathbf{E_{el}[n]} - \mu\mathbf{N}\}$ with respect to $\mathbf{n(r)}$ is equal to zero, i.e., $\mathbf{\delta\{E_{el}[n] - \mu N\} = 0}$.

This variation allows us to define the functional derivative, denoted by $\frac{\mathbf{\delta}}{\mathbf{\delta n(r)}}\{\mathbf{E_{el}[n]} - \mu\mathbf{N}\}$, by the relation:

$$\mathbf{\delta\{E_{el}[n] - \mu N\} = \frac{\delta}{\delta n(r)}\{E_{el}[n] - \mu N\}\delta n(r)dr} \qquad \text{(III-22)}$$

where, according to equations (III-18, -19 and -21), the functional $\{\mathbf{E_{el}[n]} - \mu\mathbf{N}\}$ reads:

$$\{\boldsymbol{T_0[n]} + \frac{1}{2}\frac{e^2}{4\pi\varepsilon_0}\int\int\frac{n(r)n(r')}{|r-r'|}\boldsymbol{drdr'} + \int \boldsymbol{e_{xc}[n]n(r)dr} + \int \boldsymbol{V_{ext}(r)n(r)dr} - \mu\int \boldsymbol{n(r)dr}\}$$

Now, with equation (III-22), the variational principle $\mathbf{\delta\{E_{el}[n] - \mu N\} = 0}$ yields:

$$\int\left\{\frac{\delta}{\delta n}(\boldsymbol{T_0[n]}\right) + \frac{e^2}{4\pi\varepsilon_0}\int\frac{n(r')}{|r-r'|}\boldsymbol{dr'} + \boldsymbol{e_{xc}[n]} + \boldsymbol{n(r)}\frac{\delta}{\delta n}(\boldsymbol{e_{xc}[n]}) + \boldsymbol{V_{ext}(r)} - \mu\}\boldsymbol{\delta n(r)dr} = \mathbf{0} \qquad \text{(III-23)}$$

Kohn and Sham postulated that the many-electron system described by the functional derivative in brackets of the previous equation could be equivalently represented by a non-interacting reference system described by the following one-electron Schrödinger equation:

$$\left(\frac{-\hbar^2}{2m}\boldsymbol{\nabla_i^2} + \boldsymbol{v_{KS}}\right)\boldsymbol{\varphi_i} = \boldsymbol{E_i\varphi_i}, \qquad \text{(III-24)}$$

where each electron moves independently in the effective potential $\boldsymbol{v_{KS}(r)}$ consisting of the Hartree potential $\boldsymbol{W^H(r)}$, the exchange-correlation potential $\boldsymbol{V_{xc}(r)}$ and the external potential $\boldsymbol{V_{ext}(r)}$; namely:

$$\boldsymbol{v_{KS}(r) = W^H(r) + v_{xc}(r) + V_{ext}(r)} \quad \text{(III-25)}$$

By setting: $\frac{-\hbar^2}{2m}\boldsymbol{\nabla_i^2} = \frac{\delta}{\delta n}\{\boldsymbol{T_0[n(r)]}\}$,

$$\boldsymbol{W^H(r)} = \frac{e^2}{4\pi\varepsilon_0}\int \frac{n(r')}{|r-r'|}\boldsymbol{dr'}, \quad \text{(III-26)}$$

$$\boldsymbol{v_{xc}(r) = e_{xc}[n] + n(r)\frac{\delta}{\delta n}(e_{xc}[n])},$$

$$\boldsymbol{E_i} = \mu,$$

and $\boldsymbol{n(r)} = \sum_i |\boldsymbol{\varphi_i}|^2$ (III-27)

Thus, the electron density in atoms, molecules and solids can be regarded as a sum of densities due to non-interacting quasi-particles moving in the effective potential $\boldsymbol{v_{KS}(r)}$.

In the KS equation (III-24), the potential $\boldsymbol{v_{KS}(r)}$ is a function of the electron density **n(r)**, which can be calculated from the wave functions (equation (III-27)) of independent electrons (Kohn-Sham orbitals).

Provided that $\boldsymbol{e_{xc}n[(r)]}$ is known, the KS equation may be solved in a self-consistent procedure as follows: from an initial arbitrary electron density $\boldsymbol{n_1(r)}$; the effective potential $\boldsymbol{v_{KS}(r)}$ is determined and equation (III-24) is solved. Then, a new electron density $\boldsymbol{n_2(r)}$ is deduced with equation (III-27), and the procedure is repeated until convergence of the potential $\boldsymbol{v_{KS}(r)}$ and the electron density $\boldsymbol{n(r)}$.

It should be noted that the KS orbitals are calculated at each iteration, in terms of a set of basis functions, and that the coefficients of linear combination of basis functions are determined as in the Hartree-Fock calculations, but the computational time is shorter.

The choice of the set of basis functions is of great importance in the KS calculations.
The KS approach gives useful results for most physical and chemical applications [11], but a large number of subsequent approximations must be used for correcting some of the defects of the local density approximation $\boldsymbol{E_{xc}^{LDA}[n(r)]}$.

III.3 Generalized-gradient approximations

The development of the generalized gradient approximation (GGA) started in 1980, with the form,

$$\boldsymbol{E_{xc}^{GGA}[n] = \int f\,[n(r), \nabla n(r)]\,dr,} \qquad \text{(III-28)}$$

where f is some function. The GGAs are semi-local approximations in the sense that f does not only use the local value of the density $\boldsymbol{n(r)}$ but also its gradient $\boldsymbol{\nabla n(r)}$.

For simplicity, we consider here only the spin-independent form, but in practice, GGA functionals are more generally formulated in terms of spin densities ($\boldsymbol{n\uparrow, n\downarrow}$) and their gradients ($\boldsymbol{\nabla n\uparrow, \nabla n\downarrow}$).

Many GGA functionals have been proposed. We very briefly review here some of the most widely used ones.

III.3.1 B88 exchange functional

The Becke 88 (B88 or B) [12] exchange functional is formulated as an additive correction to LDA. It consists in a compact function of $\boldsymbol{n}$ and $\frac{\boldsymbol{|\nabla n|}}{\boldsymbol{n^{4/3}}}$ chosen so as to satisfy the exact asymptotic behavior of the exchange energy per particle for finite systems, and with an empirical parameter fitted to Hartree-Fock exchange energies of rare-gas atoms.

III.3.2 PBE exchange-correlation functional

The Perdew-Burke-Ernzerhof (PBE) [13] exchange-correlation functional is a simplification of the PW91 functional [14-16].

The exchange and correlation energies per particle are expressed as simpler functions of $\boldsymbol{n}$ and $\boldsymbol{|\nabla n|}$ enforcing less exact conditions and with no fitted parameters. Specifically, the function used for correlation enforces the second-order small-gradient expansion in the high-density limit, the vanishing of correlation in the large-gradient limit, and removes the logarithm divergence of the LDA in the high-density limit.

The function used for exchange is chosen to cancel out the second-order small-gradient expansion of correlation and enforces the Lieb-Oxford bound in the large-gradient limit.

III.4 Meta-generalized gradient approximations

The meta-generalized gradient approximations (meta-GGAs or mGGAs) are of the generic Form:

$$\boldsymbol{E_{xc}^{mGGA}[n] = \int f\,[n(r), \nabla n(r), \nabla^2 n(r), \tau(r)]\,dr} \quad \text{(III-29)}$$

i.e., they use more ingredients than the GGAs, namely the Laplacian of the density $\boldsymbol{\nabla^2 n(r)}$ and/or the non-interacting positive kinetic energy density $\boldsymbol{\tau(r)}$

$$\boldsymbol{\tau(r) = \frac{1}{2}\sum_{i=1}^{N} |\nabla \varphi_i(r)|^2}, \quad \text{(III-30)}$$

where $\boldsymbol{\varphi_i(r)}$ are the KS orbitals. Note that meta-GGAs are only implicit functionals of the density since $\boldsymbol{\tau(r)}$ is itself an implicit functional of the density through the orbitals.

To avoid complications for calculating the functional derivative, they are usually considered as functionals of $\boldsymbol{n}$ and $\boldsymbol{\tau}$ taken as independent variables, $\boldsymbol{E_{xc}^{mGGA}[n, \tau]}$. This tacitly implies a slight extension of the usual KS method.

The meta-GGAs are considered part of the family of semi-local approximations, in the sense that $\boldsymbol{\tau(r)}$ depends only the gradient of the orbitals at point r. Again, we consider here only the spin-independent form, but meta-GGAs are more generally formulated in terms of spin-resolved quantities ($\boldsymbol{n\uparrow, n\downarrow, \nabla n\uparrow, \nabla n\downarrow, \nabla^2 n\uparrow, \nabla^2 n\downarrow, \tau\uparrow, \tau\downarrow}$).

One motivation for the introduction of the variable $\boldsymbol{\tau(r)}$ is that it appears in the short-range expansion of the exchange hole [17], which for the case of a closed-shell system is:

$$\boldsymbol{n_x(r, r') = -\frac{n(r)}{2} - \frac{1}{3}\left[\nabla^2 n(r) - 4\tau(r) + \frac{|\nabla n(r)|^2}{2n(r)}\right]|r - r'|^2 + \cdots} \quad \text{(III-31)}$$

Another important motivation is that $\boldsymbol{\tau(r)}$ can be used to make the correlation energy per particle $\boldsymbol{\varepsilon_c(r)}$ correctly vanish in spatial regions where the density has a one-electron character.

This is done by comparing $\boldsymbol{\tau(r)}$ with the von Weizsäcker kinetic energy density,

$$\boldsymbol{\tau^W(r) = \frac{|\nabla n(r)|^2}{8n(r)}}, \quad \text{(III-32)}$$

which is exact for one-electron systems, e.g. by introducing the ratio $\boldsymbol{\frac{\tau(r)}{\tau^W(r)}}$.

One of the most used meta-GGA approximation is the Tao-Perdew-Staroverov-Scuseria (TPSS) [18] exchange-correlation functional. A more recently developed meta-GGA approximation is the SCAN exchange-correlation functional [19], which satisfies 17 known exact constraints and contains 7 parameters determined by fitting to a few simple systems.

III.5 Basis function

To solve Kohn-Sham equations numerically, besides the exchange correlation potential and full potential, we must employ a set of basis functions in order to efficiently represent the electronic wave function. The electronic structure calculations done by first principles methods are employed by expanding in basis sets of atomic orbitals.

III.5.1 Augmented Plane Wave method (APW)

The wave function of Bloch, vector k, and band number λ is a linear combination of basis functions satisfying the Bloch boundary conditions. In periodic systems, an electronic wave function $\boldsymbol{\varphi(r)}$ can be written as a plane wave (PW) [20]. Plane wave constitutes a complete and orthogonal basis set. Therefore, every electronic wave function can be written as,

$$\boldsymbol{\varphi_{K\lambda}(r) = \sum_G C_G^{k\lambda}\, e^{i(G+K)r}}, \qquad \text{(III-33)}$$

where, G are reciprocal lattice vectors, and $\boldsymbol{C_G}$ are variational coefficients. This works only for pseudo potentials and not for the potential with a singularity 1/r at the nucleus where strong fluctuations appear in the wave function close to the nucleus.

Slater [21] introduces non-overlapping muffin-tin spheres. For the special case of muffin-tin potential, the Bloch function may be determined with any desired accuracy without having a complete basis set.

In the APW scheme [22], the unit cell is partitioned into two types of regions: (i) spheres centered around all constituent atomic sites, the so called Muffin-Tin sphere (S), and (ii) the remaining part of the unit cell, which is called interstitial region (I) as shown in figure (III.1)

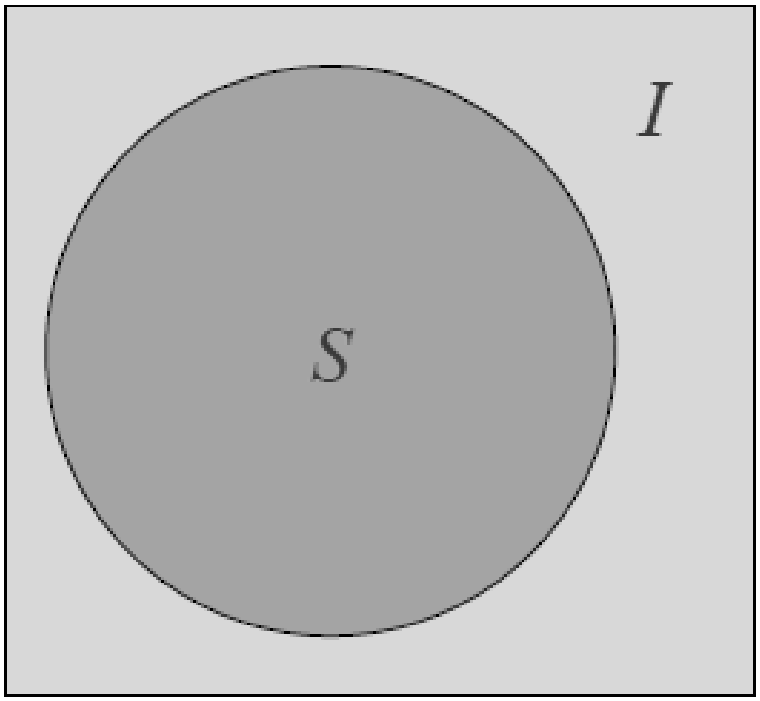

Figure III.1 Unit cell volume partitioned into the muffin-tin spheres (S) and the interstitial region (I).

The potential in the whole space can be defined as,

$$\boldsymbol{V(r)} = \begin{cases} \boldsymbol{constant} & \boldsymbol{r \in IR} \\ \boldsymbol{V(r)} & \boldsymbol{r \in MT} \end{cases} \quad \text{(III-34)}$$

Close to the nuclei, it is assumed that electrons behave like in a free-atom. The atomic like functions are efficient to describe the behavior of the electrons in this region. Therefore, the wave function of the electron over the whole unit cell can be obtained as:

$$\boldsymbol{\varphi_G^{APW}(k,r)} = \begin{cases} \mathbf{e^{i(G+K)r}} & \mathbf{r \in IR} \\ \mathbf{\sum_{lm} A_{lm}^{\mu G}\,(k) U_l\,(r,\epsilon) \gamma_{lm}(\hat{r})} & \mathbf{r \in MT} \end{cases}, \quad \text{(III-35)}$$

where k is the Bloch vector, G is a reciprocal lattice vector, l and m are the orbital and magnetic quantum numbers, respectively, and $\mathbf{U_l}$ is the regular solution of the radial Schrödinger equation:

$$\left\{\frac{-\hbar^2}{2m}\frac{\partial^2}{\partial r^2} + \frac{-\hbar^2}{2m}\frac{l(l+1)}{r^2} + V(r) - \epsilon\right\} r U_l(r) = 0 \quad \text{(III-36)}$$

Here ϵ is an energy parameter and V(r) is the spherical component of the potential. The coefficients $A_{lm}^{\mu G}$ are determined from the requirement that the wave functions have to be continuous at the boundary of the muffin-tin spheres. Hence, the APWs form a set of continuous basis functions that cover all space, where each function consists of a plane wave in the interstitial region plus a sum of functions, which are solutions of the Schrödinger equation to a given set of angular momentum quantum numbers and a given parameter ϵ, inside the muffin-tin spheres.

No doubt, APW is a good approach that can be used to obtain true valence states in the real potential. However, APW method requires use of an energy dependent secular equation, which is not practical for more than simple solid states systems. There is no clear way to make full potential. The asymptote energy cannot match at energies where U_l equals zero on the sphere boundary. This will happen at some energy problem particular in case of d and f band materials.

III.5.2 The linearized augmented plane wave method (LAPW)

In LAPW method [23], the weakly bonded electrons (e.g. valence electrons) are well described by PW, which are the solutions to the Hamiltonian with a zero potential. On the other hand, a core electron (deep in energy) "feels" practically only the nucleus to which it is bonded and thus it is well described by spherical harmonics (solutions for a single free atom). The LAPW approach combines these two basis sets by setting up a muffin-tin (MT) sphere on each atom. The rest of the space is the interstitial region.

A linear combination of radial functions times spherical harmonics $Y_{lm}(r)$ is,

$$\boldsymbol{\varphi_{Kn}} = \sum_{\mathbf{lm}}[\mathbf{A_{lm,Kn}U_l}(\mathbf{r},\mathbf{E_l}) + \mathbf{B_{lm,Kn}}\dot{\mathbf{U}}_\mathbf{l}(\mathbf{r},\mathbf{E_l})]\mathbf{Y_{lm}}(\hat{r}), \qquad \text{(III-37)}$$

where $U_l(r, E_l)$ is the (at the origin) regular solution of the radial Schrödinger equation for energy E_l and the spherical part of the potential inside sphere; $\dot{U}_l(r, E_l)$ is the energy derivative of U_l evaluated at the same energy E_l. A linear combination of these two functions constitutes the linearization of the radial function; the coefficients A_{lm} and B_{lm} are functions of Kn determined by requiring that this basis function matches (in value and slope) the corresponding basis function of the interstitial region. U_l and $\dot{U}_l$ are obtained by numerical integration of the radial Schrödinger equation on a radial mesh inside the sphere.

Based on whether or not electrons in an atom participate in the chemical bonding with other atoms, the electrons can be divided into two types. One type of electrons are the core electrons, which are extremely bound to their nucleus and thus entirely localized in the MT sphere. The corresponding states are called core states. The other type of electrons is the valence electrons that are leaking out of the MT sphere and bond with other atoms. However, for many elements, the electrons cannot be clearly distinguished like that. Some states are neither constrained in the core states, nor lie in the valence states and are correspondingly termed semi-core states. They have the same angular quantum number l as the valence states but with lower principal quantum number n.

Semi-core states are treated by introducing local orbitals in the LAPW method. Local orbitals do not depend on k and G, but only belong to one atom and have a specific character. They are called local since they are confined to the muffin-tin spheres and thus zero in the interstitial. When applying LAPW on these states, it is thus hard to use one ϵ to determine the two same l. The dilemma is solved by introducing local orbitals (LO), which are defined as,

$$\boldsymbol{\varphi_{lm}^{LO}} = [\mathbf{A_{lm}}\mathbf{U_l}(\mathbf{r}, \mathbf{E_{1,l}}) + \mathbf{B_{lm}}\dot{\mathbf{U}}_\mathbf{l}(\mathbf{r}, \mathbf{E_{1,l}}) + \mathbf{C_{lm}}\mathbf{U_l}(\mathbf{r}, \mathbf{E_{2,l}})]\boldsymbol{\Upsilon_{lm}}(\hat{r}) \quad \text{(III-38)}$$

The coefficients A_{lm}, B_{lm} and C_{lm} are determined by the three requirements that φ^{LO} should be normalized and has zero value and slope at the sphere boundary.

The LAPW method can be extended to non-spherical muffin-tin potentials with a little difficulty, because the basis offers enough variational freedom. This leads then to the full-potential linearized augmented plane wave method (FP-LAPW).

III.5.3 Full-potential linearized augmented plane wave method (FP-LAPW)

The accuracy of the LAPW + lo method can be further improved by using the full potential (FP) [24]. The potential approximated to be spherically inside the muffin-tins, while in the interstitial region, the potential is set to be constant. It is a method used to simulate the electronic properties of materials on the basis of DFT. This method has been successfully applied to study structural phase transitions of certain semiconductors, which increases the number of plane waves in the basis set in order to decrease the structural properties of systems accurately.

The shape of the charge density is taken into account with high accuracy. In this method, the unit cell is divided into two regions as shown in figure (III.2).

In FP-LAPW method, both, the potential and charge density are expanded into lattice harmonics inside each atomic sphere and as a Fourier series in the interstitial region.

$$\mathbf{V(r)} = \begin{cases} \sum_{\mathbf{lm}} \mathbf{V_{lm}(r)Y_{lm}(\hat{r})} & \mathbf{r} \in \mathbf{IR} \\ \sum_{\mathbf{G}} \mathbf{V_G e^{iGr}} & \mathbf{r} \in \mathbf{MT} \end{cases} \qquad \text{(III-39)}$$

Therefore, the plane wave solves the Schrödinger equation in interstitial region, and the product of radial solution times the spherical harmonic solution solve the Schrödinger equation in the muffin-tin region.

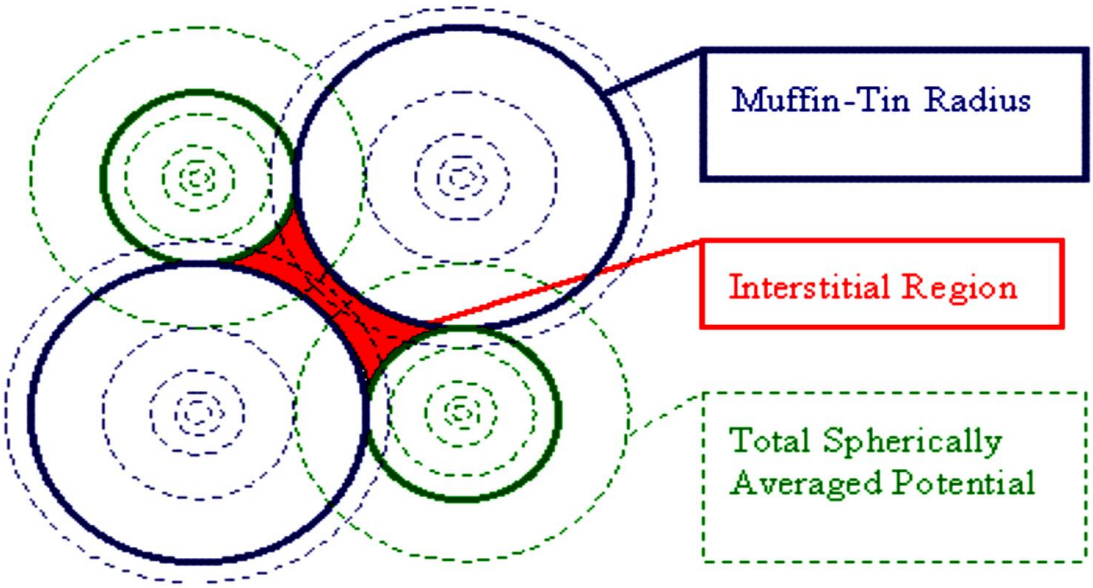

Figure III.2 Unit cell divided into muffin-tin region and interstitial region.

III.6 Computational aspects

WIEN2k is a full-potential all-electron code developed by Blaha et al. [25], at the institute fur Materialchemie, Technical Universitat at Wien, Austria. WIEN2k consists of many independent F90 programs, which are linked together via C-shell scripts.

The code is based on the Kohn-sham formalism of DFT [26-30]. In order to solve these equations, we have to construct the effective Hamiltonian operator, which depends on the electron density of the electronic system. The manner through which the Schrödinger wave equation is solved within WIEN2k code is represented by the flow chart shown below in figure (III.3).

In the newest version WIEN2k [31], the alternative basis set (APW + lo) is used inside the atomic spheres for those important orbitals (partial waves) that are difficult to converge (outermost valence p-, d-, or f-states), or for atoms where small atomic spheres must be used [32-34]. For all the other partial waves, the LAPW scheme is used.

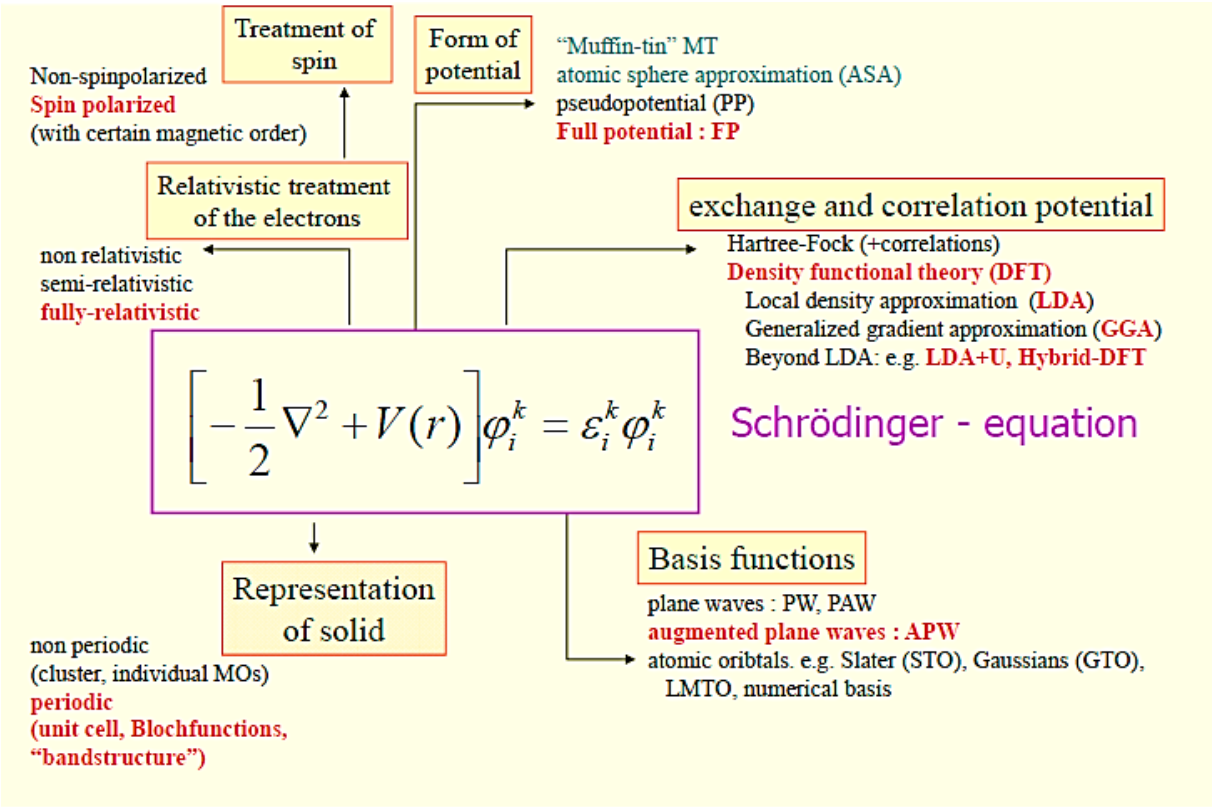

Figure III.3 Representation of the solution of Schrödinger's equation.

III.7 Bibliography

1. Hartree DR (1928) The Wave Mechanics of an Atom with a Non-Coulomb Central Field. Part I. Theory and Methods. Mathematical Proceedings of the Cambridge Philosophical Society, 24: 89–110.
2. Fock V (1930) Näherungsmethode zur Lösung des quantenmechanischen Mehrkörperproblems. Z Physik 61: 126–148.
3. Slater JC (1930) Note on Hartree's Method. Phys Rev 35: 210–211.
4. Thomas LH (1927). The calculation of atomic fields. Mathematical Proceedings of the Cambridge Philosophical Society, 23: 542–548.
5. Fermi E (1928) Eine Statistische Methode zur Bestimmung einiger Eigenschaften des Atoms und ihre Anwendung auf die Theorie des periodischen Systems der Elemente. Z Physik 48: 73–79.
6. Hohenberg P, Kohn W (1964) Inhomogeneous Electron Gas. Phys Rev 136: B864 B871.
7. Kohn W, Sham LJ (1965) Self-Consistent Equations Including Exchange and Correlation Effects. Phys Rev 140: A1133–A1138.
8. Dirac PAM (1930) Note on Exchange Phenomena in the Thomas Atom. Mathematical Proceedings of the Cambridge Philosophical Society, 26: 376–385.
9. Mermin ND (1965) Thermal Properties of the Inhomogeneous Electron Gas. Phys Rev 137: A1441–A1443. (Concerns the generalization to electrons at finite temperatures).
10. Levy M (1979) Universal variational functionals of electron densities, first-order density matrices, and natural spin-orbitals and solution of the v-representability problem. Proc Natl Acad Sci U S A 76: 6062–6065.
11. Becke AD (2014) Perspective: Fifty years of density-functional theory in chemical physics. J Chem Phys 140: 18A301.
12. A. D. Becke, Phys. Rev. A 38, 3098 (1988).
13. J. P. Perdew, K. Burke and M. Ernzerhof, Phys. Rev. Lett. 77, 3865 (1996).
14. J. P. Perdew, in Electronic Structure of Solids '91 , edited by P. Ziesche and H. Eschrig (Akademie Verlag, berlin, 1991).
15. J. P. Perdew, J. A. Chevary, S. H. Vosko, K. A. Jackson, M. R. Pederson, D. J. Singh and C. Fiolhais, Phys. Rev. B 46, 6671 (1992).

16. K. Burke, J. P. Perdew and Y.Wang, Derivation of a generalized gradient approximation: The PW91 density functional (Plenum, NY, 1997), p. 81.
17. A. D. Becke, Int. J. Quantum. Chem. 23, 1915 (1983).
18. J. Tao, J. P. Perdew, V. N. Staroverov and G. E. Scuseria, Phys. Rev. Lett. 91, 146401 (2003).
19. J. Sun, A. Ruzsinszky and J. P. Perdew, Phys. Rev. Lett. 115, 036402 (2015).
20. G. K. H. Madsen, P. Blaha, K. Schwarz, E. Sjostedt and L. Nordstrom, Phys. Rev. B 64 195134 (2001).
21. J. C. Slater, Phys. Rev. 51 151 (1937).] [J. C. Slater, Advances in Quantum Chem. 1 35 (1964).
22. E. Sjostedt, L. Nordstrom and D. J. Singh, Solid State Comm. 114 15 (2000).
23. O. K. Andersen, Phys. Rev. B 12 3060 (1975).
24. J. P. Perdew and Y. Wang, Phys. Rev. B 46 12947 (1992).
25. P Blaha, k Schwarz, G K H Madsen, D Kvasnicka and J Luitz in WIEN2k, An Augmented Plane Wave + Local Orbitals Program for Calculating Crystal Properties, edited by K Schwarz (Technical Universitat wien, Austria, 2001), ISBN 3-9501031-1-2.
26. R. G. Parr and W. Yang, Density Functional Theory of Atoms and Molecules, Oxford University Press, Oxford (1989).
27. R. M. Dreizler and E. K. U. Gross, Density Functional Theory: An Approach to the Quantum Many-Body Problems, Springer, Berlin (1990).
28. J. Callaway and N. H. March, "Density Functional Methods: Theory and Applications", Solid State Physics 38 135 (1984).
29. W. Kohn and A. D. Becke, R. G. Parr, J. Phys. Chem. 100 12974 (1996).
30. N. Argaman and G. Makov, Am. J. Phys. 68 69 (2000).
31. P. Blaha, K. Schwarz, G.K.H. Madsen, D. Kvasnicka, J. Luitz, An augmented plane wave plus local orbitals program for calculating crystal properties, Vienna University of Technology, Austria, 2001, ISBN 3-9501031-1-2.
32. G.H.K. Madsen, P. Blaha, K. Schwarz, E. Sjöstedt, L. Nordström, Phys. Rev. B 64 (2001) 195134-1.
33. K. Schwarz, P. Blaha, G.K.H. Madsen, Comput. Phys. Commun. 147 (2002) 71.
34. G.H.K. Madsen, B.B. Iversen, P. Blaha, K. Schwarz, Phys. Rev. B 64 (2001) 195102-1-6.

Chapter IV

Results and Discussion

The electronic properties, magnetism, mechanical stability and thermoelectric behavior of the ternary X2YZ (X = Fe, Co; Y = Zr, Mo; Z = Ge, Sb) and quaternary XX'YZ (X = Co, Fe; X' = Mo, Fe; Y = Zr, Fe; Z = Sb, Ge) group of Heusler alloys were studied using the full potential linearized augmented plane wave method as implemented in wien2k code (check chapter III for more details about the theoretical ab-initio method).

We have employed the generalized gradient approximation (GGA) suggested by Perdew-Burke-Ernzerhof (PBE) [1] for the electronic exchange-correlation functional.

The cut-off energy separating the core and valence states was set to -6.0 Ry and the number of K-points used in the Brillouin zone after optimization was 3000.

The plane wave cutoff parameter $Rmt*K_{max}$ has been also optimized and set to 9.0. The muffin tin radius was chosen as 2.2 Bohr for all atoms.

For the elastic constants, we have employed the cubic elastic code [2]. While the transport properties were computed using the Boltzmann transport theory as implemented in BoltzTrap code [3].

IV.1 The ternary X_2YZ family (X = Fe, Co; Y = Zr, Mo; Z = Ge, Sb)

IV.1.1 Crystal structure

In chapter II, we have explained the possible structures exhibited by full Heusler alloys (Hg_2CuTi-type and Cu_2MnAl-type structures). In the normal Heusler structure, X atoms occupy a (3/4, 3/4, 3/4) and b (1/4, 1/4, 1/4) sites, and Y atom enters the c (1/2, 1/2, 1/2) site, leaving d (0, 0, 0) site to Z atom in Wyckoff coordinates. However, in the inverse structure, X atoms occupy a and c sites, while Y and Z atoms enter the b and d sites, respectively.

In order to investigate the site preferences of X and Y atoms, we have optimized both inverse Hg_2CuTi- and normal Cu_2MnAl-type structures for Fe- and Co-based ternary compounds and compared their ground-state total energies.

The variation of the total energy as function of volume for the nonmagnetic and ferromagnetic states of both types of structures (presented in figure (IV.1.a)) suggests the stability of the three Fe-based systems, Fe_2ZrGe, Fe_2ZrSb and Fe_2MoSb, in the normal L_{21} structure, while only Fe_2MoGe crystallizes in $CuHg_2Ti$ type structure. The optimized lattice parameters are 6.01 Å, 6.24 Å, 5.95 Å and 6.1 Å for Fe_2ZrGe, Fe_2ZrSb, Fe_2MoGe and Fe_2MoSb, respectively.

For Co_2YZ family (Y = Zr, Mo; Z = Ge, Sb), we found that the normal Heusler structure is adopted when Y site is occupied by Zr element (Co_2ZrGe and Co_2ZrSb). However, when Zr is replaced by Mo atom, the systems (Co_2MoGe and Co_2MoSb) crystallize in the inverse structure (see figure (IV.1.b)). The energy minimum corresponds to a lattice constant of 6.08 Å, 6.28 Å, 5.88 Å and 6.12 Å for Co_2ZrGe, Co_2ZrSb, Co_2MoGe and Co_2MoSb, respectively.

We also notice from figures (IV.1.a) and (IV.1.b) that the ferromagnetic (spin polarized) configuration is lower in energy as compared to the paramagnetic state for all the ternary Fe- and Co-based systems, except Fe_2ZrGe, showing a lower energy in the nonmagnetic state.

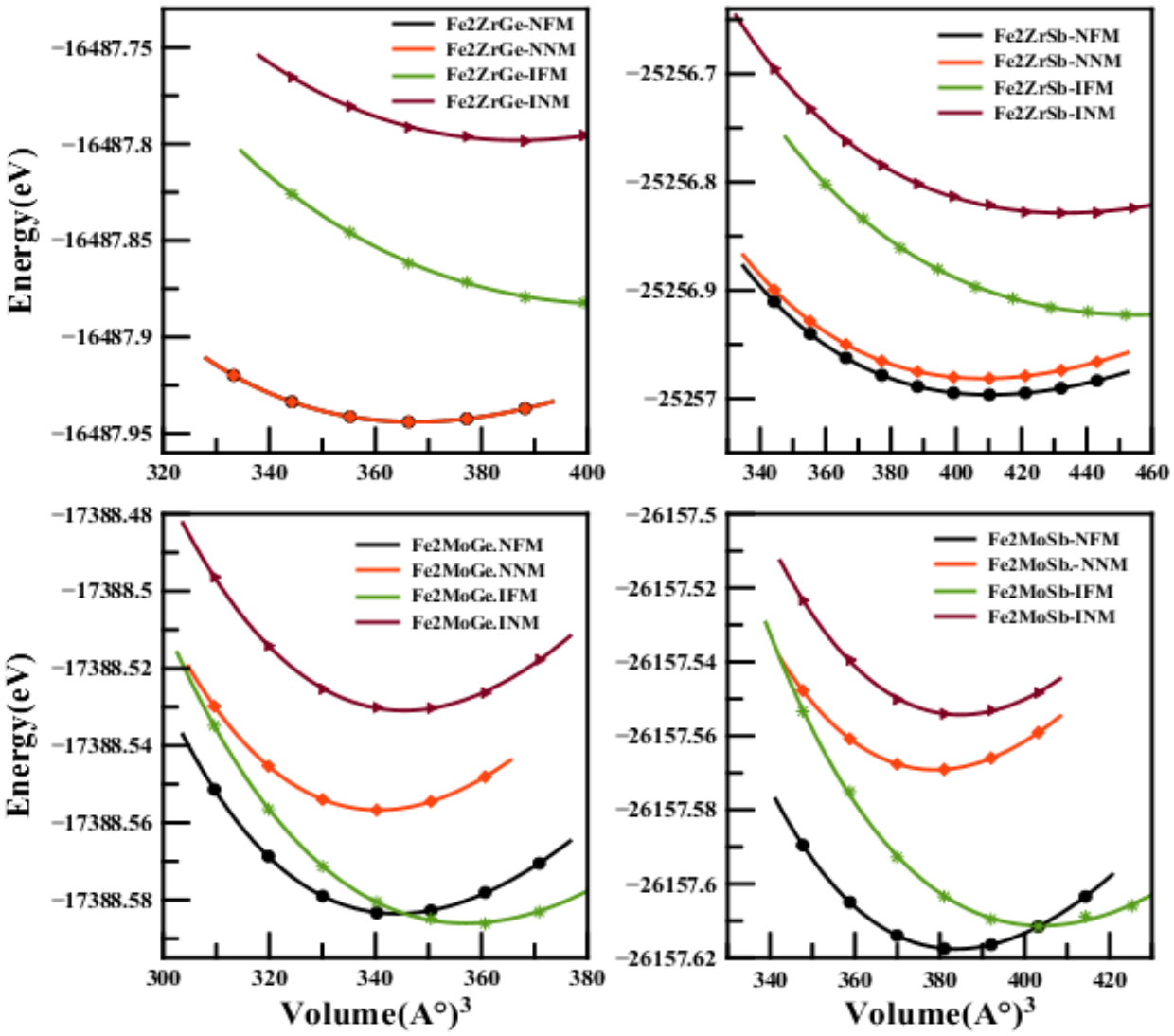

Figure IV.1.a Optimization curves for the ternary Fe-besed Heusler alloys.

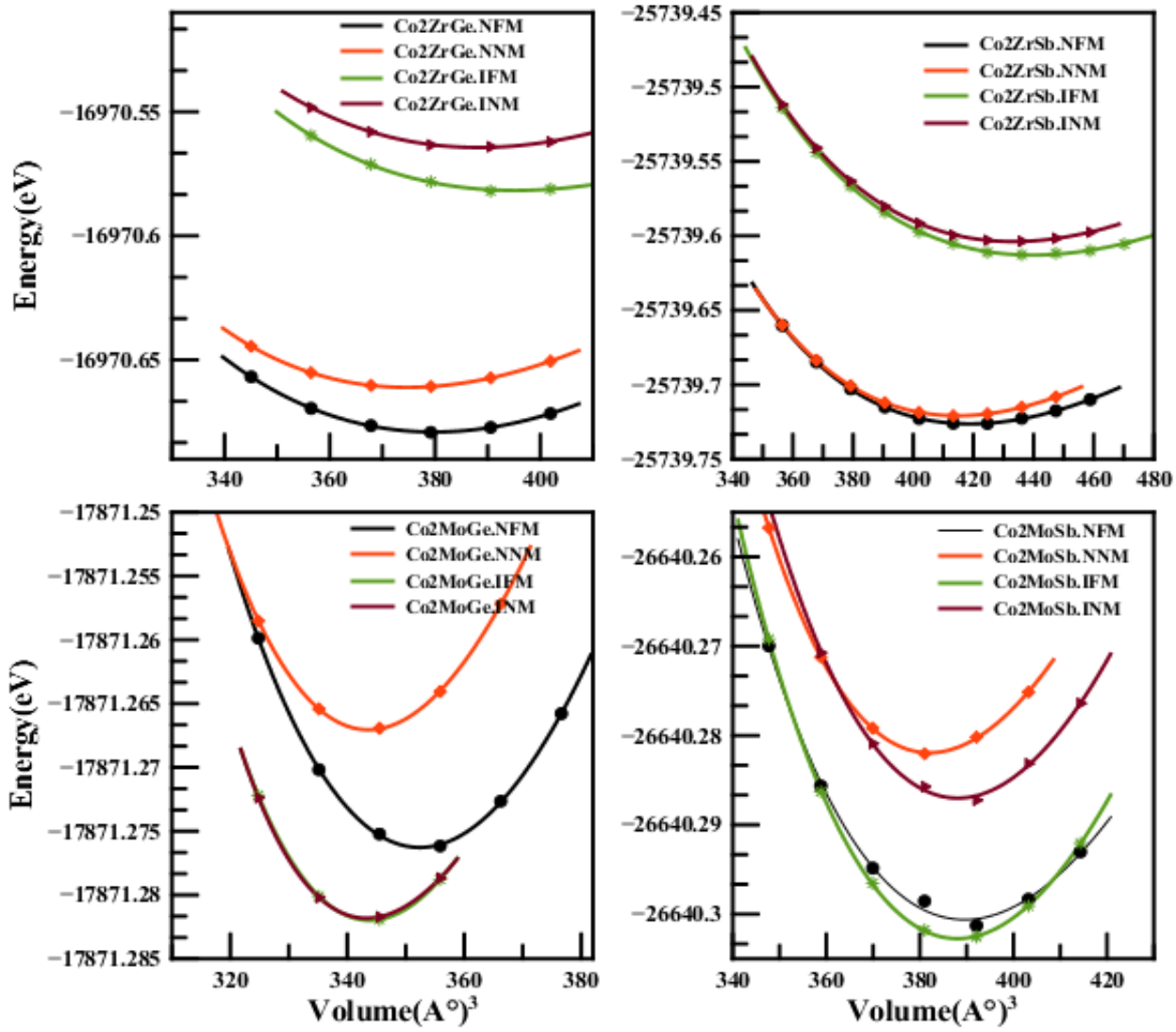

Figure IV.1.b Optimization curves for the ternary Co-based Heusler alloys.

The crystal structure types, equilibrium lattice constants and energy band gaps are listed in table (IV.1).

For each pair of compounds with the same X and Y elements, we notice that the lattice parameter increases by increase of the valence of Z atom (see table (IV.1)).

We also notice from the same table that the lattice constant increases when substituting Fe by Co atom for the compounds crystallizing in the normal Heusler structure. Whereas for the inverse Heusler alloys, the lattice constant decreases when Fe is replaced by Co element.

Table IV.1 Lattice constants, structure type, magnetic moments, the minority spin gap (Eg_{min}) and energy band gaps (Eg_{HM}) of the ternary compounds.

System	***Lattice constant (Å)***	***Structure type***	***Eg_{min} (eV)***	***Eg_{HM} (eV)***
Fe_2ZrGe	6,01 (5.93 for Fe_2ZrSi)	TI	0.135	/
Fe_2ZrSb	6,24	TI	0.73	0
Fe_2MoGe	5,95 (5.78 for Fe_2MoSi)	TII	/	/
Fe_2MoSb	6,10	TI	/	/
Co_2ZrGe	6,08 (6.08)[5] (6.06)[4]	TI	0.59 (0.58)[5] (0.43)[4]	0.32 (0.31)[5]
Co_2ZrSb	6,28	TI	/	/
Co_2MoGe	5,88 (5.78 for Co_2MoSi)	TII	/	/
Co_2MoSb	6,12	TII	/	/

IV.1.2 Electronic properties

The electronic structures of the ternary Fe- and Co-based alloys were studied using first-principles calculations. The band structures presented in figures (IV.2.a) and (IV.2.b) were calculated at equilibrium lattice constants along their high symmetry directions in the Brillouin zone, where the black solid lines represent the majority spin channels and the red dashed lines refer to the minority states. In addition, we present the calculated total and partial magnetic moments in table IV.2.

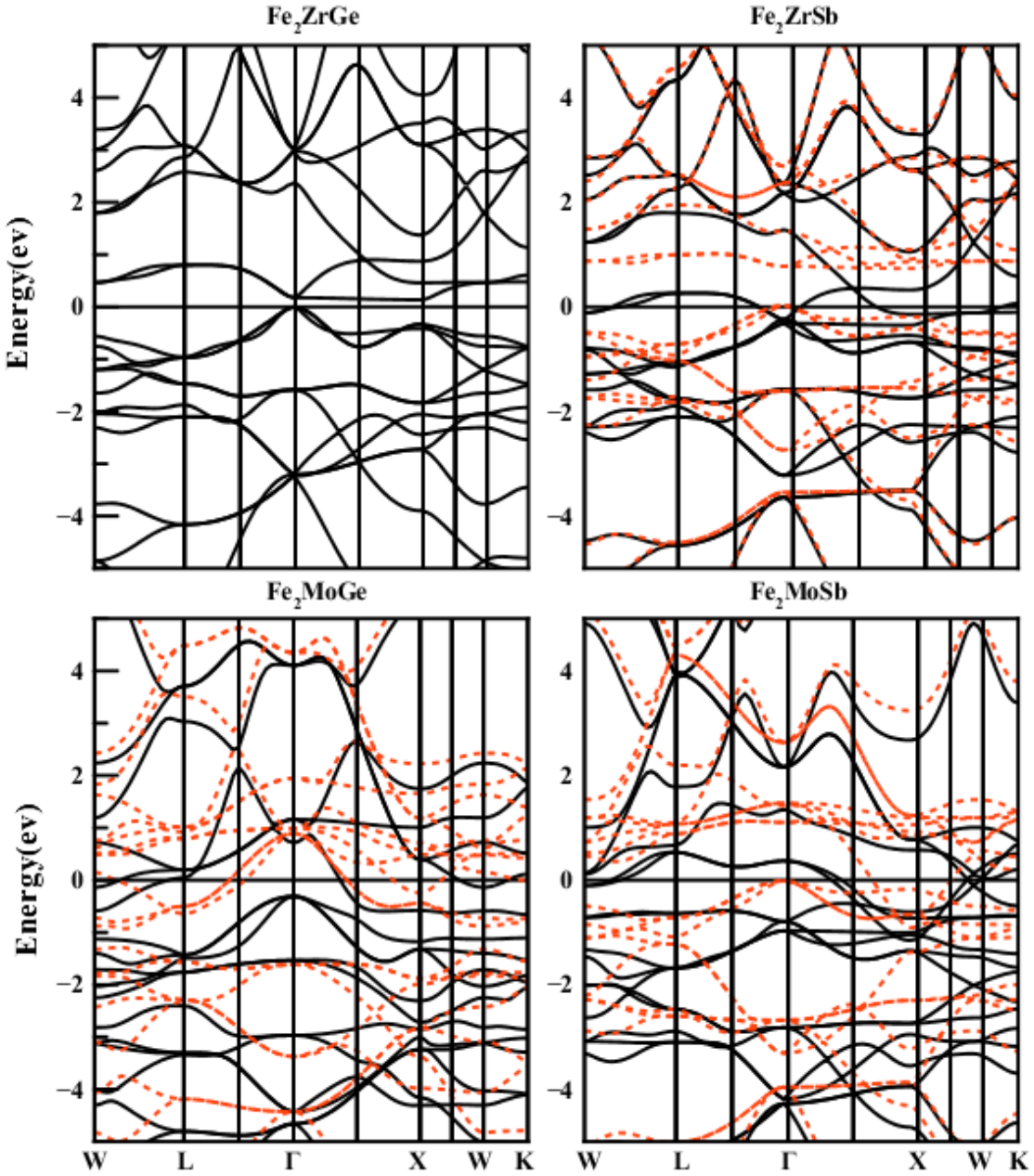

Figure IV.2.a Band structures of the majority and minority spin channels for the ternary Fe-based Heusler alloys.

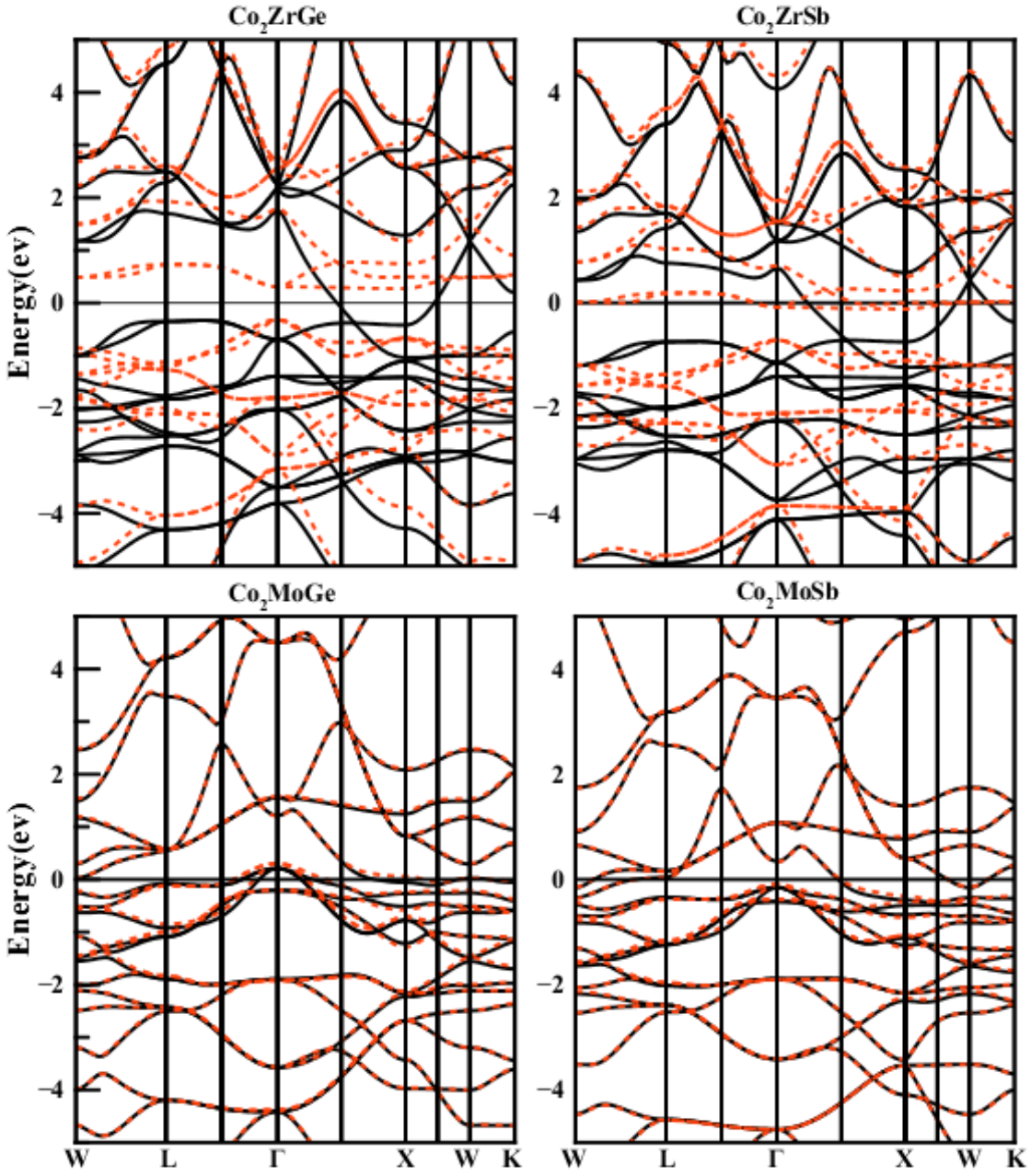

Figure IV.2.b Band structures of the majority and minority spin channels for the ternary Co-based Heusler alloys.

The electronic structure of Fe_2ZrGe shows a flat band at the bottom of the conduction band along Γ-X direction. This alloy with 24 valence electrons is consistent with the Slater Pauling rule [6] and exhibits a magnetic moment of 0 μ_B, indicating a semiconducting behavior. The obtained band gap is indirect with a value of about 0.14 eV.

When replacing Ge by Sb (Fe_2ZrSb), we notice the stability of the ferromagnetic phase. The band structure calculations show a metallic aspect in spin up channel, while the minority spin states is semiconducting. Hence, Fe_2ZrSb is a half-metallic ferromagnet with a magnetic moment of 0.99 μ_B. The band gap is also indirect and it is located around Fermi level (E_F) in the minority-spin channel.

For Fe_2MoSb, the band structure shows a metallic behavior with a moderate moment of 2.81 μ_B, which is close to the one predicted by Slater Pauling rule ($3\mu_B$).

The last compound in Fe-based series, Fe_2MoGe, crystallizing in the inverse Hg_2CuTi type structure, is characterized by a metallic aspect and it shows a magnetic moment of almost 3.55 μ_B, which disobeys Slater Pauling predictions.

For Co_2ZrGe, the band structure shows a half-metallic aspect with a magnetic moment of 1.96 μ_B (2 μ_B according to Slater Pauling rule). An ideal band structure with a magnetic moment of 2.00 μ_B has already been determined in [4] and [5]. The difference in the resulting magnetic moments confirms the importance of the atomic positions on the structural properties of Heusler alloys [7].

Co_2ZrSb, on the other hand, is an ordinary magnetic alloy with a magnetic moment of 1.69 μ_B, which is far less from the predictions of Slater Pauling rule ($3\mu_B$).
The next two compounds, Co_2MoGe and Co_2MoSb, both crystallizing in the inverse Heusler structure, show similar features around Fermi level in both spin directions. The magnetic moments were found to be 0.16 μ_B and 0.20 μ_B, respectively, which disobeys Slater's predictions.

Table IV.2 Unit cell total magnetic moments M_{tot} and atomic moments Mi of constituent i for the ternary full Heuslers. N_v is the number of valence electrons of the systems.

Systems	N_v	M_x	$M_{x'}$	M_y	M_z	M_{int}	M_{tot}
Fe_2ZrGe (TI)	24	0.00	0.00	0.00	0.00	0.00	0.00
Fe_2ZrSb (TI)	25	0.65745	0.65745	-0.15185	-0.01979	-0.14675	0.99651
Fe_2MoGe (TII)	26	1.78877	2.22991	-0.36676	0.00748	-0.11187	3.54752
Fe_2MoSb (TI)	27	1.31352	1.31352	0.19772	-0.01415	0.00049	2.81110
Co_2ZrGe (TI)	26	1.08258	1.08258	-0.09574	0.02929	-0.13373	1.96470
Co_2ZrSb (TI)	27	0.90737	0.90737	-0.05440	0.02690	-0.09288	1.69436
Co_2MoGe (TII)	28	0.23990	-0.02800	-0.02460	-0.00783	-0.01630	0.16316
Co_2MoSb (TII)	29	0.33771	0.14250	-0.18359	-0.01259	-0.08020	0.20383

Generally, the hybridizations between the d-orbitals of transition metals is mainly responsible of the existence of the minority gap, while the s-p elements are very important for the structural stability of Heusler alloys. To better understand these hybridizations [8], we have calculated the total and partial densities of states (DOS) of the ternary Heusler alloys as shown in figures (IV.3.a) and (IV.3.b). The positive DOS values represent the majority-spin channel and the negative values represent the minority-spin states. From these figures, we notice that the s-bands of Sb and Ge atoms are very low in energy, and are located in an isolated range of -12.5 eV to -10.5 eV, and -11 eV to -9 eV, respectively

The Sb-p orbitals contribute significantly to the density of states of X_2YSb compounds. Likewise, Ge-p orbitals contribute to the density of states in an energy region between ~ -7 eV and -3 eV. These s and p-states show almost identical band structures for the two spin directions in both series and are hybridized with X and Y d-electrons, which explains the small negative moments of these s-p elements.

Fe_2ZrGe with 24 valence electrons is a semiconductor with a narrow band gap. In this compound, Fe d-states dominate the higher valence band, while they are located at about 0.14 eV above the conduction band. Whereas Zr d- orbitals are split into occupied states lying around -2 eV below Fermi level and unoccupied states in the lowest conduction band above. Primly, the electronic structure of Fe_2ZrGe compound shows the same behavior as the majority channel of Fe_2ZrSb, except that in the latter, the Fermi level is located above the conduction band.

The spin up channel of Fe_2ZrSb is also characterized by Fe d-states surrounding E_F, while Zr d-orbitals are located in the unoccupied part of this channel. The minority spin states present significant band gaps in the partial DOS. These gaps are larger for Y and Z atoms as compared to X element. In this compound, Fe d-states surrounding the half-metallic gap hybridize with Zr d-orbitals, opening a large indirect gap of 0.73 eV above Fermi level.

For Fe_2MoGe with type II structure, the d-states of both Fe atoms contribute the most to the total DOS below Fermi level, while Mo d-orbitals extend into the unoccupied part of the majority spin channel. Spin down channel is characterized by a pseudo gap below Fermi level. Fe_I d-states are localized around E_F and are coupled to Fe_{II} and Mo d-orbitals below Fermi level, which explains the reduction in the moment of Fe_I atom. Fe_2MoGe totally disagrees the rule of 24.

For Fe_2MoSb, we notice that Fe d-states participate the most to the total DOS. The majority channel shows three main peaks below Fermi level that belong to Fe atom with small contributions from Mo element. The minority channel is characterized by Fe d-states mixed to Mo d-orbitals constituting two main peaks below E_F. While above, we notice that Fe and Mo d-orbitals constitute a large peak. The interactions between the d-states of the transition elements cause a reduction in the moment of Mo atom, leading to a deviation of the total moment of the system from the predicted one.

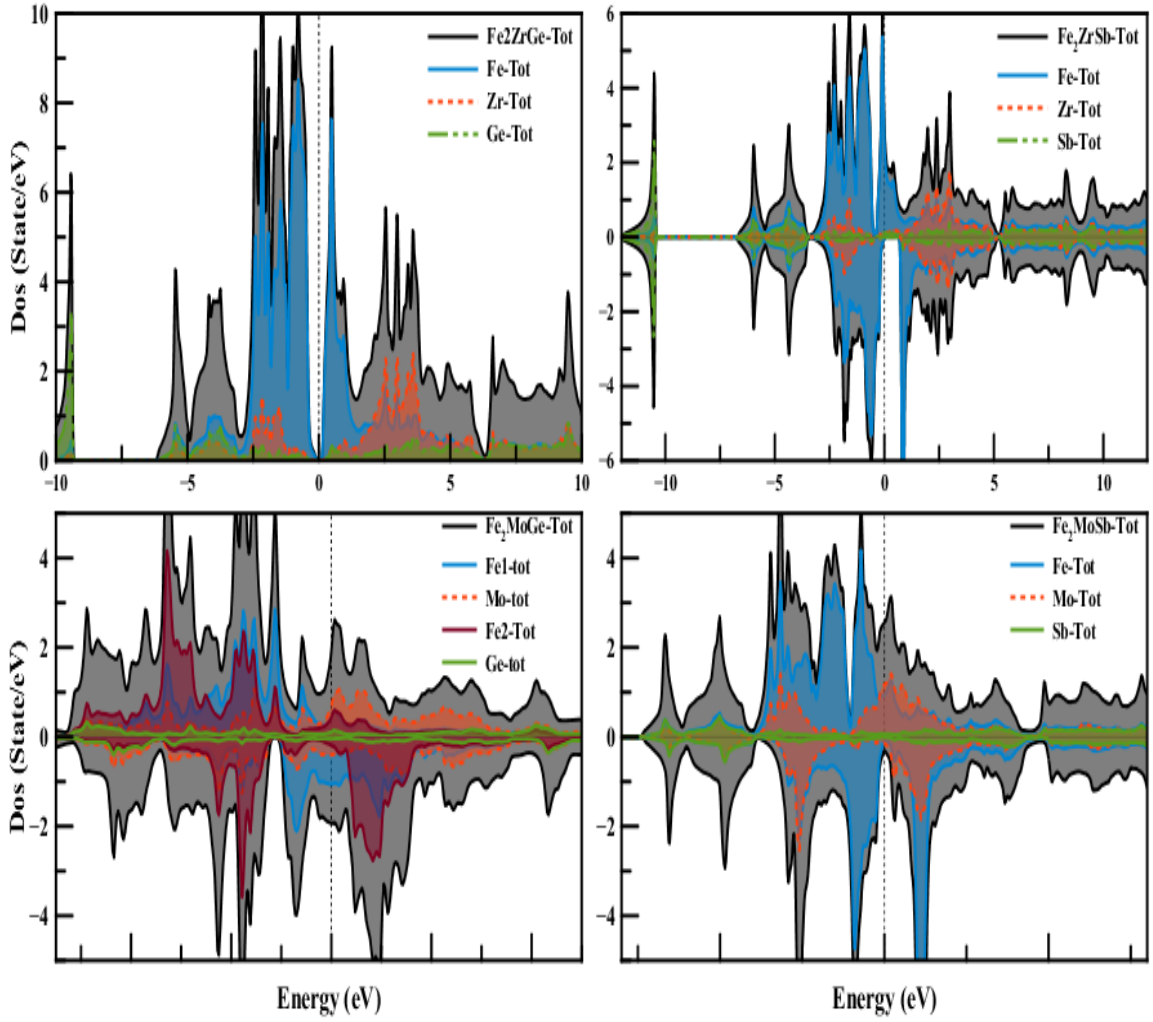

Figure IV.3.a Total and partial densities of states for the ternary Fe-based Heusler alloys.

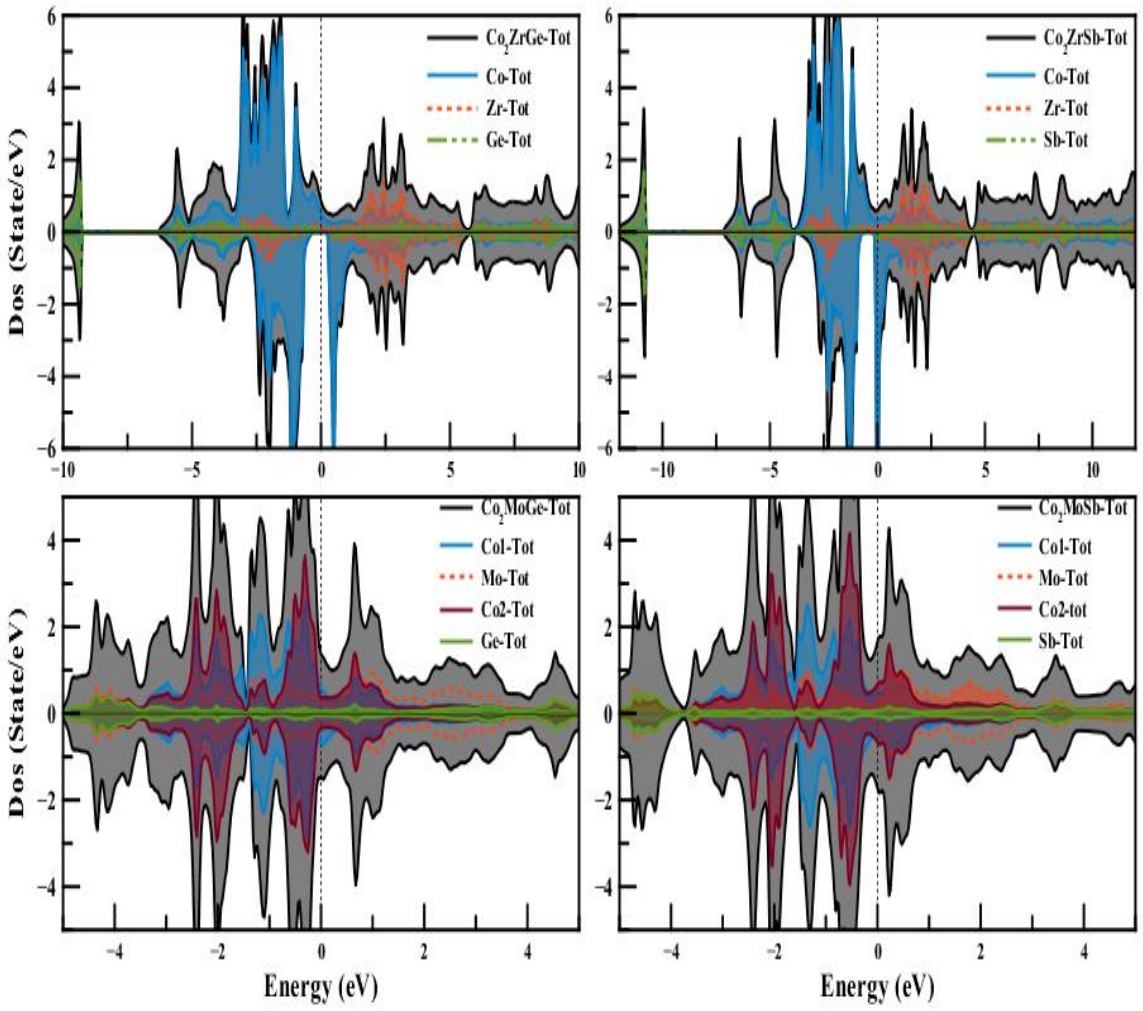

Figure IV.3.b Total and partial densities of states for the ternary Co-based Heusler alloys.

Moving on to Co-based series, where we notice that the magnetic moments of Co atoms in compounds with TII structure are considerably reduced as compared to those crystallizing in TI Heusler structure. Moreover, the interaction between X (or X') and Y element is antiparallel for all Co-based systems.

For Co_2ZrZ (Z = Ge, Sb) alloys, the magnetic moments carried by Co atoms decrease with increasing the number of valence electrons, while the densities of states of these two systems are almost identical. The Fermi level in Co_2ZrGe lies almost at the center of the minority band gap and it is limited by 0.32 eV below E_F and 0.27 eV above. This results in an equal band gap to that characterizing the minority channel of Co_2ZrSb (0.59 eV), where the Fermi level is situated near the conduction band. For both Co_2ZrZ alloys, the bonding states of the majority channel mostly exist at the higher valence transition metal element, while the unoccupied antibonding bands mainly exist at Zr 4d-orbitals. In addition, the spin down gap occurred by Zr atoms is broader than the one presented by Co elements around E_F.

As compared to Co_2ZrGe, the minority conduction band of Co_2ZrSb constitutes a large peak extending upon the Fermi level. Co_2ZrGe have already been reported as a perfect half-metal with a moment of exactly $2.00\mu_B$ [4,5], where the difference in the partial and total magnetic moments is related to the difference in atomic positions. For the same reason, the magnetic moment of Co atom has been reduced in Co_2ZrSb system, causing a loss of the half-metallic properties.

The electronic structure of Co_2MoZ pair exhibits almost identical features in majority and minority spin channels, where Co_I and Co_{II} d-orbitals show the major contributions to the total DOS with small contributions from Mo d-states. These states are very mixed around E_F and they extend along the conduction band. For both Co_2MoZ materials, the energy range between -3.0 and 1.0 eV is relative to the d-states of the transition metal elements cutting through the Fermi level. Moreover, the magnetic moment of Co atoms is very small and negative in the case of Co_2MoGe (Co_{II} atom precisely). The similarities between spin up and spin down channels support the metallic character of these two compounds.

IV.1.3 Elastic properties

Calculating the elastic parameters of a material helps to provide information about its ductility and stiffness. The three elastic constants $\boldsymbol{C_{11}}$, $\boldsymbol{C_{12}}$ and $\boldsymbol{C_{44}}$ were calculated by relaxing the unit cell in the optimized configurations. We remind of the Born-Huang criteria [9], unleashing the conditions of mechanical stability for a cubic system as follows:

$$\boldsymbol{C_{44} > 0}, \qquad \boldsymbol{\frac{(C_{11}-C_{12})}{2} > 0}, \qquad \boldsymbol{C_{12} < B < C_{11}}$$

According to the previous Born-Huang criteria, only four compounds Fe_2ZrSb, Co_2ZrGe and Fe_2MoZ (Z = Ge, Sb), were found to be mechanically stable. As for Fe_2ZrGe, Co_2ZrSb and Co_2MoZ alloys, we notice that C_{11} is much smaller than C_{12}, which overbalances their mechanical instability. Because these materials are not mechanically stable, the remaining elastic parameters will be discussed for the four stable systems only.

The hardness of each alloy was measured by estimating the values of the Bulk modulus (B), where large values of B characterize stiffed materials. While the shear modulus (G) has been evaluated using the following Voigt [10] and Reuss [11] expressions:

$$\boldsymbol{G_R = \frac{5C_{44}(C_{11}-C_{12})}{4C_{44}+3(C_{11}-C_{12})}} \quad , \quad \boldsymbol{G_V = \frac{C_{11}-C_{12}+3C_{44}}{5}}$$

Young's modulus (E) is another indicator of the stiffness of materials, where high values of E define stiff alloys. The estimated bulk (**B**) and shear (**G**) values as well as the values of Young's modulus listed in table (IV. 3) indicate that all of Fe_2ZrSb, Co_2ZrGe and Fe_2MoZ materials may be stiff in nature.

Poisson's ratio (υ) [12] and Pugh's factor ($\boldsymbol{k}$) [13] give information of the brittle or ductile character in a given material. Poisson's ratio is less than 0.26 for brittle materials. In addition, the material is considered ductile if the ratio of $\boldsymbol{B/G}$ is above 1.75, otherwise, it is brittle.

In the case of Co_2ZrGe and Fe_2MoZ alloys, although exhibiting positive values of Cauchy pressure, the values of $\boldsymbol{\upsilon}$ are less than 0.26, meaning that these alloys may be brittle in nature. They also possess small values of $\boldsymbol{B/G}$, which confirms their brittleness.
On the other hand, the large positive $\mathbf{C_p}$, large $\boldsymbol{B/G}$ and $\boldsymbol{\upsilon}$ of Fe2ZrSb indicate its enhanced ductility.

In addition, all of these ternary compounds can be considered as anisotropic regarding their small values of anisotropy factor [14]. These values are also different from unity, which indicates the structural stability of Fe_2ZrSb, Co_2ZrGe and Fe_2MoZ systems.

Table IV.3 Elastic constants (GPa) of the ternary Heuslers.

	C_{11}	C_{12}	C_{44}	B	G	E	υ	A	k	C_p	T_{melt}
Fe_2ZrGe	21.02	524.9	221.2	356.9	20.08	59.12	0.47	-0.88	17.78	303.7	1567.6 $\pm 300K$
Fe_2ZrSb	265,7	195.3	126.3	218.7	75.75	203.7	0.34	3.59	2.89	69	1469.9 $\pm 300K$
Fe_2MoGe	203.2	152.4	81.23	169.3	137.5	324.6	0.18	3.2	1.23	71.17	1753.9 $\pm 300K$
Fe_2MoSb	238.5	179.7	102.9	199.3	-1054.7	4141.4	-2.96	3.5	-0.19	76.8	677.2 $\pm 300K$
Co_2ZrGe	229.7	131.7	85.9	164.4	243.75	489.3	0.004	1.75	0.67	45.8	1910.5 $\pm 300K$
Co_2ZrSb	97.84	175.6	78.7	149.7	-149.48	-672.1	1.25	-2.02	-1.00	96.92	1131.2 $\pm 300K$
Co_2MoGe	171.7	179.1	121.7	176.6	161.65	371.6	0.15	-32.9	1.09	57.4	1962.6 $\pm 300K$
Co_2MoSb	155.1	181.2	444.9	172.5	194.6	424.2	0.09	-34.1	0.89	-263.7	2123.4 $\pm 300K$

Finally, we have estimated the melting temperature [15] related to the elastic constant $\boldsymbol{C_{11}}$ as follows:

$$\boldsymbol{T_{melt} = [553K + \left(\frac{5.91K}{GPa}\right) C_{11}] \pm 300K}$$

Obviously, the material with higher elastic constant has higher melting temperature. All four stable systems show high values of melting temperature, which supports their ability of preserving their crystal structures in a large range of temperature changes.

In the purpose of developing further new half-metals, we have formed eight quaternary structures based on the same atomic composition of the previous ternary Heuslers, only by replacing one X atom by a different 3d or 4d element.

The next part of this chapter will be focusing on the electronic properties, mechanical stability and thermoelectric efficiency of the quaternary systems.

IV.2 The quaternary XX'YZ family (X = Co, Fe; X' = Mo, Fe; Y = Zr, Fe; Z = Sb, Ge)

IV.2.1 Crystal structure

Commonly, quaternary Heusler alloys crystallize in the LiMgPdSn structure (F-43m) with four atoms occupying (0, 0, 0), (1/2, 1/2, 1/2), (1/4, 1/4, 1/4), and (3/4, 3/4, 3/4) Wyckoff positions. They have three structural prototypes labelled as type1, type2 and type3 that differ only in their atomic positions (see table IV.4).

If we consider Z atom at (0, 0, 0) position, the remaining three X, X′ and Y atoms will be placed in three different face centered cubic (fcc) sublattices in three non-degenerate ways.

The site preferences for the studied quaternary systems may be explained as follows:

The stability of the least electronegative Y atom (in this case Zr with 1.33 and Fe with 1.83 Pauli units) depends on losing its electrons to other elements in the system. Simultaneously, the most electronegative Z atom (2.01 and 2.05 Pauli unit for Ge and Sb respectively) tries to accept electrons from other elements. Therefore, these two occupy tetrahedral sites forming an ionic type sublattice. Whereas X and X' having intermediate electronegativities occupy tetrahedral sites.

Table IV.4 Site occupancy in the quaternary Heusler structure for different types of atomic arrangements.

Structure type	***a(1/4, 1/4, 1/4)***	***b(1/2, 1/2, 1/2)***	***c(3/4, 3/4, 3/4)***	***d(0, 0, 0)***
Type 1	X	X'	Y	Z
Type 2	X	Y	X'	Z
Type 3	X'	X	Y	Z

In order to confirm the ground state structure of the quaternary Heusler alloys, we have calculated the total energy as function of the lattice constant (E_{tot} / a) for three different atomic arrangements (see figures (IV.4.a) and (IV.4.b)). We report as well the structure types, equilibrium lattice constants (a_0), number of valence electrons (N_V) and energy band gaps (Eg) in table (IV.5).

From figures (IV.4.a) and (IV.4.b), we notice that the most stable configuration for XX'ZrZ (X = Co, Fe; X' = Mo, Fe; Z = Ge, Sb) alloys corresponds to type 2 structure. This type of structure has the occupation of octahedral sites d (0, 0, 0) and b (1/2, 1/2, 1/2) by Z element and Zr, respectively.

Whereas X and X' are at a (1/4, 1/4, 1/4) and c (3/4, 3/4, 3/4) tetrahedral sites, respectively. This is confirmed by implying the rule of electronegativities, where in structure type 2 and by fixing the s-p element at d position, b site is always occupied by the least electronegative transition metal element, which is Zr atom (1.33) in the case of the six XX'ZrZ (X = Co, Fe; X' = Mo, Fe; Z = Ge, Sb) alloys.

Whereas for CoMoFeZ (Z = Ge, Sb) systems, the lowest energy versus volume curve corresponds to type 1 structure with the occupation of a (1/4, 1/4, 1/4) position by Co atom, Mo at b (1/2, 1/2, 1/2) and Fe at c (3/4, 3/4, 3/4). In this case, both Fe and Co elements have close values of electronegativities, leading to a structure type 1. The octahedral sites are occupied by the main group element (Ge/Sb) and the most electronegative of the three transition elements (Mo), while the tetrahedral sites are occupied by the two other transition metal elements (Co and Fe).

Figures (IV.4.a) and (IV.4.b) also show that the ferromagnetic phase is lower in energy as compared to the paramagnetic state for all XX'YZ quaternary Heuslers.

An increase in the lattice constant and decrease in the bulk modulus is observed for CoX'YZ materials (X' = Fe, Mo; Y = Fe, Zr; Z = Ge, Sb) with a number of valence electrons over 24. While the bulk modulus of XMoZrZ (X = Co, Fe; Z = Ge, Sb) compounds, having a number of valence electrons that is equal or less than 24, increases with increasing lattice constants (see table IV.5).

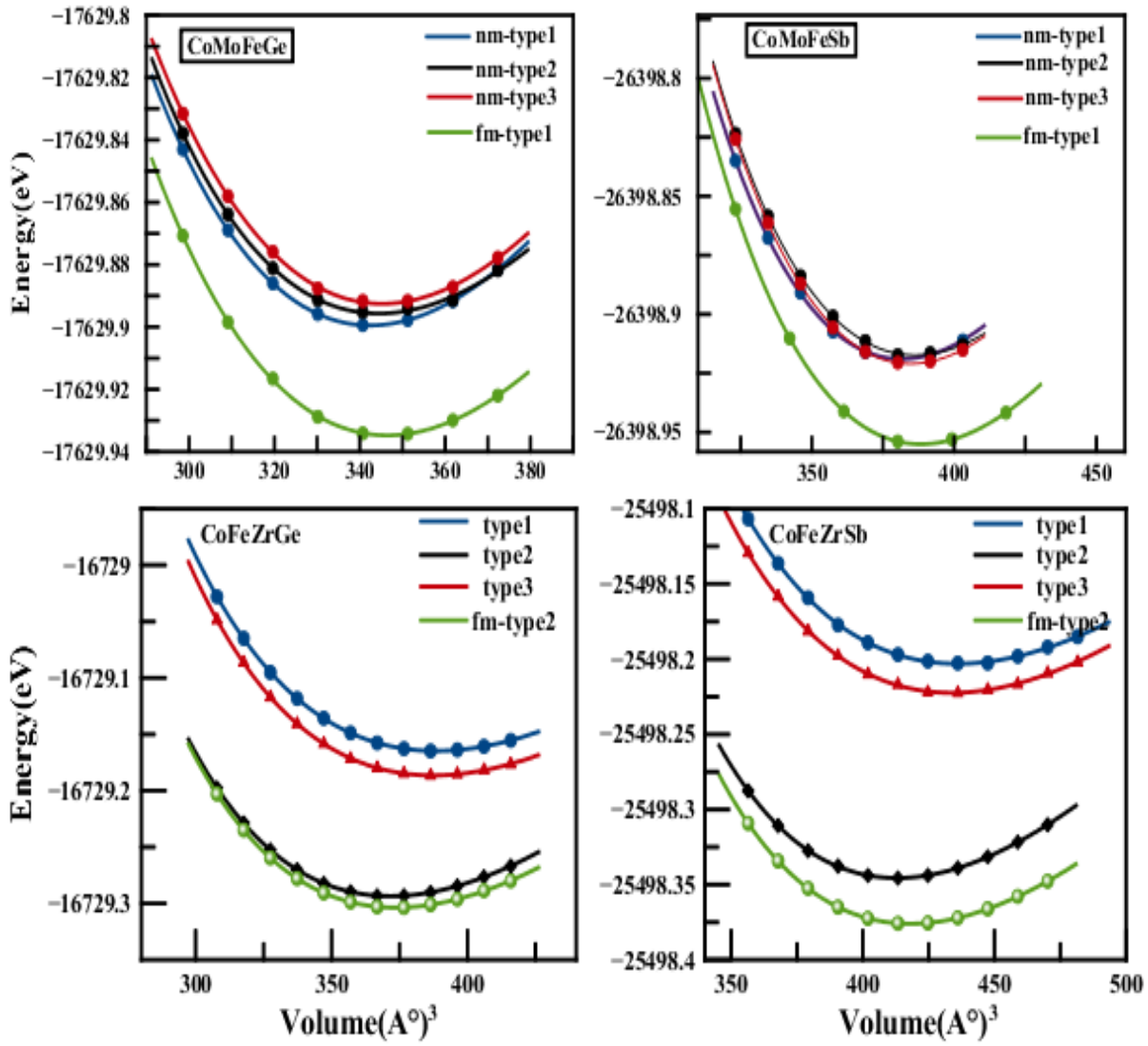

Figure IV.4.a The three possible atomic arrangements (type 1, type 2 and type 3) for CoX'YZ (X' = Mo, Fe; Y = Zr, Fe; Z = Ge, Sb) quaternary Heuslers calculated for the nonmagnetic state. The ferromagnetic state was estimated only for the most stable nonmagnetic total energy.

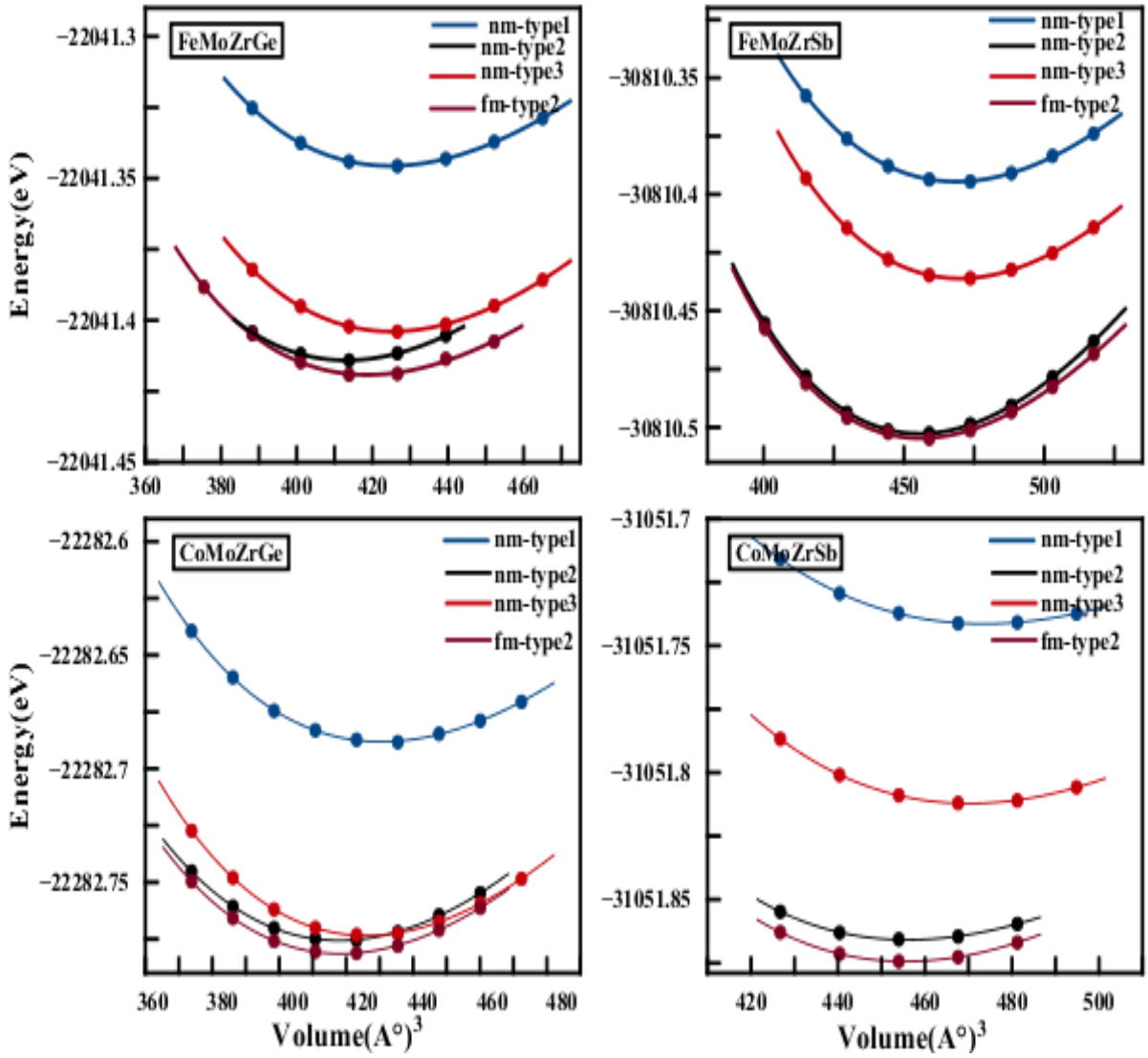

Figure IV.4.b The three possible atomic arrangements (type 1, type 2 and type 3) for XMoZrZ (X = Co, Fe; Z = Ge, Sb) quaternary Heuslers calculated for the nonmagnetic state. The ferromagnetic state was estimated only for the most stable nonmagnetic total energy.

Table IV.5 Optimized lattice constants a_0, number of valence electrons N_V, Bulk modulus (B) and band gaps (Eg) for quaternary Heusler compounds.

System	*N_V*	*Magnetic state*	*Structure type*	*E_{tot} (eV)*	*a_0 (A°)*	*B (GPa)*	*Half-metallicity*	
							Eg_{min}	**Eg_{HM}**
FeMoZrGe	22	NM	Type1	-22041.345615	6.3143	156.9121		
			Type2	-22041.414087	6.2559	171.9438		
			Type3	-22041.403940	6.3161	168.7521		
		FM	Type2	-22041.419194	6.2841	156.4103	/	/
FeMoZrSb	23	NM	Type1	-30810.394544	6.5249	141.9657		
			Type2	-30810.502722	6.4636	169.0049		
			Type3	-30810.436101	6.5305	157.5264		
		FM	Type2	-30810.504665	6.4647	159.6964	/	/
CoMoZrGe	23	NM	Type1	-22282.688142	6.3427	149.3693		
			Type2	-22282.775644	6.2803	164.3353		
			Type3	-22282.773482	6.3205	171.4521		
		FM	Type2	-22282.781460	6.2823	165.1552	/	/
CoMoZrSb	24	NM	Type1	-31051.741379	6.5471	135.1610		
			Type2	-31051.865877	6.4655	148.6458		
			Type3	-31051.812168	6.5316	156.7892		
		FM	Type2	-31051.874392	6.4630	165.5031	/	/
CoFeZrGe	25	NM	Type1	-16729.164772	6.1287	158.8694		
			Type2	-16729.293588	6.0395	182.2885		
			Type3	-16729.186504	6.1233	161.7539		
		FM	Type2	-16729.303712	6.0501 [16]	177.9919	0.50089 [16]	0.00369 [16]
CoFeZrSb	26	NM	Type1	-25498.203085	6.3695	133.6173		
			Type2	-25498.345624	6.2552	166.3653		
			Type3	-25498.222435	6.3587	138.8768		
		FM	Type2	-25498.376041	6.2809 [16]	158.7701	0.67753	0.16547
CoMoFeGe	27	NM	Type1	-17629.899482	5.8766	232.7758		
			Type2	-17629.895676	5.8885	205.3062		
			Type3	-17629.892540	5.8925	226.5456		
		FM	Type1	-17629.934747	5.8995	219.5824	/	/
CoMoFeSb	28	NM	Type1	-26398.918999	6.0922	210.3784		
			Type2	-26398.917362	6.1176	194.1589		
			Type3	-26398.915491	6.1223	191.4277		
		FM	Type1	-26398.955097	6.1104	193.6095	/	/

IV.2.2 Magnetic moments and electronic properties

We present the band structures of the quaternary XX'YZ (X = Co, Fe; X' = Mo, Fe; Y = Zr, Fe; Z = Sb, Ge) Heusler alloys in figures (IV.5.a) and (IV.5.b), where the black solid lines represent the majority channels and the red dashed lines represent the minority states. We have also listed their total and atomic moments in table (IV.6).

Only two compounds, CoFeZrGe and CoFeZrSb, were found to exhibit a true half-metallic character. In these systems, the bands cross the Fermi level in spin up channel indicating a metallic behavior while the minority spin states shows no band at Fermi level, indicating a semiconducting behavior.

CoFeZrZ (Z = Ge, Sb) compounds with the magnetic moments 1 μ_B and 2 μ_B, respectively, agree well to the Slater Pauling rule, where Fe and Co atoms contribute the most to the total moment (see table (IV.6)), while the interactions between 4d and 3d elements is antiparallel. In CoFeZrGe, the BC_{min} is located at 0.49 eV at X point, and the BV_{max} at -0.036 eV at Γ point, creating an indirect band gap with a value of 0.5 along Γ-X direction. An indirect band gap of 0.67 eV is also observed in the band structure of CoFeZrSb alloy, with the BV_{max} at -0.16 eV at Γ point and the BC_{min} at 0.51 eV along X direction.

For both half-metallic quaternary CoFeZrZ systems, X and X' are 3d transition elements and Y is a 4d atom. The first was derived from the ternary parents Co_2ZrGe (a stable half-metal) and Fe_2ZrGe (an unstable semiconductor). Whereas the second is a combination of the unstable magnetic Co_2ZrSb and the stable half-metallic Fe_2ZrSb. The ternary parents of each quaternary half-metal were found to crystallize in the normal Heusler structure. Moreover, they do not share the same character; however, one of them adopts a half-metallic aspect. In other words, we found that the half-metallic properties could be transferrable from only one half-metallic ternary parent even if the other parent exhibits a magnetic character.

For the rest of materials with X being a 3d element and X' and Y being 4d transition metals, the bands cross the Fermi level in both spin states, meaning that no true half-metallic gap could exist in any of these systems.

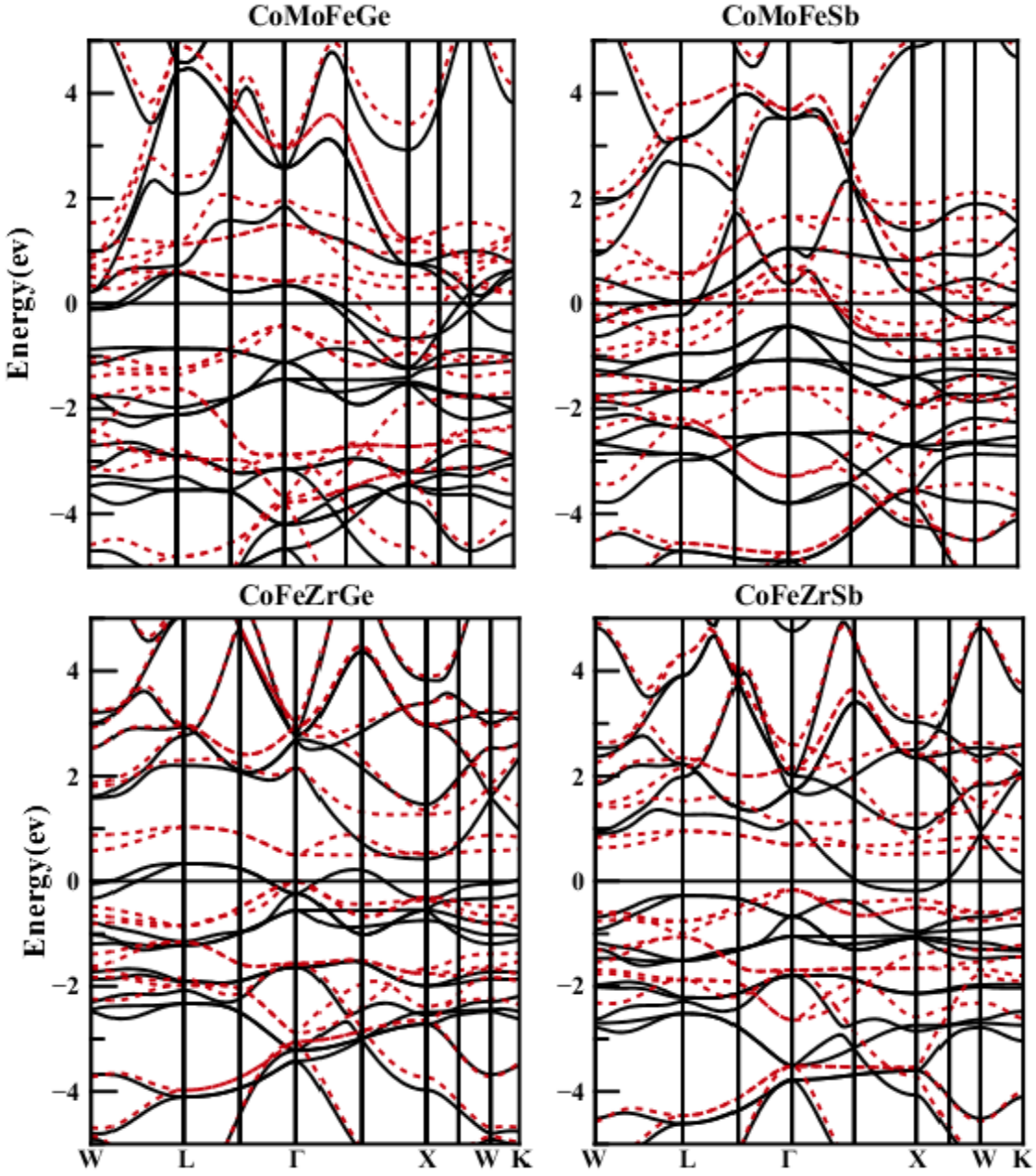

Figure IV.5.a Band structures of the majority and minority spin channels for CoX'YZ (X' = Mo, Fe; Y = Zr, Fe; Z = Ge, Sb) quaternary alloys.

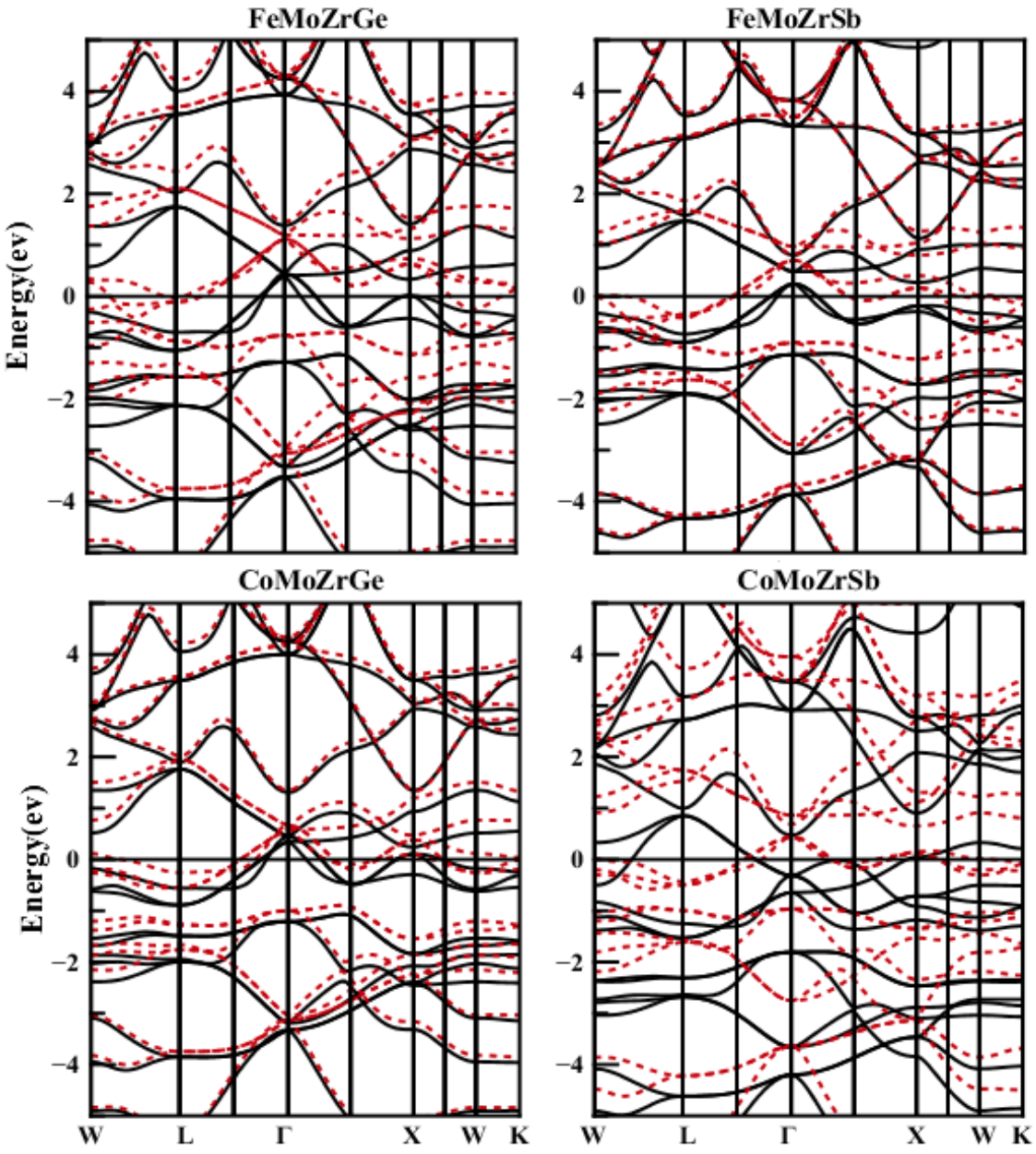

Figure IV.5.b Band structures of the majority and minority spin channels for XMoZrZ (X = Co, Fe; Z = Ge, Sb) quaternary alloys.

For the pair CoMoZrZ, the magnetic moments according to Slater Pauling's rule should be $1\mu_B$ and $0\mu_B$, respectively. All constituents of these two Heuslers are coupled ferromagnetically. CoMoZrSb is the only alloy showing a much deviated moment than the predicted one. It is a combination of the stable magnetic Co_2ZrSb crystallizing in the normal Heusler structure and the metallic Co_2MoSb with the inverse type structure. Noticeably, CoMoZrSb follows the same character of the ternary parents since they were both found to deviate from the rule of 24.

Whereas CoMoZrGe, with a combination of the unstable half-metal Co_2ZrGe with the normal Heusler structure and the stable magnetic Co_2MoGe with the inverse structure, shows a moderate moment of $0.84\mu_B$ and a metallic aspect.

The metallic behavior is also predominant in CoMoFeZ compounds. If we consider the structure type 2 as equivalent to that of the regular Heusler structure and type 1 to that of the inverse structure of the ternary parents, CoMoFeZ would be the only pair crystallizing in the inverse type structure. In these systems, X and Y atoms are in symmetric positions a (1/4, 1/4, 1/4) and c (3/4, 3/4, 3/4). The interactions between these elements are parallel, where the 3d transition atoms carry larger magnetic moments as compared to the 4d ones. CoMoFeSb with the stable metallic parents: the inverse Co_2MoSb and the normal Fe_2MoSb, shows a moderate moment that conforms well to the slater Pauling rule ($4\mu_B$). This compound also adopts the same metallic character of the ternary parents. CoMoFeGe on the other hand, even of exhibiting no half-metallic character, its magnetic moment of $2.82\mu_B$ conforms well to the Slater Pauling rule ($3\mu_B$). This compound with a combination of two stable magnetic inverse metals Co_2MoGe and Fe_2MoGe, follows the same metallic character of the precedent ternary parents.

For the pair FeMoZrZ with the parents (the stable metal Fe_2MoGe-the unstable semiconductor Fe_2ZrGe) and (the stable metal Fe_2MoSb-the stable half-metal Fe_2ZrSb), respectively, Fe atoms carry the largest magnetic moment, while the interactions between 4d-Zr element and the rest of atoms is antiparallel. For these two quaternary systems, we obtained the magnetic moments $1.99\mu_B$ and $0.97\mu_B$, respectively. Despite of being in good agreement with the Slater Pauling rule ($2\mu_B$ and $1\mu_B$, respectively), these two compounds can only be considered as near half-metals with a near gap in spin up channel.

Table IV.6 Total and atomic magnetic moments of the quaternary systems.

Systems	***Atomic magnetic moments***				***total magnetic moments***
	X	**X'**	**Y**	**Z (Ge/Sb)**	
FeMoZrGe	1.32016	0.64483	-0.09558	-0.01704	1.98759
FeMoZrSb	0.85638	0.25641	-0.09805	-0.00993	0.97443
CoMoZrGe	0.28590	0.42799	0.02657	0.00160	0.84358
CoMoZrSb	1.66160	0.97556	0.15500	0.00152	2.97668
CoFeZrGe	0.58363	0.67064	-0.09774	-0.00985	1.04972 [16]
CoFeZrSb	1.03951	1.25514	-0.15045	0.00580	1.99345 [16]
CoMoFeGe	1.21085	0.36138	1.27059	0.00015	2.82752
CoMoFeSb	1.24107	0.84237	1.75028	-0.00765	3.87813

The total and partial densities of states were also calculated at equilibrium lattice constants in order to better understand the electronic properties of these alloys (see figures (IV.6) and (IV.7)), where the positive DOS values refer to spin-up channel and the negative values represent spin-down states. Obviously, the main hybridizations come from the d−d bands of the transition metal atoms. These atoms contribute the most in the formation of the gap.

The s-p bands of the main group elements are also important in determining the positions of the d-bands. In the present series of compounds, Ge and Sb atoms introduce a deep lying s-band at about -10 and -12 eV, respectively, and three p-bands situated below the d-bands of the transition metals.

Several studies [17,18] have explained the dependence of the half-metallic gap on positions of the bonding (e_g, t_{2g}) and anti-bonding (e_u, t_u) orbitals resulting from the hybridizations between X, X' and Y transition metal elements. The X and X' d-orbitals hybridize forming the $2e_g$ and

$3t_{2g}$ bonding orbitals. These hybrid orbitals hybridize with Y d-states developing $2e_u$ and $3t_u$ bonding and anti-bonding hybrid orbitals and creating a gap in between.

For the majority channel of CoFeZrZ pair, the valence band region from −4 to -1 eV is mostly dominated by the t_{2g} states of Co and Fe atoms. In the energy region from −1 to 1 eV, the main contributions arise from the e_g states of the 3d transition metals. While from 1 to 4 eV, it is the Zr t_{2g} and e_g states that predominate. As for the minority channel, the energy region from −4 to 0 eV refers to the t_{2g} states of Co and Fe elements. The energy interval from 0 to 4 eV shows that the e_g states of Co and Fe atoms in addition to Zr-t_{2g} and -e_g degenerates participate the most to the total DOS.

All three compounds CoMoZrGe and FeMoZrZ (Z = Ge, Sb) present a band gap in spin up channel, however, the gap do not extend through the Fermi level in any of them.

The majority and minority spin directions of CoMoZrGe alloy show common features with a spin up gap that is closer to the Fermi level than the one situated in spin down channel. The spin up energy region from -4 to 0 eV shows that the main peaks belong to Co- and Mo-t_{2g} states. Above Fermi level, we notice that the d-e_g states of Co and Mo appear in the energy between 0 and 2 eV, while Zr-t_{2g} and -e_g degenerates show contributions from 2 to 4 eV.

CoMoZrSb is also an ordinary metal presenting a small gap in spin down channel. The t_{2g} states of Co and Mo atoms dominate the spin up energy region from -4 to -1 eV. Whereas from -1 to 1 eV, we notice small contributions from Co- and Mo-e_g states. The last partition from 1 to 4 eV refers to Zr-e_g and -t_{2g} orbitals. As for spin down channel, the energy region from -3 to 0 eV is populated by Co- and Mo-t_{2g} orbitals with a relatively small contribution from Zr. Above Fermi level, Co- and Mo-e_g states participate from 0 to 2 eV, while Zr-e_g and t_{2g} states dominate from 2 to 4 eV.

Similar to CoMoFeGe, the hybridizations between 3d and 4d atoms in CoMoFeSb near Fermi level may be responsible of the reduction of the total magnetic moment in this compound. For the minority spin channel, all transition metals show major contributions of the d-t_{2g} states from -4 eV to 0 eV. Above E_F, Co- and Fe-e_g states contribute from 0 to 2 eV in addition to Mo (t_{2g}+e_g) degenerates. The majority channel from -4 to -2 eV is dominated by Co and Fe-t_{2g} degenerates as well as small participation of Mo-t_{2g} states. The partition from -2 to 0 eV is relative to the e_g orbitals of Co and Fe atoms, while the t_{2g} and e_g degenerates of Mo arise in the energy between 0 and 2 eV.

For FeMoZrGe (FeMoZrSb) alloy, Fe- and Mo-t_{2g} orbitals contribute the most in the energy region between -4 and 0 eV of spin up channel. From 0 to 2 eV, the main contributions come from the e_g states of Fe and Mo atoms. While Zr-e_g and t_{2g} orbitals are dominant from 2 to 4 eV. In the minority spin direction from -2 to 1 eV, Fe- and Mo-t_{2g} orbitals are the main contributors in addition to small participation from Zr. From 1 to 2 eV, the main contributions originate from Fe and Mo-e_g states, and from 2 to 4 eV, they refer to Zr-e_g and -t_{2g} orbitals.

In general, the loss of the half-metallic properties refers either to the atomic composition of these alloys or to the hybridizations between the 3d elements and Mo 4d delocalized orbitals.

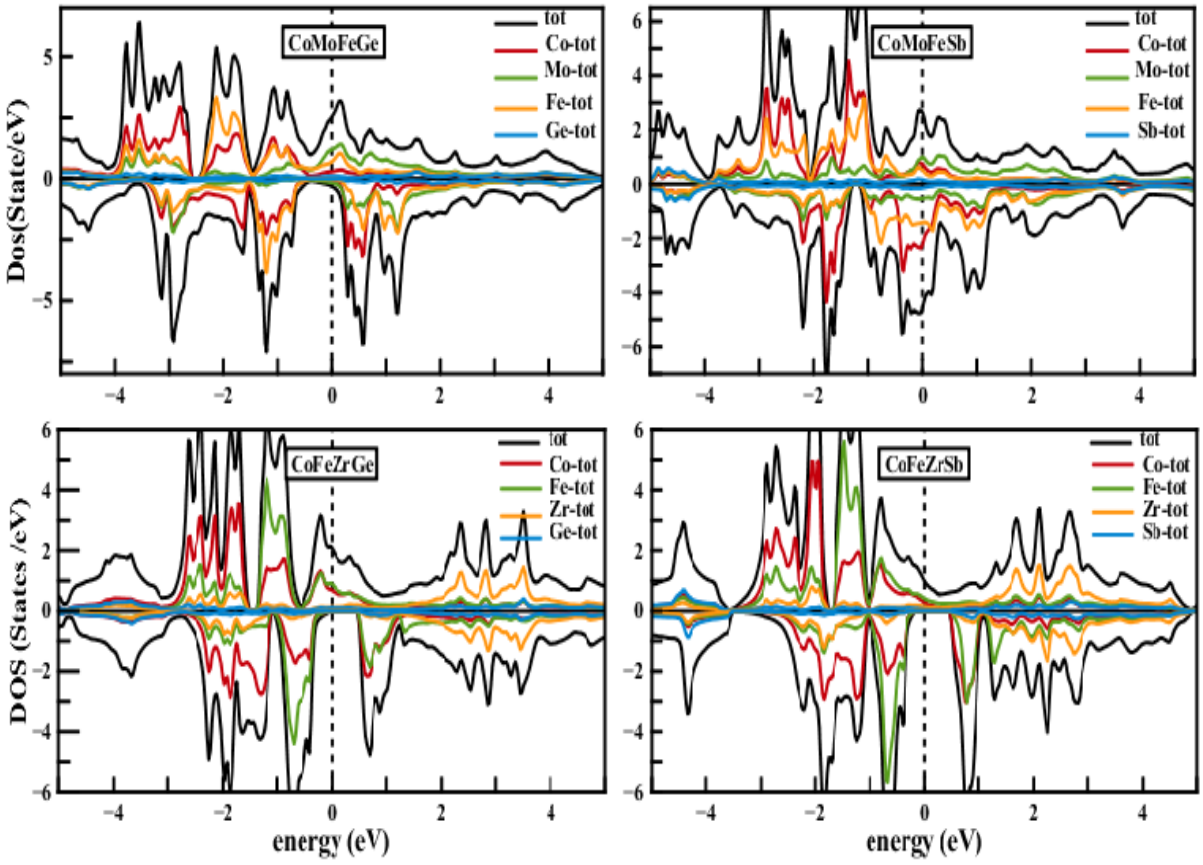

Figure IV.6.a Total densities of states for the quaternary CoX'YZ (X' = Mo, Fe; Y = Zr, Fe; Z = Ge, Sb) Heusler alloys.

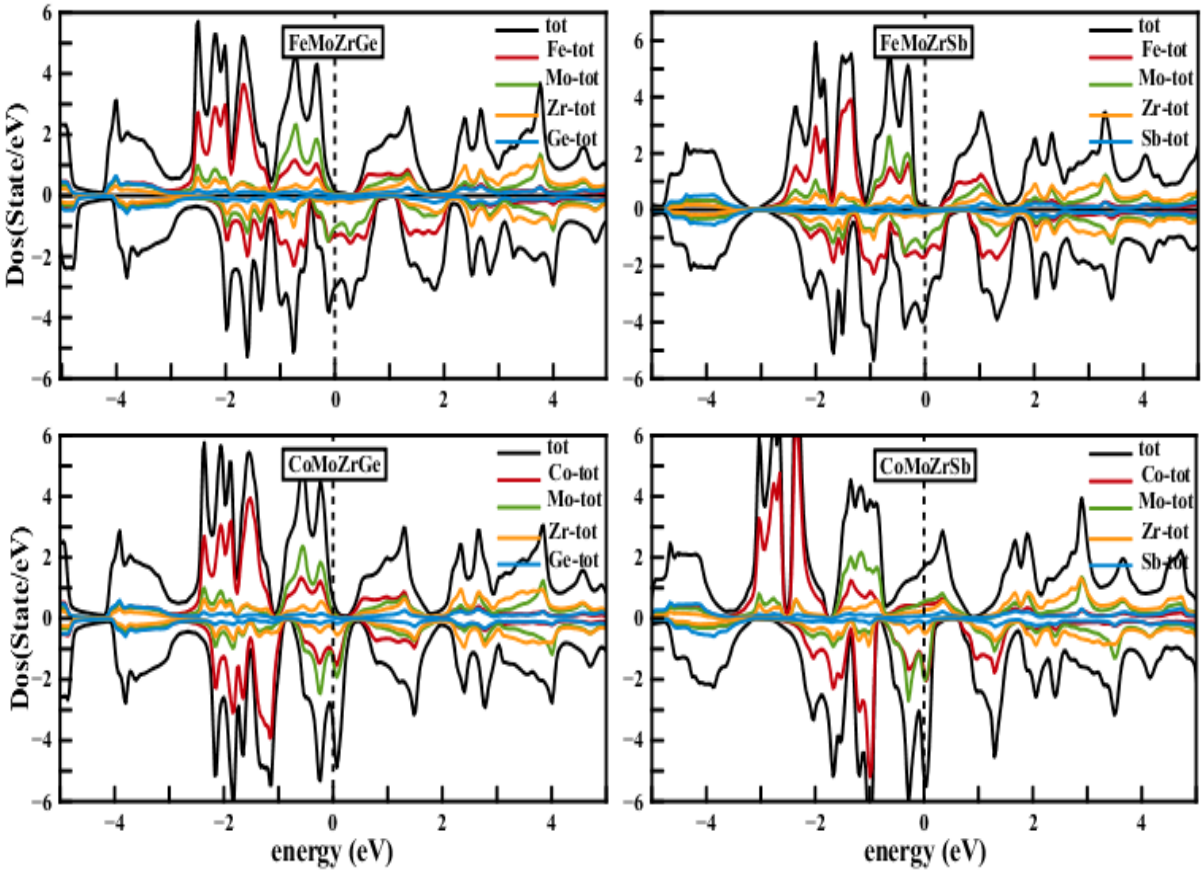

Figure IV.6.b Total densities of states for the quaternary XMoZrZ (X = Co, Fe; Z = Ge, Sb) Heusler alloys.

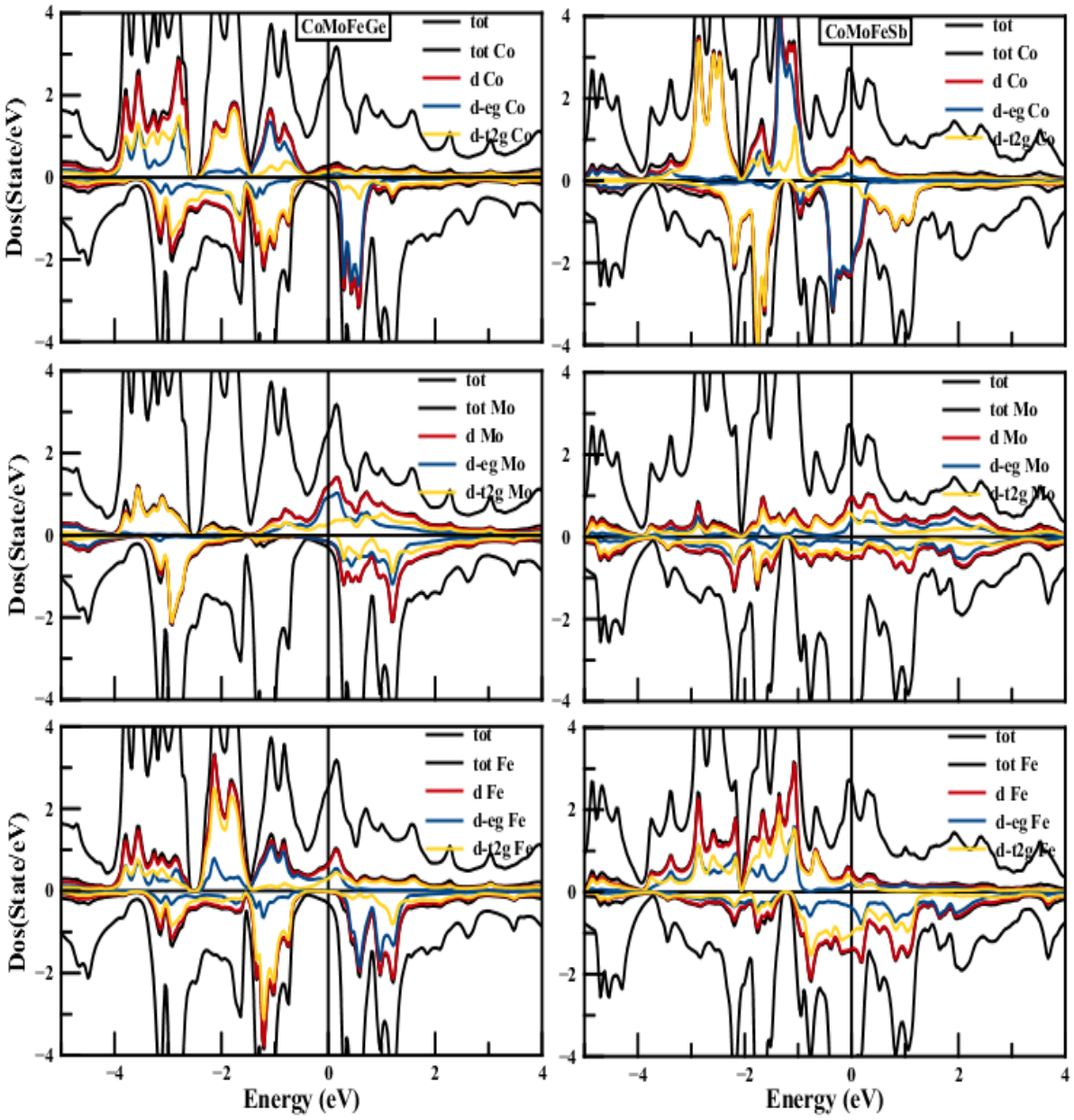

Figure IV.7.a Partial densities of states for CoMoFeZ (Z = Ge, Sb) quaternary alloys.

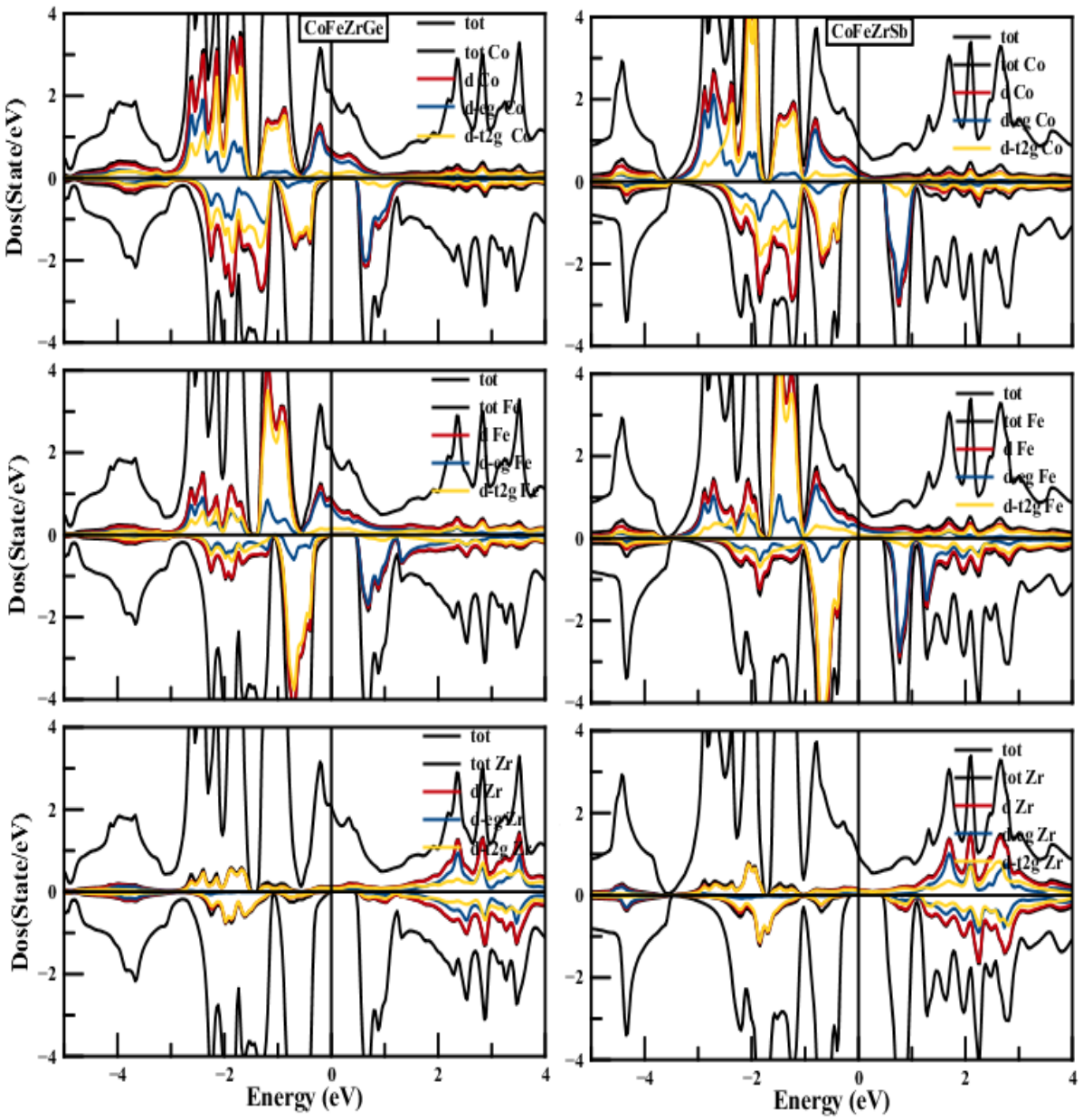

Figure IV.7.b Partial densities of states for CoFeZrZ (Z = Ge, Sb) quaternary alloys.

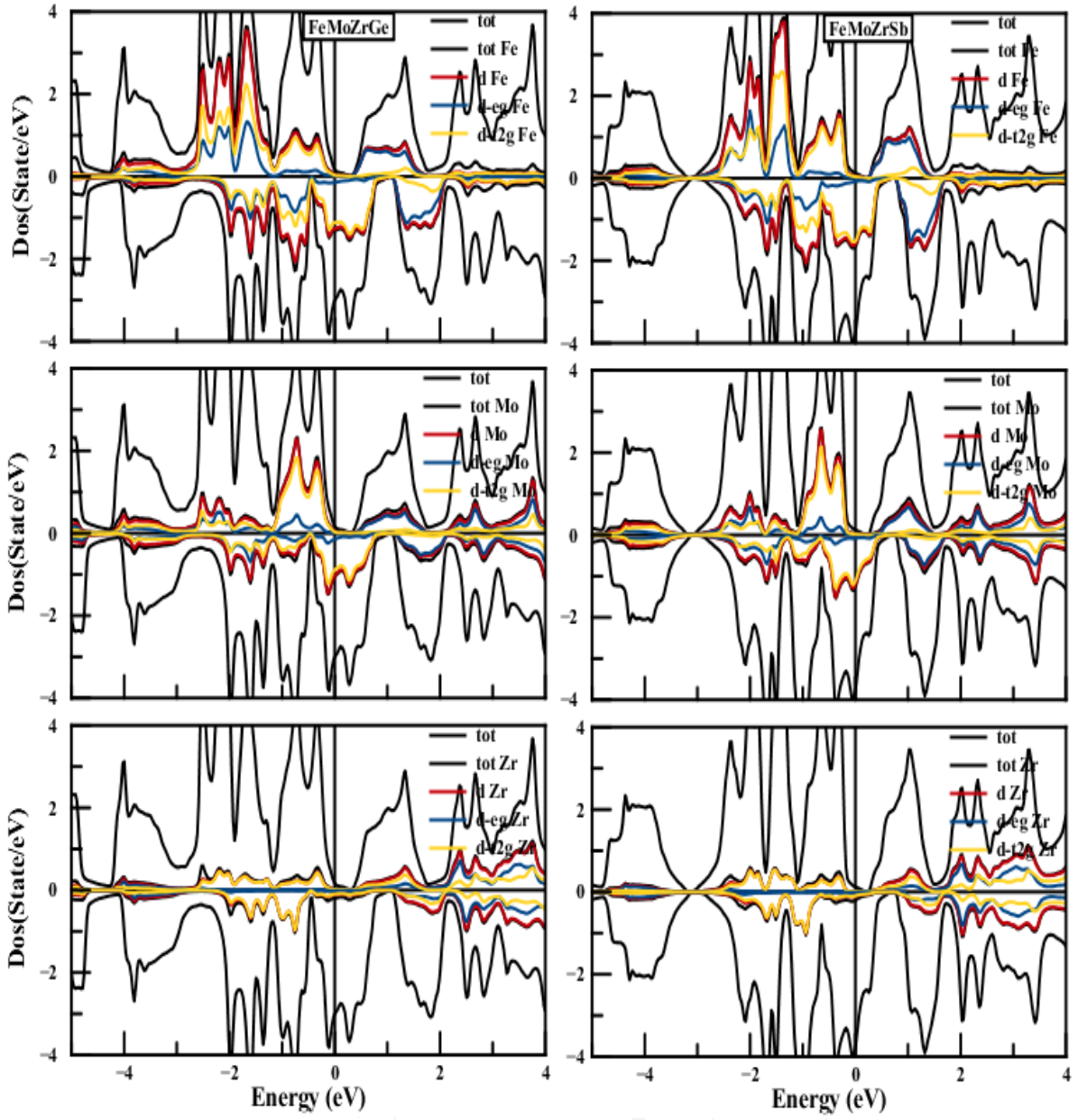

Figure IV.7.c Partial densities of states for FeMoZrZ (Z = Ge, Sb) quaternary alloys.

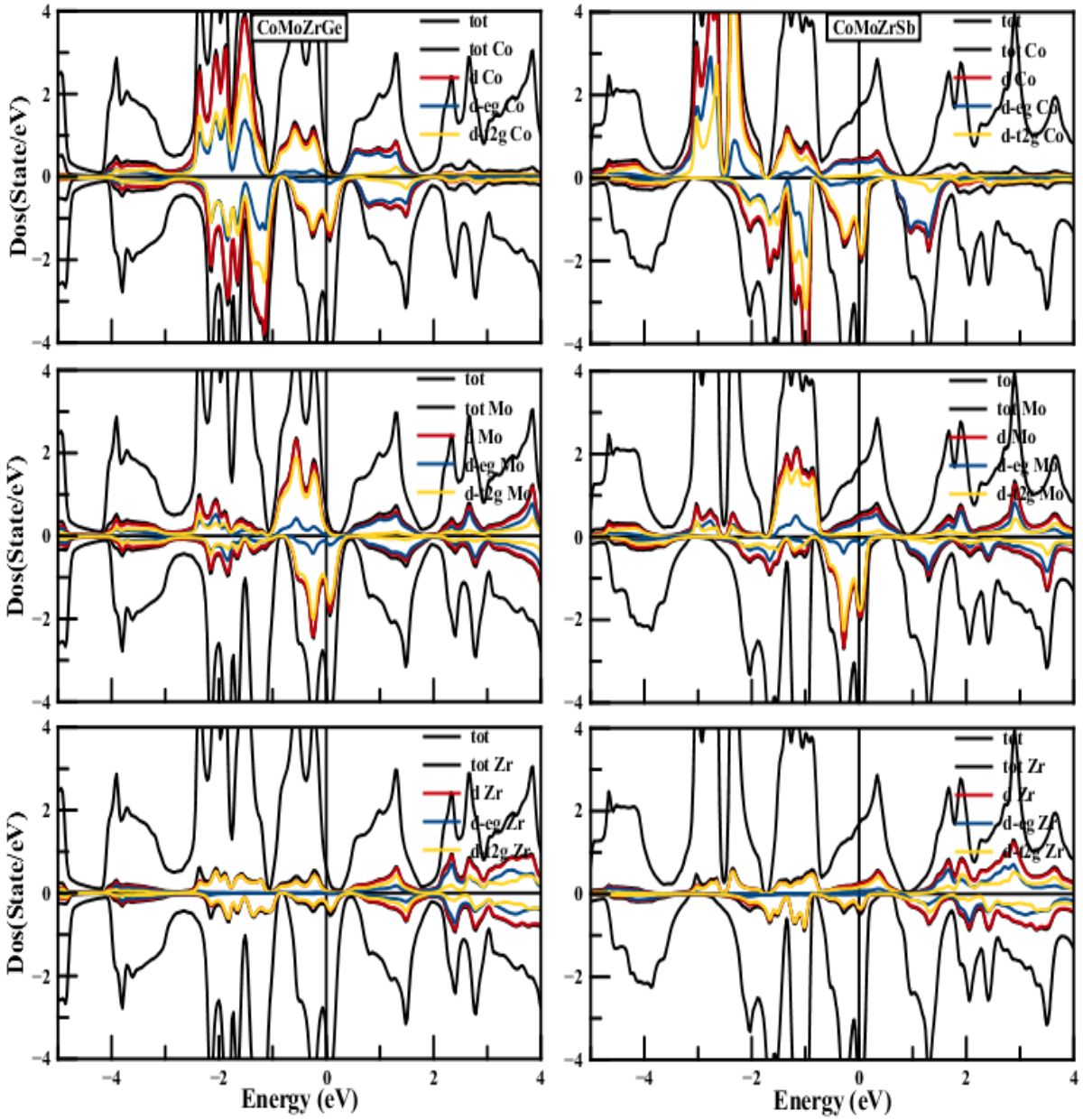

Figure IV.7.d Partial densities of states for CoMoZrZ (Z = Ge, Sb) quaternary alloys.

IV.2.3 Elastic properties

We have also checked the mechanical stability of these quaternary systems by calculating the three elastic parameters $\mathbf{C_{11}}$, $\mathbf{C_{12}}$ and $\mathbf{C_{44}}$ (see table (IV.7)). Because the resulting elastic constants satisfy the Born-Huang preconditions, the quaternary Heuslers XX'YZ may be considered as stable alloys.

The evaluated values of B and G that are listed in table (IV.7) prove the hardness and strength of XX'YZ quaternary alloys. Moreover, the values of the Bulk that were extracted from Murnaghan equation of state [19] are very close to those calculated using the elastic constants for all alloys (check table (IV.5). The high values of Young's modulus presented by the quaternary Heuslers also support their stiffness.

Poisson's ratio ($\boldsymbol{\upsilon}$) and Pugh's factor ($\boldsymbol{k}$) were also calculated in order to check the brittle or ductile character in these materials. The resulting values of Pugh's and Poisson's ratio for XMoZrGe (X = Co, Fe) and CoFeZrZ (Z = Ge, Sb) pairs of alloys are greater than 1.75 and 0.3, respectively, which confirms the ionic character and ductility of these alloys. For the pair XMoZrSb (X = Co, Fe), Poisson's and Pugh's ratios are under the limited values, which means these two materials may be brittle. The brittle nature of CoMoZrSb and FeMoZrSb alloys is also substantiated by the negative values of Cauchy pressure (-7.99 GPa and -3 GPa, respectively). CoMoFeZ (Z = Ge, Sb) pair on the other hand have shown a remarkable ductile behavior and a strong malleability as both alloys are characterized by high values of $\boldsymbol{\upsilon}$ and $\boldsymbol{k}$. Moreover, because the anisotropic factor (A) is either smaller or greater than 1, XX'MoZ systems possess an anisotropic behavior.

Lastly, the high values of $\boldsymbol{T}_{\text{melt}}$ for all these quaternary alloys confirm their atomic bonding strength and ability to maintain their crystal structure over a large range of temperatures.

Table IV.7 Calculated elastic constants and mechanical parameters (GPa) of quaternary compounds at equilibrium lattice constants.

	C_{11}	C_{12}	C_{44}	B	G	E	υ	A	k	C_p	T_{melt}
FeMoZrGe	222,3	142,8	78,14	169.3	59.59	159.9	0.34	1.96	2.84	64.62	1866.85 $\pm 300K$
FeMoZrSb	318,8	128,5	131,5	191.9	115.5	288.7	0.25	1.38	1.66	-3	2437.46 $\pm 300K$
CoMoZrGe	272,2	146,2	96,04	188.2	81.1	212.7	0.31	1.53	2.32	50.2	2161.41 $\pm 300K$
CoMoZrSb	313,2	94,59	102,6	167.5	105.2	261.3	0.24	0.94	1.59	-7.99	2404.25 $\pm 300K$
CoFeZrGe	226.2	154.9	92	178.7	62.91	100.3	0.41	2.58	5.01	62.9	1889.84 $\pm 300K$
CoFeZrSb	255,1	108.1	67.2	157.1	69.66	190.8	0.3	0.91	2.14	40.9	2060.64 $\pm 300K$
CoMoFeGe	252,9	213,1	62,13	226.3	39.42	111.8	0.42	3.12	5.74	150.9	2047.40 $\pm 300K$
CoMoFeSb	204,5	182,9	124,8	190.1	51.55	141.8	0.38	11.6	3.69	58.1	1761.6 $\pm 300K$

IV.2.4 Thermoelectric properties

The peculiarity of thermoelectric materials is their ability to transform heat into useful energy. For this reason, they are very beneficial in the field of waste heat recovery systems and power generators. Figures (IV.7) and (IV.8) display the thermoelectric properties of the quaternary XX'YZ systems. We have also listed the maximum values of the Seebeck coefficient, electrical conductivity and power factor of these alloys in table (IV.8).

From figure (IV.8 (a)), we notice that CoMoZrSb exhibits positive Seebeck values with increasing temperature, indicating it is a p-type material. The total thermopower of this compound shows an intense decrement from a value of 489.9µV/K to a minimum of 129.8µV/K. Unlike CoMoZrSb, we notice an almost consistent trend in the Seebeck of CoMoZrGe upon increase of temperature, where the maximum value have reached 148.3µV/K. Since the Seebeck coefficient remains positive, CoMoZrGe is also a p-type material.

For CoMoFeGe (CoMoFeSb) alloy, the Seebeck increases slowly upon increase of temperature with a maximum of 95.3µV/K (93.9µV/K) at 400K (700K). CoMoFeGe shows high positive values of thermopower below room temperature in contrast to CoMoFeSb, indicating a p-type of conduction for the low s-p valent alloy and an n-type of conduction for the high valent one. Whereas above, both alloys show nearly equal positive Seebeck values with holes as main charge carriers.

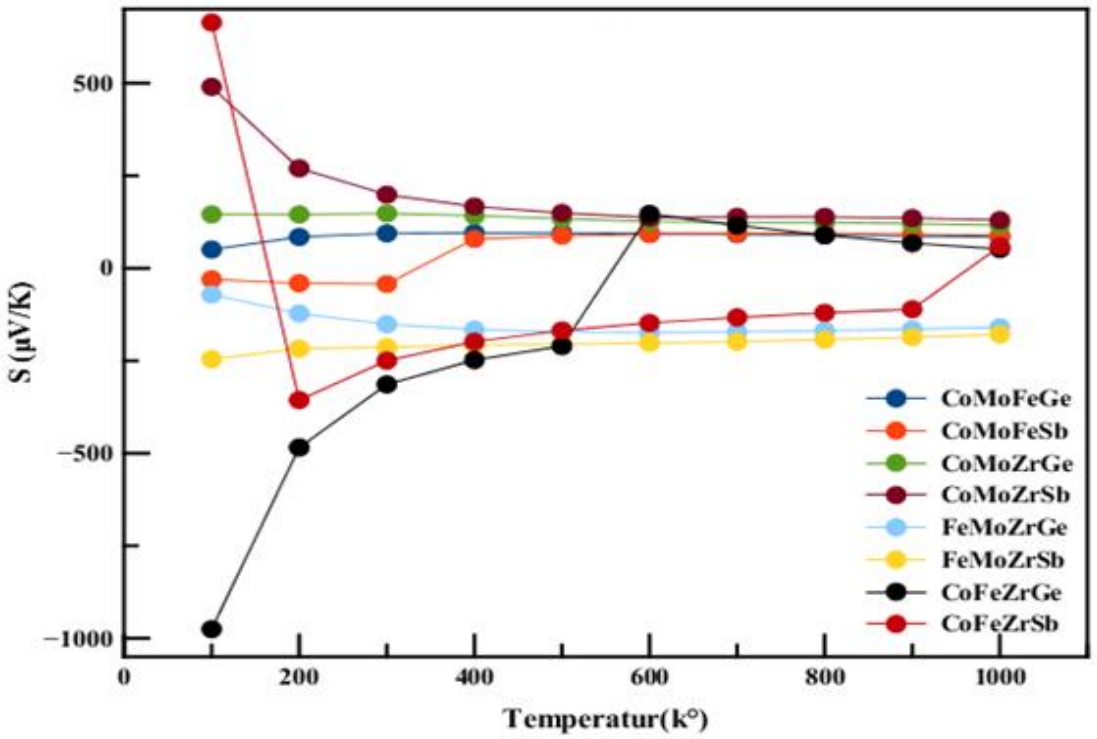

Figure IV.8.a Temperature dependence of the Seebeck coefficient (S) for XX'YZ (X = Co, Fe; X' = Mo, Fe; Y = Zr, Fe; Z = Ge, Sb) quaternary alloys.

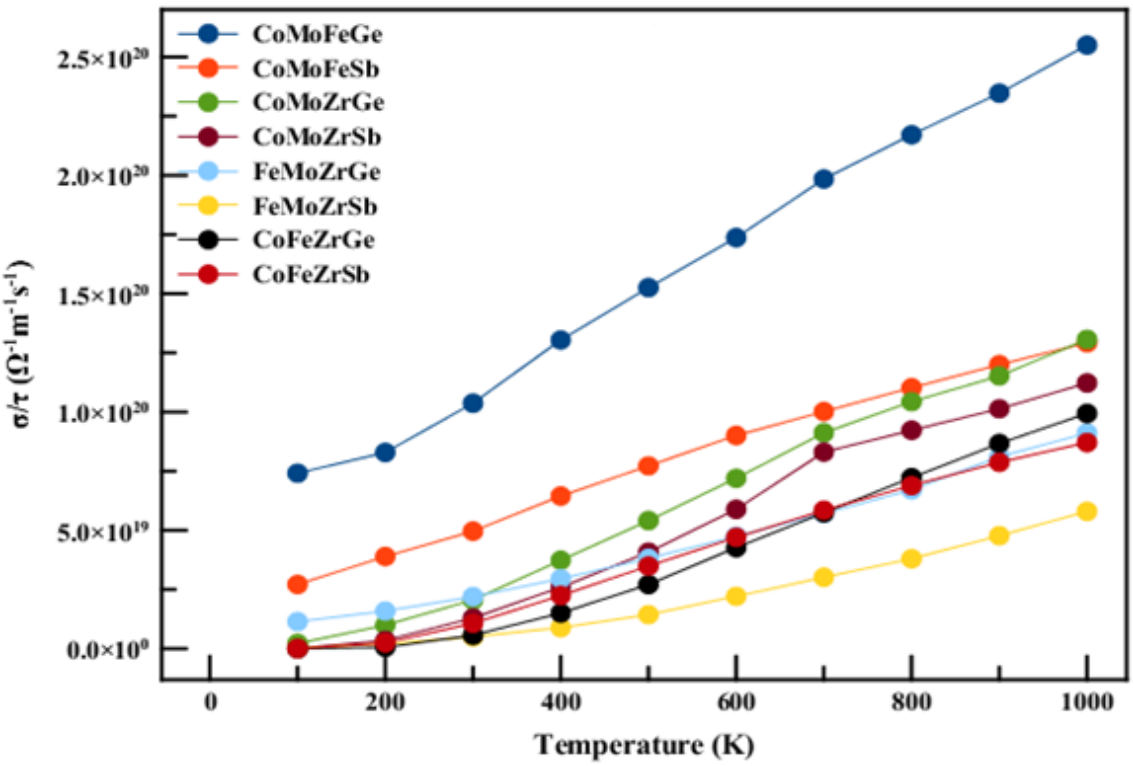

Figure IV.8.b Temperature dependence of the electrical conductivity (σ) for XX'YZ (X = Co, Fe; X' = Mo, Fe; Y = Zr, Fe; Z = Ge, Sb) quaternary alloys.

For CoFeZrZ alloys, we notice a sharp decaying trend in the total Seebeck coefficient from a value of -975.36 and 664.16 microV.K^{-1}, respectively, below room temperature, and a slow decaying trend above. The Seebeck of CoFeZrGe is negative below 500K (suggesting an n-type of conduction) and positive above (a p-type of conduction). Whereas for CoFeZrSb, the Seebeck remains negative in a temperature range from 200 to 900K. This compound is at the whole an n-type material.

The last two alloys, FeMoZrGe and FeMoZrSb, show negative values of thermopower, which overbalances the n-type of conduction. Below 600K, the total thermopower of FeMoZrGe increases reaching -173.6µV/K. As for FeMoZrSb, it shows a decaying trend from a value of -245.8µV/K. Above 600K, the Seebeck curve decreases for both alloys.

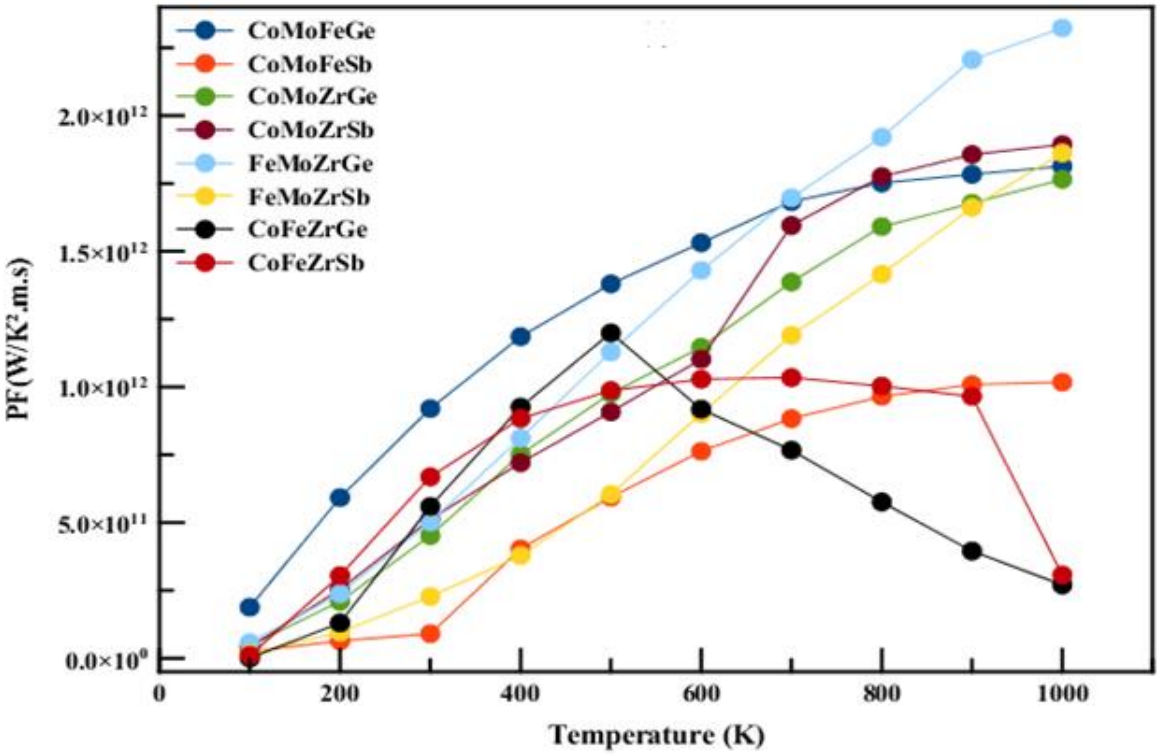

Figure IV.9 Temperature dependence of the Power Factor (PF) for the XX'YZ (X = Co, Fe; X' = Mo, Fe; Y = Zr, Fe; Z = Ge, Sb) quaternary alloys.

Table IV.8 The maximum values of the Seebeck coefficient, electrical conductivity and power factor of the quaternary alloys.

	S (μV/K)	***σ/τ (*10^{20}Ω^{-1}m^{-1}s^{-1})***	***PF(10^{12}W/K^2.m.s)***
FeMoZrGe	-173.6	0.91	2.32
FeMoZrSb	-245.8	0.58	1.86
CoMoZrGe	148.3	1.3	1.76
CoMoZrSb	489.9	1.22	1.89
CoFeZrGe	-975.36	0.99	1.19
CoFeZrSb	664.16	0.87	1.03
CoMoFeGe	95.3	2.55	1.81
CoMoFeSb	93.9	1.29	1.01

The electrical conductivity (σ/τ) is illustrated in figure IV.8 (b), where all alloys show a monotonous increment within temperature.

For the pair FeMoZrZ, the conductivity curves follow a linear altitude showing a gradual increasing trend below room temperature and a sharp one above, where the ultimate peaks have reached $9.1*10^{19}$ and $5.8*10^{19}\Omega^{-1}m^{-1}s^{-1}$, respectively.

The electrical conductivity of CoMoFeGe increases remarkably as compared to the rest of materials, where the highest value have reached $2.55*10^{20}\Omega^{-1}m^{-1}s^{-1}$.

For CoMoFeSb, CoMoZrGe and CoMoZrSb alloys, the conductivity increases sharply up to 700K with the ultimate values $1.29*10^{20}$, $1.3*10^{20}$ and $1.22*10^{20}\Omega^{-1}m^{-1}s^{-1}$, respectively. Finally, the two half-metals possess an almost linear increment in the total conductivity, where CoFeZrGe exhibits a higher maximum conductivity than CoFeZrSb ($0.99*10^{20}$ and $0.87*10^{20}$

$\Omega^{-1}m^{-1}s^{-1}$, respectively). The increasing trend in the total conductivity confirms the half-metallic behavior in these compounds.

In order to estimate the amount of power that could be generated by these quaternary Heuslers, we have calculated the variation of the power factor (PF) within temperature (see figure IV.9) using the following equation:

$$PF = S(\uparrow)^2\sigma(\uparrow)/\tau + S(\downarrow)^2\sigma(\downarrow)/\tau$$

We notice an exponential rise in the PF curve of CoMoFeZ pair, where the lower valent p-group alloy shows high efficiency due to its higher values of Seebeck coefficient and conductivity as compared to CoMoFeSb. For these two compounds, the power factor have reached an optimum of $1.81*10^{12}W/K^2.m.s$ and $1.01*10^{12}W/K^2.m.s$, respectively.

CoFeZrZ alloys also show an exponential behavior, where the power factor of CoFeZrGe increases up to 500K reaching a maximum of $1.19*10^{12}W/K^2.m.s$, and decreases above. CoFeZrSb shows the same trend with a maximum of $1.03*10^{12}W/K^2.m.s$ at 700K.

The power factor of FeMoZrZ and CoMoZrZ alloys increases dramatically upon increase of temperature. FeMoZrGe exhibits a PF value of $2.32*10^{12}W/K^2.m.s$. As for FeMoZrSb, we obtained the value $1.86*10^{12}W/K^2.m.s$.

As for the last pair of alloys, CoMoZrZ, the maximum PF value have reached $1.76*10^{12}W/K^2.m.s$ and $1.89*10^{12}W/K^2.m.s$, respectively.

To conclude, we have employed the FP-LAPW method based on DFT within the generalized gradient approximation GGA to investigate the properties of sixteen ternary and quaternary Fe- and Co-based Heuslers.

First, we have studied the electronic properties of the ternary alloys, where the band structure calculations confirmed the existence of a true half-metallic character in two compounds, Co_2ZrGe and Fe_2ZrSb. An indirect band gap along Γ-X direction was obtained in the minority spin channel of each half-metal with the values 0.59 eV and 0.73 eV, respectively.

The three elastic coefficients supported the stability of Co_2ZrGe, Fe_2ZrSb and Fe_2MoZ (Z = Ge, Sb) alloys only. The calculated elastic parameters confirmed the brittleness of Co_2ZrGe and Fe_2MoZ alloys, while a ductile behavior characterized Fe_2ZrSb compound. This new half-metal definitely requires a detailed phonic and thermoelectric discussion.

Next, we have derived eight quaternary systems from the previous ternary parent compounds. In this series, we obtained two other half-metals, CoFeZrGe and CoFeZrSb that were also found to exhibit indirect band gaps along Γ-X direction in spin down channel with the values 0.5 eV and 0.67 eV, respectively. As for the rest of materials, the metallic character was predominant.

Moreover, we have examined the mechanical stability of these quaternary systems and they were all found to satisfy the mechanical Born-Huang stability criteria. The elastic parameters have also confirmed their metallic bonding and ductility except for XMoZrSb pair (X = Co, Fe), where the brittle nature takes-over. In addition, the estimated high melting temperatures proved the ability of these systems to maintain their crystal structure over a large range of temperatures.

Lastly, the quaternary XX'YZ materials have shown a commendable thermoelectric behavior and good efficiency in the thermoelectric field applications. The largest values of the power factor were obtained for the near half-metallic FeMoZrGe and the metallic CoMoZrSb regarding their high Seebeck coefficients. The remaining quaternary alloys have also exhibited interesting thermoelectric features, where the power factor have reached as high as $1.86*10^{12} W/K^2.m.s$ for FeMoZrSb alloy.

After performing an intensive theoretical investigation of the crystal structure, magnetic properties, mechanical stability and thermoelectric behavior of the ternary X_2YZ (X = Fe, Co; Y = Zr, Mo; Z = Ge, Sb) and quaternary XX'YZ (X = Co, Fe; X' = Mo, Fe; Y = Zr, Fe; Z = Sb,

Ge) group of Heuslers, our findings suggest that these are promising materials for spin-electronics (due to the robustness of half-metallicity) and thermoelectric applications.

IV. 3 Bibliography

1. J.P. Perdew, K. Burke, et M. Ernzerhof, Phys. Rev. Lett., 77, 3865 (1996).
2. N.W. Ashcroft, N.D. Mermin, Solid State Physics, Saunders College Publishing, New York, 1976, p.9.
3. S. Skaftouros, K. Özdoğan, E. Şaşıoğlu, I. Galanakis, Phys. Rev. B87 (2013) 024420.
4. Li S, Liu Y, Ren Z, Zhang X, and Liu G. J Korean Phys Soc 2014; (65) 1059.
5. International Journal of Environmental, Chemical, Ecological, Geological and Geophysical Engineering 2015; (9): 4.
6. Slater JC. Phys Rev 1936; (49): 537.
7. Labo DN, Priolkar KR, Koide A, Emura S. 2017 Effect of site occupancy disorder on martensitic properties of Mn2NiIn type alloys: X-ray absorption fine structure study. J. Appl. Phys. 121, 053902.
8. Galanakis I, Dederichs PH and Papanikolaou N. Phys Rev B 2002 (66): 174429.
9. M. Born, K. Huang, Dynamical Theory of Crystal Lattices, Clarendon, Oxford 1956, p. 420.
10. Voigt W. Lehrbuch der kristallphysik (mit ausschluss der kristalloptik). Springer-Verlag; 2014.
11. Reuss A. Calculation of the flow limits of mixed crystals on the basis of the plasticity of monocrystals. Z Angew Math Mech 1929;9:49–58.
12. Frantsevich IN, Voronov FF & Bokuta SA In & Frantsevich IN (Ed.). Elastic Constants and Elastic Moduli of Metals and Insulators. Naukova Dumka, Kiev. (1983); 60: 180.
13. Pugh SF. Relations between the elastic moduli and the plastic properties of polycrystalline pure metals. Philos. Mag. (1954); 45: 823.
14. J. Wang, S. Yip, S.R. Phillpot, D. Wolf, Phys. Rev. Lett. 71, 4182 (1993).
15. M.E. Fine, L.D. Brown and H.L. Marcus, Scr. Metall. 18 (1994) p.951.
16. R. Paudel and J. Zhu, J. Magn. Magn. Mater. 453, 10 (2018).
17. S. Ghosh, S. Ghosh, arXiv:1812.02856, 2018.
18. I. Galanakis, P. Mavropoulos and P. H. Dederichs, *J. Phys. D: Appl. Phys.* 39, 765 (2006).
19. F. D. Murnaghan, Natl. Acad. Sci. U. S. A. 30, 5390 (1994).

Summary

The general idea of this thesis was based on the development of new half-metals with different properties by mixing both 3d and 4d magnetic elements.

Using FP-LAPW method within the generalized gradient approximation (GGA), we have investigated a group of ternary and quaternary Fe- and Co-based materials. Eventually, a pair of ternary (Co_2ZrGe, Fe_2ZrSb) and a pair of quaternary (CoFeZrGe, CoFeZrSb) compounds were identified to be true half-metals. They exhibit indirect band gaps in the minority spin channel with the values 0.59 eV, 0.73 eV, 0.5 eV and 0.68 eV, respectively, along Γ-X direction. We have also found a non-magnetic semiconductor, Fe_2ZrGe with a gap of 0.14 eV along the same direction.

For the rest of materials, the band structures and the densities of states have shown no true half-metallic properties.

The elastic parameters of the ternary materials have been estimated and only four compounds Fe_2ZrSb, Co_2ZrGe and Fe_2MoZ (Z = Ge, Sb) were found to satisfy the conditions of Born-Huang stability criteria. In contrary, all quaternary alloys were found to be dynamically stable.

We have also calculated the thermoelectric efficiency of the quaternary systems using the BoltzTrap code. Large Seebeck coefficients were obtained for the two half-metallic CoFeZrGe and CoFeZrSb compounds. These values have reached as high as -975.36 and 664.16 microV.K^{-1}, respectively, at 100K. Both systems exhibit high power factors as well, with the maximum values $1.19*10^{12}WK^{-2}m^{-1}s^{-1}$ and $1.03*10^{12}Wm^{-1}K^{-2}s^{-1}$, respectively, above room temperature.

The remaining quaternary systems have also shown a high thermoelectric efficiency, where the values of the power factor have reached as high as $2.32*10^{12}W/K^2.m.s$, which proves their capability as promising thermoelectric materials.

Eventually, we look forward for more theoretical and experimental researches concerning these materials. In addition, we would like to work on the substitution of the magnetic components of these systems and modifying their structural arrangements, which could result in the formation of a half-metallic gap and perform their spintronic properties.